UC Berkeley
UC Berkeley Electronic Theses and Dissertations

Title
Nanocrystal Photovoltaics: The Case of Cu2S-CdS

Permalink
https://escholarship.org/uc/item/4fz2v7wg

Author
Rivest, Jessica Louis Baker

Publication Date
2011

Peer reviewed|Thesis/dissertation

eScholarship.org Powered by the California Digital Library
University of California

Nanocrystal Photovoltaics: The Case of Cu_2S-CdS

by

Jessica Louis Baker Rivest

A dissertation submitted in partial satisfaction of the

requirements for the degree of

Doctor of Philosophy

in

Engineering - Mechanical Engineering

in the

Graduate Division

of the

University of California, Berkeley.

Committee:
Professor Paul Alivisatos, co-chair
Professor David Dornfeld, co-chair
Professor Alice Agogino
Professor Peidong Yang

Fall 2011

Nanocrystal Photovoltaics: The Case of Cu_2S-CdS

Copyright 2011
Jessica Louis Baker Rivest

ABSTRACT

Nanocrystal Photovoltaics – The Case of Cu_2S-CdS

by

Jessica Louis Baker Rivest

Doctor of Philosophy in Engineering

University of California, Berkeley

Professor A Paul Alivisatos, co-chair

Professor David Dornfeld, co-chair

In this dissertation, fine control over the morphology and composition of a nanostructured semiconductor thin film is demonstrated at a degree not previously possible. While such control is beneficial in a variety of optical and electrical devices, this research was performed from the perspective of photovoltaics.

A new architecture is presented for low cost and high conversion efficiency photovoltaics, utilizing self-assembled nanocrystals. A method is introduced for vertically aligning nanorods using a controlled-evaporation self-assembly technique, enabling the uniform alignment of nanorods on a square-centimeter substrate. Such meso-scale assembly and optimization required the development of a morphology quantification technique. The technique presented here utilizes grazing incidence x-ray diffraction to assemble a quantitative pole figure, or nanorod orientation histogram, and can be used with any thin film. After nanorod assembly, an asymmetric electrical junction (required for photovoltaic operation) is achieved in each rod using a cation exchange technique, which can be performed reliably and reversibly on-chip. This results in a film comprising a massively parallel array of single-crystal nanodiodes. Electrical measurements of these films show rectified behavior and reveal a photocurrent upon illumination of the aligned and cation-exchanged films. Finally, the stability of the Cu_2S phase is investigated as a function of nanocrystal size. The low chalcocite to high chalcocite solid-solid crystallographic phase transition is found to occur at temperatures depressed 60 Kelvin below the bulk phase transition temperature.

The research summarized in this dissertation describes a set of synthetic and analytical techniques that enable nanoscopic control of morphology and composition in device-scale semiconductor thin films. Such control may be leveraged to precisely manipulate the flow of charge carriers in

optoelectronic devices. Due to the simple wet chemical processes employed in the fabrication of these devices, the techniques presented suggest the possibility of very low cost.

This work provides a proof-of-concept for a next-generation photovoltaic device architecture, and serves as a set of guidelines for achieving the desired crystallographic phase, crystallographic orientation, and compositional patterning desired in a nanostructured semiconductor thin film.

ACKNOWLEDGEMENTS

This intellectual journey was made possible by my advisor, Paul Alivisatos, who leads gently and brilliantly by example. David Dornfeld supported the unusual circumstance of a mechanical engineer in chemistry, and made sure that tradition did not stand in the way of cross-disciplinary research. Alice Agogino was a mentor in teaching, providing oversight in my teaching assistantships and insight into career paths. Peidong Yang taught me chemistry and helped me reason through experiments early on in my graduate career. These members of my dissertation committee have been instrumental in guiding me through my doctoral work.

I am fortunate to have spent time with a variety of faculty mentors. Rachel Segalman, Delia Milliron, and Jeff Urban have been role models and sounding boards for how to lead an early and successful academic career. Dan Kammen exemplified interdisciplinary work, showing me its importance in the field of energy, and providing generous support and advice. Arun Majumdar's career has demonstrated a tasteful mix of fundamental exploration and real-world applicability, and represents a true paragon.

I have been lucky to have a large group of collaborators who have enriched not only the papers we've written together, but the entire scientific process. Prashant Jain was a patient collaborator with boundless intellectual energy and generous wordsmithery. Michael Toney introduced me to SSRL's beamline 11-3 and helped me think through experimental techniques and data interpretation. Leslie Jimison was reliable and cheerful throughout our fun collaboration. Asaph Widmer-Cooper's methodical work was an inspiration. Haimei Zheng was a model project lead, working extremely hard to produce admirable work. Sarah Swisher was a reliable collaborator and friend. Lam-Kiu Fong taught me how to bring relevance to coursework in the laboratory, and was a successful mentee.

I gratefully acknowledge fellowships from the National Science Foundation and later from Intel, which allowed me to concentrate on science rather than fundraising.

My labmates in the Alivisatos group have been invaluable in welcoming me to the world of chemistry, teaching me technique as well as safety, and empathizing with whatever state of research I happen to be in. Bryce Sadtler in particular spent many patient hours teaching me nanocrystal synthesis and helping me think through experiments. Charina Choi, Lilac Amirav, and Joey Luther have been valuable colleagues and friends, giving me good reason to come to lab even in the midst of difficult experiments. Trevor Ewers has spent his heart of gold on keeping the TEM in perfect working order, feeding his labmates, and keeping us ergonomic. Kate Nichols, our resident artist,

never missed an opportunity to admire the beauty of my samples, even when they were failed experiments. Jill Millstone was a friend and a strategist who made lab a fun place to be.

The PV Idea Lab and Energy Houseboat communities, in particular Dave Danielson, Cyrus Wadia, Ilan Gur, and Tonio Buonassisi, have provided interesting discussions, key introductions, and a warmth and camaraderie I could only have dreamt of.

Finally, my family and friends have been encouraging and curious, and were understanding when I needed to spend late nights at the Foundry SEM. Since before I can remember, my mother Kitty has asked questions about my classes and my research until I ran out of answers. My father Keith and sister Nikki have always been there to strategize around the critical parts of my doctoral research, and life in general. My father-in-law Ron was a quiet supporter, helping me see the academic world through his eyes. My mother-in-law Gail and my brother-in-law Alex have reminded me to have fun along the way, and to stop and smell (or photograph) the roses. My friend Libby has generously taken interest in every project I've undertaken, and has been a lifelong collaborator on all levels. My friend Kay believed in me loudly, and showed me how to cut a bold academic path. My cousin Maria encouraged me to teach early and often, and made Berkeley feel more like home. My friend Amy walked (or ran) this course in stride with me, and made me appreciate the luxury of academia at every turn. Ed Seldin and Leo van Glabbeek showed me how to appreciate the details.

My husband Chris has infused my life with adventure and energy. Together, we flourish.

ABBREVIATIONS & DEFINITIONS

TEM – transmission electron microscope
HRTEM – high resolution TEM
EFTEM – energy filtered TEM
SEM – scanning electron microsope
TWh – terawatt-hour
nm – nanometer
GIXD – grazing incidence x-ray diffraction
EDS – energy dispersive x-ray spectroscopy
RBS – Rutherford backscattering spectroscopy
Nanocrystal, nanoparticle – crystalline material with dimensions on the order of nanometers
Nanorod – rod-shaped nanocrystal
CIGS – copper indium gallium sulfide/selenide
CIS – copper indium selenide
CZTS – copper zinc tin sulfide
vdW – van der Waals
D^i - rotational diffusion constant
η_s - shear viscosity
ODF – orientation distribution function, pole figure
ITO - indium tin oxide
RMS – root mean square
PEG – polyethylene glycol
SAM – self-assembled monolayer
χ - polar angle
SSRL – Stanford Synchrotron Radiation Laboratory
MAR345 – detector plate for x-ray diffraction
LED – light emitting diode
MEMS – micro electronic mechanical system
AM1.5G – solar flux standard, 1,000W/m^2
EGaIn – eutectic gallium indium
PEDOT
Bulk, extended solid – macroscopic material
T_b (P_b) – Temperature (pressure) in bulk
LC – low chalcocite
HC – high chalcocite
JCPDS – Joint committee on Powder Diffraction Standards
d – nanorod diameter
ℓ, L - nanorod length
Vertical, perpendicular, aligned, oriented – assembled nanorods

Table of Contents

INTRODUCTION 1

1.1 ENERGY 1
1.2 PHOTOVOLTAICS 3
1.3 A THIRD GENERATION PHOTOVOLTAIC ARCHITECTURE 4
1.3.1 NANOCRYSTALS 5
1.3.2 Cu_2S-CdS 6
1.3.3 STABILITY 7
1.4 BROADER IMPLICATIONS 8
1.5 REFERENCES 9

DEVICE-SCALE PERPENDICULAR ALIGNMENT OF COLLOIDAL NANORODS 12

2.1 INTRODUCTION 12
2.2 EXPERIMENTAL METHODS OF NANOROD ASSEMBLY 13
2.3 QUANTIFICATION OF THE ASSEMBLY PARAMETER SPACE 14
2.3.1 SYSTEM TEMPERATURE 16
2.3.2 NANOROD ASPECT RATIO 16
2.3.3 VDW INTERACTIONS 17
2.4 DEVICE-SCALE ASSEMBLY 20
2.5 REFERENCES 22

QUANTIFICATION OF THIN FILM CRYSTALLOGRAPHIC ORIENTATION USING X-RAY DIFFRACTION WITH AN AREA DETECTOR 25

3.1 INTRODUCTION 25
3.2 OBTAINING A COMPLETE, ACCURATE THIN-FILM POLE FIGURE 27
3.2.1 X-CORRECTION 28
3.2.2 POLARIZATION CORRECTION 30
3.2.3 ABSORBANCE CORRECTION 30
3.3 TECHNIQUE APPLICATION 31
3.4 CONCLUSION 34
3.5 REFERENCES 35

ASSEMBLED MONOLAYER NANOROD HETEROJUNCTIONS 38

4.1 INTRODUCTION 38
4.2 CATION EXCHANGE 39
4.3 DEPTH-PROFILING OF HETEROJUNCTION COMPOSITION 42
4.4 ELECTRICAL MEASUREMENTS OF MASSIVELY PARALLEL NANOROD JUNCTIONS 43
4.5 REFERENCES 47

SIZE DEPENDENCE OF A TEMPERATURE-INDUCED SOLID-SOLID PHASE TRANSITION IN COPPER(I) SULFIDE 50

5.1 INTRODUCTION 50
5.2 THE LOW- TO HIGH- CHALCOCITE TRANSITION IN COPPER(I) SULFIDE 51

5.3 SIZE-DEPENDENT PHASE RELATION **54**
5.4 IMPLICATIONS FOR Cu_2S APPLICATIONS **56**
5.5 REFERENCES **57**

CONCLUSION **59**

APPENDIX I. NANOROD ASSEMBLY **61**

APPENDIX II. QUANTIFICATION OF THIN FILM CRYSTALLOGRAPHIC ORIENTATION **70**

APPENDIX III. ASSEMBLED MONOLAYER NANOROD HETEROJUNCTIONS **74**

Chapter 1

Introduction

Energy drives the world as we know it: gravitational energy propels the earth around the sun and nuclear energy creates photons that radiate from the sun to the earth, creating pressure variations resulting in weather patterns and diurnal cycles that we resist with everything from climate-control appliances to illumination for reading. The understanding of the flow of energy, from chemical to potential to kinetic and beyond, is central to the study of science. It is therefore not surprising that as science evolves, it has come to pay special attention to that which is at its very core, and to that which lies at the very core of humanity as well: energy.

1.1 Energy

Human civilization has come to depend upon an immense supply of energy. In 2008 that demand measured 143,851 TWh or an average flux of 15.47 TW[1]. As the world population grows larger and wealthier, energy-consuming activities crescendo, provoking a projected 49% rise in power consumption by the year 2035[2]. Meeting these energy needs poses a great challenge. Meeting these energy needs in a **sustainable** manner poses a far greater challenge.

Assessing the resources available from which we can derive energy, we can categorize them as 'renewable' or 'consumable'. While energy sources such as methane, coal, and oil do regenerate over many thousands of years, the rate at which we are currently depleting them makes 'consumable' an appropriate label. Wind, solar, and hydro-power represent 'renewable' resources, which are not exhausted by continual use. Renewable and consumable resources are inherently difficult to compare, as they are in units of power and energy, respectively. By integrating the power from a renewable source for one year, we can get units of energy per year. Also, by dividing the consumable fuel supply by the number of years we need it to last, we can get units of energy per year. Figure 1-1 shows this data with an assumed consumption timespan of 100 years.

Adding another shade to the energy abundance picture is the environmental sustainability of each resource. In the United States, 87% of global carbon emissions derive from energy use (leaving 13% to construction and industrial processes) – divided roughly evenly between the electricity sector and the transportation sector[3]. Without decarbonization of our energy supply, the threat of climate destabilization is real. Emission of other pollutants and consumption of freshwater are additional sustainability considerations. [1] **see footnote*

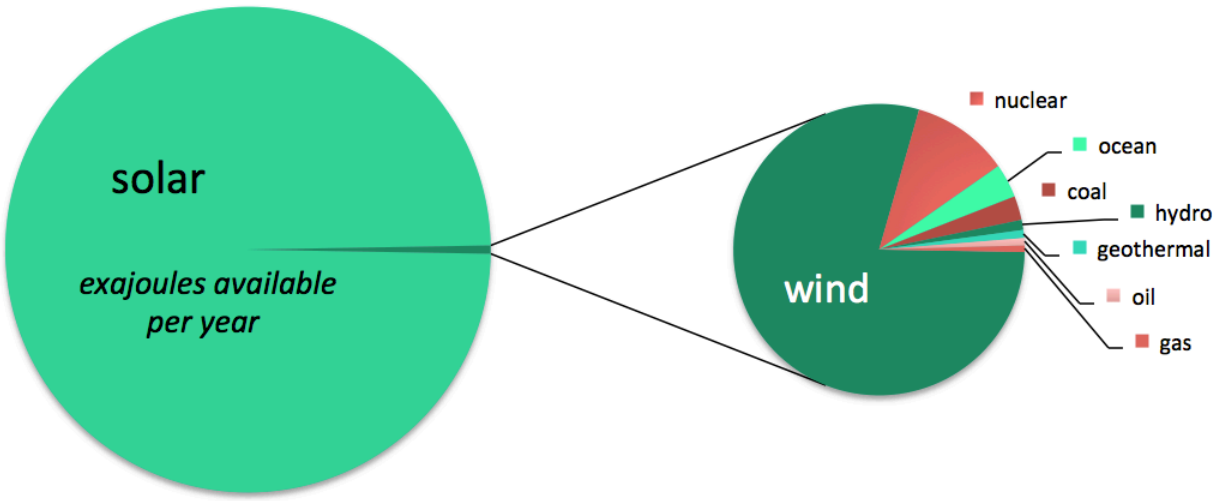

Figure 1-1. Available energy supply by raw resource, graphed in Joules, and assuming a 100-year timeline for fully depleting non-renewable resources. 2010 consumption is roughly equal to the 'ocean' wedge. Data compiled from [1,2,4].

The abundance of the solar resource is staggering, presenting 100-10,000 times more energy than other sources over a 100-yr timespan; 4,000 times as much power as we use today; orders of magnitude more than we can envision our society ever consuming. While each of these resources has an important role to play in our energy future, it is clear from the sheer abundance of solar energy that we must learn to harness it at scale if we are to keep up with our own consumption.

Solar energy can be harnessed in a variety of ways, from the growth of chemical energy supplies (plants for fuel) to the production of electricity (photovoltaics) to the generation of thermal energy (solar thermal). Electricity derived from solar thermal energy is limited by Carnot efficiency to be less than ~50% efficient and is typically closer to half that value[5]. Photosynthesis has never been demonstrated to be more than 8% efficient and has a theoretical efficiency of 15% or higher[6]. Photovoltaics can attain conversion efficiencies of 32% with a single bandgap and 68.8% in a tandem configuration[7,8].

---

[*] Beyond the scope of this dissertation are the additional and important energy considerations of intermittency (and the implied necessary load-shifting) and grid connectivity (to ensure smooth transmission of any distributed power source).

1.2 Photovoltaics

Of the solar energy technologies, photovoltaics are particularly appealing because of their rapid and modular deployability, their tolerance for water-constrained and diffuse-light environments, and their relatively high areal energy output. However, cost has prevented wide-scale adoption. Materials and manufacturing costs, durability, and power output are major cost drivers, in addition to financing and installation.

Three generations of photovoltaics have been described by a prominent photovoltaics expert, Martin Green[8]: The first is the generation of silicon photovoltaics – a relatively efficient proof-of-concept, deployed at high cost on a small scale. Industry has now reached the second generation, which consists of low-cost and low-efficiency photovoltaics. Third generation photovoltaics have been envisioned to have high conversion efficiency obtained at a very low cost, are expected to spur worldwide adoption of photovoltaics. As we work toward third generation photovoltaics, we must devise innovative ways to push the juxtaposed variables of cost and conversion efficiency in favorable directions.

The photovoltaic effect consists of 3 basic steps: absorption, charge separation and transport, and charge carrier collection[9]. When a semiconductor material absorbs a photon, an electron is excited to a higher-energy state, leaving behind an electron 'hole'. The absence of the negatively-charged electron gives the hole a positive charge. Both of these charge carriers have some mobility in the semiconductor, and in the absence of electronic asymmetry in the semiconductor, the holes and electrons are attracted and collide, re-emitting the energy radiatively or non-radiatively.

It is possible to achieve asymmetry (necessary for photovoltaic action) in a semiconductor through either a type-II heterojunction or a Schottky junction. In the heterojunction, asymmetry is induced by the relative conduction and valence band alignments between the two semiconductors forming the heterojunction. Cadmium telluride - cadmium sulfide is a common example of a heterojunction. In a Schottky junction, the relation of the semiconductor band edges to the work function of an electrical contact causes an energetic barrier for one charge carrier type, making it difficult for the carrier to move in that direction. Both of these junctions conduct excited electrons preferentially in one direction, and holes in the opposite direction. This allows for the collection of a net current under illumination.

Historically, high efficiency has been attained with single crystalline materials whose perfect lattices enable facile movement of charge carriers without risk of collision with performance-degrading defects. The fabrication of such large single crystals requires high-temperature and high-cost processes prohibitive to economical devices. Furthermore, the perfect single-crystal lattice (and therefore high carrier mobility) is required only in the through-film direction; the path that electrons and holes must travel. Improving crystallinity in-plane is not a significant boon to device performance.

In contrast to large single crystals, the fabrication of small single crystals, or colloidal **nanocrystals**, uses relatively lower temperatures and lower cost. A monolayer of single-crystalline nanoparticles should, in principle, act as a single-crystal device, allowing high carrier movement in the required direction (through-film), without spending unnecessary effort on improving carrier mobility in-plane. Additionally, processing a nanocrystal ink into a device could make use of inherently inexpensive manufacturing methods such as printing or spraying, eliminating the expensive vacuum processing techniques often used in thin-film photovoltaics.

1.3 A third generation photovoltaic architecture

This dissertation describes one possible architecture for third-generation photovoltaics (see Figure 1-2). The architecture leverages single-crystal rod-shaped nanocrystals carefully oriented in a thin film in an effort to achieve single-crystal performance in a low-cost solution-processed photovoltaic device. The work embodied in this quest includes colloidal self-assembly, thin film morphology quantification, on-chip cation exchange, crystallographic phase identification, and electrical characterization. A proof of principle is demonstrated, and a new body of questions about nanocrystal surfaces arises.

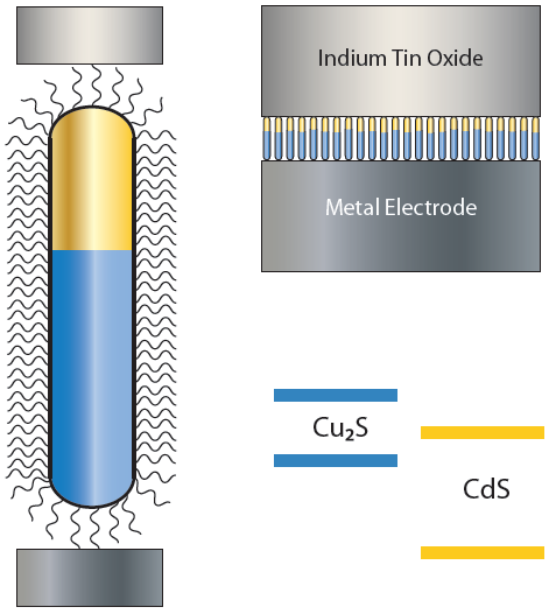

Figure 1-2. Schematic of one possible third generation photovoltaic architecture

1.3.1 Nanocrystals

Nanocrystals are small inorganic lattices measuring nanometers or tens of nanometers in diameter, which consist of hundreds to many thousands of atoms. Their size-tunable properties distinguish them from their bulk counterparts, and make them uniquely valuable in a variety of applications including optoelectronics (their size and shape determines their optical spectra *via* quantum confinement), catalysis (the shape of the crystal can select for dominant facets with higher reactivity), and biological sensing (the crystal surface and interior are independently tunable allowing for selective attachment)[10].

Semiconductor nanocrystals can be grown colloidally at relatively low temperatures (<350C), and can be size- and shape- tuned by growth time and by careful selection of the organic ligands that mediate crystal growth and ultimately passivate the nanocrystal surface, facilitating dispersion in solvent. In the case of wurtzite cadmium sulfide nanorods, the octadecylphosphonic acid ligand binds tightly to the side facets (parallel to the [001] axis), while incompletely passivating the (001) and (00-1) facets. This incomplete passivation leads to a high growth rate along the c-axis of the wurtzite crystal, giving it an elongated 'rod' shape[11]. This simple growth technique results in a nanocrystal ink of size- and shape- monodisperse crystals, which may be processed inexpensively into semiconducting devices.

The control of the shape and size of the nanocrystals affords a useful lever for controlling material properties. Hierarchical control of the arrangement of nanocrystals into a film provides yet another layer of control of semiconductor film properties. The study of self-assembly, in which nanoparticles are induced to form superlattices in 2 or 3 dimensions, began in 1995 with a seminal paper by Murray *et al.*[12] reporting spherical nanocrystal arrangement. Since then, the superlattice literature has continued to grow, but almost exclusively with <u>spherical</u> particle assembly – commonly using controlled destabilization of an evaporating nanocrystal ink.

Small-scale assembly of <u>rod-shaped</u> nanocrystals was first noticed by Peng and Talapin[11,13]. Ryan and Russell later demonstrated directed assembly with electric fields[14,15]. These qualitative studies showed vertical nanorod alignment over less than a square micron. For this assembly to be relevant to devices, it would need to be scaled by at least 8 orders of magnitude.

This scale was demonstrated (as described in Chapter 2) in cadmium sulfide nanorods by independently controlling the system temperature and the evaporation rate[16]. This simple and scalable process achieved an alignment of 96% vertical nanorods over one square centimeter. The device-scale vertical assembly of nanorods may enable a semiconductor thin film with single-crystal performance, but ultra-low cost.

The optimization and scaling of nanorod self-assembly would have been impossible without the development of a quantification technique capable of assessing centimeter-sized substrates. Electron microscopy is a useful and direct measurement of local alignment, but is impractical for the quantitative investigation of large substrates. Thin film morphology was assessed quantitatively (see Chapter 3) with grazing-incidence x-ray diffraction (GIXD), using a 2-stage data collection technique in combination with derived correction factors[17]. This morphology quantification method is general to any thin film, and has been used to assess inorganic thin-films, polymer films, and covalent organic frameworks.

1.3.2 Cu_2S-CdS

The original thin film photovoltaic device (second generation photovoltaic) was demonstrated the same year that the traditional silicon photovoltaics device (first generation) emerged: In 1954, Bell Labs announced the first practical solar cell, a p-n junction[18]; later that same year, Reynolds et al. announced a new chemistry consisting of a cadmium sulfide crystal with a copper contact[19,20], which had presumably diffused partway into the cadmium sulfide, creating a copper sulfide layer to form a type-II heterojunction. The electronic band alignments of a type-II heterojunction induce asymmetry that induces holes and electrons to move in opposite directions, providing the rectified electrical behavior necessary to create net photocurrent.

After the realization that the solid-state copper was diffusing into the CdS crystal in an ion-exchange reaction, the Clevite Corporation began developing more controllable processes of cation exchange[21]. By the 1970s, heterojunction efficiencies had reached nearly 10% and work was underway to improve long-term stability. However, the power to weight ratio of heavy CdS-Cu_2S couldn't compete with the incumbent Silicon devices employed by the aerospace industry, so with the end of the cold war and the end of the oil crisis of the 1970s, investment in photovoltaics tapered dramatically, leaving silicon to be supported by the emerging computing industry while other chemistries languished[19].

With the advent of Cu_2S and CdS nanocrystals over the last handful of years, and as issues of earth-abundance arise, there is renewed interest in the Cu_2S chemistry[22]. The cation exchange techniques of the 1970s[21] have been adapted to nanocrystal systems, using methanol as a solvent to extract (in the case of CdS$\rightarrow$$Cu_2S$) the Cd^{2+} ions from the lattice, for replacement by 2 Cu^+ ions. This method is found to be generalizable to PbS, Ag_2S, Hg_2S, Ag_2Se and Cu_2Se among others[23-27]. The small-interfacial-area heterojunctions can provide an additional benefit: lattice strain inherent in any epitaxial heterojunction is relieved over some characteristic distance by formation of a mismatch dislocation. The mismatch dislocation can act as a trap or a recombination site, degrading the performance of the heterojunction. With an interfacial area smaller than the characteristic distance of mismatch dislocations, the nano-heterojunction may function more perfectly than the same chemistry does in bulk.

If cation exchange could be used on an aligned array of CdS nanorods, we would form the type-II heterojunction demonstrated in 1954. However, we would have done this in an effectively single-crystal system, and with simpler manufacturing techniques than the vacuum processes traditionally used for the deposition of such films. Additionally, we may achieve higher performance than even single-crystal Cu_2S-CdS devices were able to attain (roughly 10% efficiency[28]) by use of small heterojunctions that evade mismatch dislocations. (An alternative to a heterojunction would be to select semiconductor-contact pairs to form a Schottky junction to achieve rectification in an aligned nanorod system.)

Research on Cu_2S nanocrystal photovoltaics may illuminate pathways to enhanced stability, or may provide analogous studies for ternary and quaternary related materials copper indium sulfide (CIS), copper indium gallium selenide-sulfide (CIGS), and copper zinc tin sulfide (CZTS).

1.3.3 Stability

The stability of any photovoltaic material must be carefully examined, since it must maintain performance for a minimum of 25 years in a harsh environment. In the case of nanomaterials, this reconnaissance ought to be even more cautious given the high surface-area-to-volume ratio that may exacerbate the effects of surface defects, provide greater opportunity for oxidation, and enable the stabilization of crystallographic phases not seen at room temperature in extended solids.

One important area of stability investigation is the size dependence of phase transition temperatures. The crystallographic phase diagram of a nanocrystal may vary from its bulk counterpart simply due to the high surface area of the small crystal; at the nanoscale, it is no longer appropriate to neglect the surface tension of crystal phases when calculating the free energy of a crystal. In the case of bulk Cu_2S, a phase transition from low- to high-chalcocite is observed at 104°C. This temperature is strongly depressed in nanocrystals, which exhibit the same transition at temperatures as low as 52°C, in the range of photovoltaic operating temperatures[29]. Because Cu_2S has superior photovoltaic properties in the low chalcocite phase, larger-diameter (>5nm) nanocrystals (with higher transition temperatures) will perform best in solar cells.

Another subject critical to stability is the chemical composition of the nanocrystal surface. Nanocrystal surfaces may cause an effective doping of the nanocrystal itself[30] or may provide recombination pathways for excited charge carriers. Ligands designed to passivate the nanocrystal surface must meet varying requirements at different stages of device fabrication, from bond strength to tail group solubility to electrical conductivity. These nanocrystal surface issues will need to be addressed if we are to pursue the noteworthy advantages of nanocrystalline photovoltaic devices.

1.4 Broader Implications

High-quality semiconductor thin film applications are not confined to the world of photovoltaics. Closely-related are photodetectors and light-emitting diodes, which would similarly benefit from high through-film carrier mobility, using size-tunable nanorods. Further intriguing is the use of vertical arrays of nanorods for memory applications, in which each 4-nanometer nanorod represents one bit of data. Additionally, with catalysts grown on the nanorod tips, a photocatalytic system may be equally within reach of the architecture described in this dissertation.

1.5 References

1. BP Statistical Review of World Energy June 2009. **2009**, 1–48.
2. *International Energy Outlook 2010*; U.S. Energy Information Adminitration, 2010.
3. EPA, U. S.; OAR; Division, C. C. Inventory of US GHG Emissions and Sinks: 1990-2009 - Executive Summary Standalone (EPA 430-S-11-001). **2011**, 1–28.
4. Tsao, J.; Lewis, N.; Crabtree, G. *Solar FAQs*; U.S. Department of Energy, Office of Basic Energy Science, 2006; pp. 1–24.
5. Crabtree, G. Solar energy conversion. *Physics Today* **2007**.
6. Walter, M. G.; Warren, E. L.; McKone, J. R.; Boettcher, S. W.; Mi, Q.; Santori, E. A.; Lewis, N. S. Solar Water Splitting Cells. *Chem. Rev.* **2010**, *110*, 6446–6473.
7. Shockley, W. Detailed Balance Limit of Efficiency of p-n Junction Solar Cells. *Journal of Applied Physics* **1961**.
8. Green, M. A. Third generation photovoltaics: Ultra-high conversion efficiency at low cost. *Prog. Photovolt: Res. Appl.* **2001**, *9*, 123–135.
9. Nelson, J. *The physics of solar cells*; 2003.
10. Alivisatos, A. Semiconductor clusters, nanocrystals, and quantum dots. *Science* **1996**.
11. Peng, X.; Manna, L.; Yang, W.; Wickham, J.; Scher, E.; Kadavanich, A.; Alivisatos, A. Shape control of CdSe nanocrystals. *Nature* **2000**, *404*, 59–61.
12. Murray, C.; Kagan, C. Self-organization of CdSe nanocrystallites into three-dimensional quantum dot superlattices. *Science* **1995**.
13. Talapin, D. V.; Shevchenko, E. V.; Murray, C. B.; Kornowski, A.; Förster, S.; Weller, H. CdSe and CdSe/CdS Nanorod Solids. *J. Am. Chem. Soc.* **2004**, *126*, 12984–12988.
14. Ryan, K. M.; Mastroianni, A.; Stancil, K. A.; Liu, H.; Alivisatos, A. P. Electric-Field-Assisted Assembly of Perpendicularly Oriented Nanorod Superlattices. *Nano Lett.* **2006**, *6*, 1479–1482.
15. Gupta, S.; Zhang, Q.; Emrick, T.; Russell, T. P. "Self-Corralling" Nanorods under an Applied Electric Field. *Nano Lett.* **2006**, *6*, 2066–2069.
16. Baker, J. L.; Widmer-Cooper, A.; Toney, M. F.; Geissler, P. L.; Alivisatos, A. P. Device-scale perpendicular alignment of colloidal nanorods. *Nano Lett.* **2010**, *10*, 195–201.
17. Baker, J. L.; Jimison, L. H.; Mannsfeld, S.; Volkman, S.; Yin, S.; Subramanian, V.; Salleo, A.; Alivisatos, A. P.; Toney, M. F. Quantification of thin film crystallographic orientation using X-ray diffraction with an area detector. *Langmuir* **2010**, *26*, 9146–9151.
18. Chapin, D.; Fuller, C. A New Silicon p-n Junction Photocell for Converting Solar Radiation into Electrical Power. *Journal of Applied Physics* **2004**.
19. Loferski, J. The first forty years: a brief history of the modern photovoltaic age. … *in photovoltaics: research and applications* **1993**.
20. Reynolds, D.; Leies, G.; Antes, L.; Marburger, R. Photovoltaic Effect in Cadmium Sulfide. *Phys. Rev.* **1954**, *96*, 533–534.
21. Cook, W.; Shiozawa, L. Relationship of copper sulfide and cadmium sulfide phases. *Journal of Applied Physics* **1970**.
22. Wu, Y.; Wadia, C.; Ma, W.; Sadtler, B.; Alivisatos, A. P. Synthesis and Photovoltaic Application of Copper(I) Sulfide Nanocrystals. *Nano Lett.* **2008**, *8*, 2551–2555.
23. Son, D. H.; Hughes, S. M.; Yin, Y.; Paul Alivisatos, A. Cation exchange reactions in ionic nanocrystals. *Science* **2004**, *306*, 1009–1012.
24. Robinson, R. D.; Sadtler, B.; Demchenko, D. O.; Erdonmez, C. K.; Wang, L. W.; Alivisatos, A. P. Spontaneous Superlattice Formation in Nanorods Through Partial Cation Exchange. *Science* **2007**, *317*, 355–358.
25. Sadtler, B.; Demchenko, D. O.; Zheng, H.; Hughes, S. M.; Merkle, M. G.; Dahmen, U.; Wang, L.-W.; Alivisatos, A. P. Selective facet reactivity during cation exchange in cadmium sulfide nanorods. *J. Am. Chem.*

Soc. **2009**, *131*, 5285–5293.

26. Luther, J. M.; Zheng, H.; Sadtler, B.; Alivisatos, A. P. Synthesis of PbS Nanorods and Other Ionic Nanocrystals of Complex Morphology by Sequential Cation Exchange Reactions. *J. Am. Chem. Soc.* **2009**, *131*, 16851–16857.
27. Dloczik, L.; Koenenkamp, R. Nanostructured metal sulfide surfaces by ion exchange processes. *Journal of Solid State Electrochemistry* **2004**, *8*, 142–146.
28. Stanley, A. G. Cadmium sulfide solar cells. *In: Advances in materials and device research. New York, Academic Press, Inc. (Applied Solid State Science. Volume 5), 1975, p. 251-366*. **1975**, *5*, 251–366.
29. Rivest, J. B.; Fong, L.-K.; Jain, P. K.; Toney, M. F.; Alivisatos, A. P. *Size Dependence of a Temperature-Induced Solid-Solid Phase Transition in Copper(I) Sulfide*; submitted, 2011.
30. Talapin, D. V. PbSe Nanocrystal Solids for n- and p-Channel Thin Film Field-Effect Transistors. *Science* **2005**, *310*, 86–89.

The following was reproduced with permission from: Jessy Baker (Rivest), Asaph Widmer-Cooper, Michael F Toney, Phillip L Geissler, and A. Paul Alivisatos, "Device-Scale Perpendicular Alignment of Colloidal Nanorods" Nano Letters **2010**, *10* (1), pp 195– 201.

Copyright 2010 American Chemical Society.

* * * * *

Acknowledgements. We thank Steven Volkman and Shong Yin for their help at the Stanford Synchrotron Radiation Lightsource facilities. We thank Jen Dionne for SEM images taken at Lawrence Berkeley National Labs' Molecular Foundry, and Munekazu Motoyama for AFM roughness measurements. We thank PK Jain, KM Tye, DJ Milliron, JJ Urban, JM Luther, CL Choi, JE Millstone and B Sadtler for helpful discussions and critical review of our manuscript. This work was funded by the Helios Solar Energy Research Center which is supported by the Director, Office of Science, Office of Basic Energy Sciences, Materials Sciences and Engineering Division, of the U.S. Department of Energy under Contract No. DE-AC02-05CH11231. Portions of this research were carried out at the Stanford Synchrotron Radiation Lightsource, a national user facility operated by Stanford University on behalf of the U.S. Department of Energy, Office of Basic Energy Sciences. Personnel expenses were supported in part by the National Science Foundation Graduate Fellowship.

Chapter 2

Device-Scale Perpendicular Alignment of Colloidal Nanorods

2.1 Introduction

Colloidal nanocrystals offer a potential route to realizing low-cost solution-processed electronic devices. In particular, with their size-tunable properties, single-crystallinity, and inexpensive synthesis, semiconductor nanoparticles could enable improved optoelectronic devices. To date, however, the performance of nanoparticle devices has been limited, in large part, by the number of interfaces that charge carriers encounter before they can be collected; each interface presents an opportunity for recombination and subsequent charge loss or relaxation. An ideal film would appear as a single-crystal to charge carriers, but would maintain solution-processability and therefore low manufacturing cost. This has been attempted with nanowire arrays[1-3], which can have single-crystal properties in the through-film direction (necessary for optoelectronics), but such arrays have met with only partial device success due to the low nanowire packing density and difficulty of incorporating semiconductor material between wires. Using colloidal nanocrystals, researchers have explored carrier mobility and device performance in the context of low-resistivity percolation networks. Improving the percolation network (low-resistivity pathway for charge carriers) has steadily improved performance as devices have evolved from using spheres to randomly-oriented rods to hyperbranched particles[4,5]. An ideal device geometry would consist of a monolayer of vertically oriented rods (perpendicular to substrate) spanning the full thickness of the film. While vertical nanowires have been formed on substrates using batch processing[6-9], the aim of this work was to achieve a perpendicular morphology in one step using solution-processable nanocrystals with no pre-patterning requirements or substrate restrictions.

Several reports have presented the perpendicular alignment of nanorods on a small scale (mm^2s)[10-16], but larger areas necessary for devices have not been reported quantitatively, nor is there a firm understanding of the underlying physical principles directing self-assembly, which would facilitate

rational design. A key component missing from the literature until recently is large-scale quantification of nanorod orientation[17]. Here, we report a slow-drying method for self-assembly of colloidal semiconductor nanorods resulting in their device-scale perpendicular alignment. We explore the self-assembly parameter space, and discuss the important role kinetics plays in alignment. This assembly method is general to a variety of substrates and can be expanded to the square centimeter scale.

2.2 Experimental Methods of Nanorod Assembly

In this work, nanorod films were produced with both short- and long-range order by controlling the evaporation of a solution of cadmium sulfide (CdS) nanorods (Figure 2-1). CdS nanorods (4nm in diameter, tunable 30-100nm in length, with surfaces passivated by octadecylphosphonic acid) were used in these studies due to the well-established synthesis[18] of single-crystal samples monodisperse in size and shape. Before alignment, the nanorods were stored air-free, and rod concentrations were measured by UV-vis absorption calibrated with inductively coupled plasma mass spectrometry. With a slow evaporation rate (<1mm/min meniscus speed across substrate), an elevated temperature (55°C), and an appropriate substrate (for example, silicon nitride), nanorods oriented vertically. (See Appendix I for further details.) To better understand the key parameters controlling self-assembly and thus aid rational device design, electron microscopy images were paired with a diffraction measurement technique representative of full-film morphology.

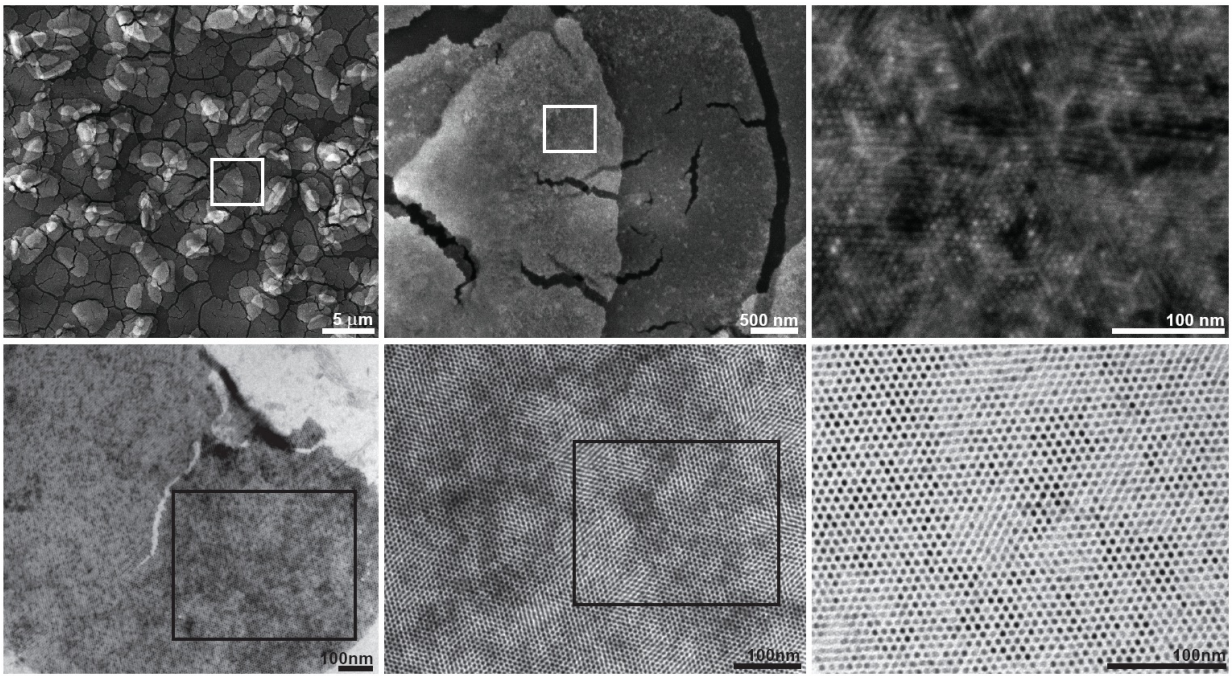

Figure 2-1. Electron microscopy images of large vertically oriented rod domains with progressive zoom from left to right. Top/bottom row: SEM/TEM images. Regions of higher contrast correspond to multiple monolayers. At this scale, assembly is difficult to judge quantitatively with electron microscopy.

Assembly of quantum ***dots*** can be assessed with a small-angle x-ray diffraction measurement (which probes the particle-to-particle periodicity, rather than lattice periodicity in individual nanoparticles) because particle rotational orientation is unimportant; only positional information is needed[19]. For information about nanocrystal crystallographic orientation, and for facile data interpretation, wide-angle diffraction is an alternative technique. In some cases, these methods are complementary.

2.3 Quantification of the Assembly Parameter Space

Grazing-incidence wide-angle x-ray diffraction (GIXD) enables morphological quantification of assembled nanoparticle thin-films by leveraging the anisotropic lattice common to many semiconductor nanocrystals (Figure 2-2). Here, in the case of cadmium sulfide (wurtzite lattice), the long axis of the nanorod corresponds to the c-axis ((002) direction) in the rod's lattice. Therefore, knowledge of the *lattice* orientation translates to knowledge of the *rod* orientation. While any diffraction peak could be used to monitor rod orientation, (002) was chosen because of the sharp signal afforded by its orientation along the long axis of the rod. (002) diffraction from rods oriented parallel to the substrate falls at the horizon of the Bragg ring in the diffraction pattern (Figure 2-2 c and d) and corresponds to rod orientation angle $\omega=\pm 90^{o}$. Diffraction from rods oriented perpendicular to the substrate falls at the top of the Bragg ring, where ω approaches 0°. Radial cross-sections of the diffraction pattern taken at different angles show the degree of anisotropy in nanorod orientation (Figure 2-2e and f). Integrating diffraction intensity as a function of angle ω along the circumference of the (002) Bragg ring gives us an orientation distribution function (Figure 2-2g and h).[20]

By using a large X-ray beam size and rastering the beam across the substrate, we obtain an orientation distribution function (ODF) representative of the entire film. By integrating the normalized and intensity-corrected ODF[21] within a range of angles of interest, one can say with precision how many rods are oriented within this range. Here, vertical is considered to be $\pm 20^{o}$, as this amount of tilt corresponds to a small change in film thickness of only 6%.

Strong texture is observed (intensity variation around Bragg ring) in the diffraction patterns from films of vertically oriented nanorods (Figure 2-2d), corresponding to a narrow ODF indicating vertical nanorod alignment. The width of the orientation peaks may be due to contraction of the ligand shell upon final solvent drying, causing rods to lean slightly. This could be understood as a cumulative effect of the shrinkage of ligands on many rods (approximately 0.4nm per rod), creating (over the area of tens of rods) enough space for either cracks or rod inclination (see cracks and tilting rods in Figures 2-1 and AI-3, respectively).

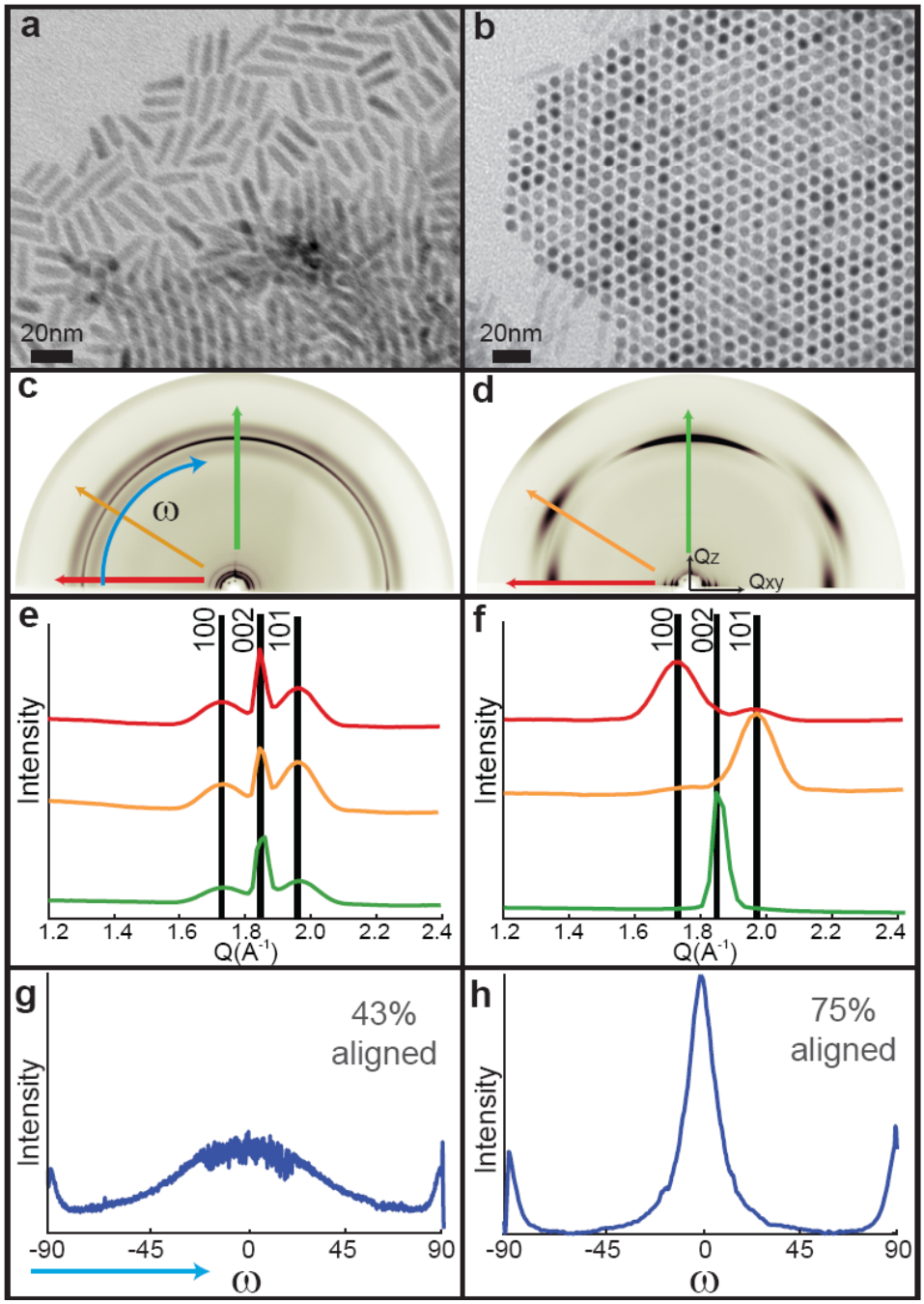

Figure 2-2. X-ray diffraction is a necessary complement to electron microscopy for film morphology assessment. (a) and (b) TEM images of near-isotropic and vertically aligned nanorods. The c-axis of the anisotropic wurtzite lattice is oriented along the long axis of nanorods, enabling detection of rod orientation with wide-angle diffraction. (c) and (d) Diffraction patterns corresponding to morphologies (a) and (b). Intensity collected near the horizon of the (002) (middle) Bragg ring is diffraction from horizontally oriented rods, while intensity near the top is from vertically oriented rods. Low-Q intensity is from small-angle diffraction events (superlattice). (e) and (f) Radial cross-sections of diffraction patterns shown in (c) and (d) indicate an angle dependence only in the case of an oriented film. (g) and (h) Orientation distribution obtained by plotting the intensity of rocking and grazing data along the (002) Bragg rings in (c) and (d) as a function of ω[21,22]. From these plots, we can determine the percentage of rods vertically oriented (within $\pm$ 20° of the normal to substrate): 43% and 75% are vertically aligned in (g) and (h). The tails around ω=±90° in (h) indicate that some of the rods lie horizontally.

To quantitatively explore the dependence of rod alignment on key assembly parameters (temperature, aspect ratio, and van der Waals (vdW) interaction with the substrate (Figure 2-3)), we used the GIXD analysis described in Figure 2-2 together with theoretical calculations of interaction energies and diffusion constants. Elucidation of the contributions from entropy, enthalpy, and kinetics gave us insight into the physics governing rod self-assembly. The standard experimental conditions for data plotted in Figure 2-3 were: 55° C nanocrystal solution temperature, rod aspect ratio 6.4, rod diameter 4nm, polydispersity s=12%, tetrachloroethylene as solvent, Si_3N_4 substrates, and evaporation rates resulting in ~1mm/min meniscus speeds across the substrate. The total number of nanorods in solution was chosen to provide at least one full monolayer of vertically aligned rods on the final substrate. To avoid aggregation, experiments were performed in the presence of excess surfactant (see Appendix I for additional experimental details).

2.3.1 System Temperature

Heating the nanorod solution 10-40°C above room temperature (while keeping the evaporation rate constant) favored perpendicular rod alignment (Figure 2-3a), consistent with previous qualitative reports[10,14]. This may point to a kinetic effect and/or competition between entropic and energetic driving forces. The rotational and translational diffusion constants (D^i) for rod-shaped particles in solution[23] depend on temperature as $D^i \propto T/\eta_s$, where η_s is the shear viscosity. Since η_s decreases upon heating, self-assembly will become faster at higher temperature, effectively giving the system more time to lower its free energy. In this case, the increase in alignment upon heating would indicate that the perpendicularly aligned state is thermodynamically stable. The trend in Figure 2-3a could also indicate that there are entropic effects driving perpendicular alignment that are opposed by enthalpic interactions. It is well known that hard rod-shaped particles will spontaneously undergo orientational ordering when their containing volume shrinks (e.g. due to solvent evaporation), because the gain in positional entropy on alignment (associated with reducing the total excluded volume) more than compensates for the loss in rotational entropy[24]. Li *et al.* have observed similar liquid-crystalline behavior for CdSe nanorods[25], which have analogous physical properties to the CdS nanorods used in the present study. In Li's work, the isotropic-nematic phase boundary was found to be weakly temperature dependent over the range considered (some of this data is plotted in Figure 2-3a for comparison), indicating that the entropically driven ordering may be opposed by enthalpic interactions that become less important at higher temperature.

2.3.2 Nanorod Aspect Ratio

Similar to previous reports, we found that low aspect ratio (AR) rods aligned more readily than rods with high AR (Figure 2-3b). While we were able to align rods with ARs up to 15 (higher than any published report), we were unable to identify a set of parameters that achieved detectable vertical orientation with nanorods of AR approaching 25. This is likely a predominantly kinetic effect. The short-time (non-interacting) rotational diffusion constant D^{rot} for rod-shaped particles in solution is

strongly dependent upon their length L[23]. For the size of nanorods considered here $D^{rot} \propto \ln(L)/L^3$) and decreases by ~97% going from an AR of 5 to 25. The long-time rotational diffusion (considering rod-rod interactions) should follow a similar trend (see Appendix I). Based on thermodynamic considerations alone, we expect little change in alignment with increasing AR. The relative energy per particle for a monolayer of CdS rods aligned perpendicular and parallel to Si_3N_4 changes little with AR in the range considered here (see Appendix I). It is also known that for entropic reasons longer rods order orientationally at lower volume fraction. The interaction energy between the rod (both the nanocrystal and the ligands) and the substrate in solution also plays a role in rod self-assembly, as shown by its effect on alignment in Figure 2-3c (details of the vdW energy calculations are in Appendix I). A strongly attractive interaction encourages rods to maximize their area of contact with the substrate by lying parallel to it. As this attraction is decreased, a stronger preference for perpendicular alignment is observed. Similar to Titov[27], we found that the substrate influenced alignment. However, our experimental results show that the alignment is not a simple function of the substrate Hamaker constant, and that in general alignment is not strongly dependent upon the choice of substrate (see also Figure 2-4) over the range of interactions we considered. Based on theoretical analysis, we suggest that the ligands bound to the nanorods play an important energetic role. The vdW energies calculated in solution are typically not much larger than thermal energy, primarily because the ligands prevent the crystalline cores from interacting strongly with each other and with the substrate. Note that the typical separation between rods surfaces in our experiments is 3.7 nm. This result explains why perpendicular alignment is only weakly substrate dependent. The inclusion of the ligands in our analysis also offers an explanation for the subtle dependence of alignment on the choice of substrate. If the Hamaker constant of the substrate is greater than that of the solvent then the ligands are effectively repelled by the substrate at close range. This effect leads to a non-monotonic dependence of the rod-substrate interaction energy on the substrate Hamaker constant, as shown by the curve in Figure 2-3c.

2.3.3 vdW Interactions

Our calculations also show that ligand-ligand and ligand-substrate interactions are large and dominant in the absence of solvation (100s of kT). While it is clear that self-assembly does not occur after drying is complete, fluctuations in solvent density near the liquid-vapor interface could activate these strong attractions in the late stages of assembly[28,29]. The visible film contraction and cracking that occurs at the final stage of drying is also consistent with the large increase in ligand vdW interactions that we calculate upon desolvation. Finally, our calculated interaction energies (in both vacuum and solution) suggest that perpendicular alignment should be largely independent of the choice of nanocrystal material. Indeed, reports of self-assembly demonstrate vertical alignment of CdS[12], CdSe[15], CdS-CdSe heterostructures[14], Cu_2S[30], Ag_2S[30], and Au[31] rods.

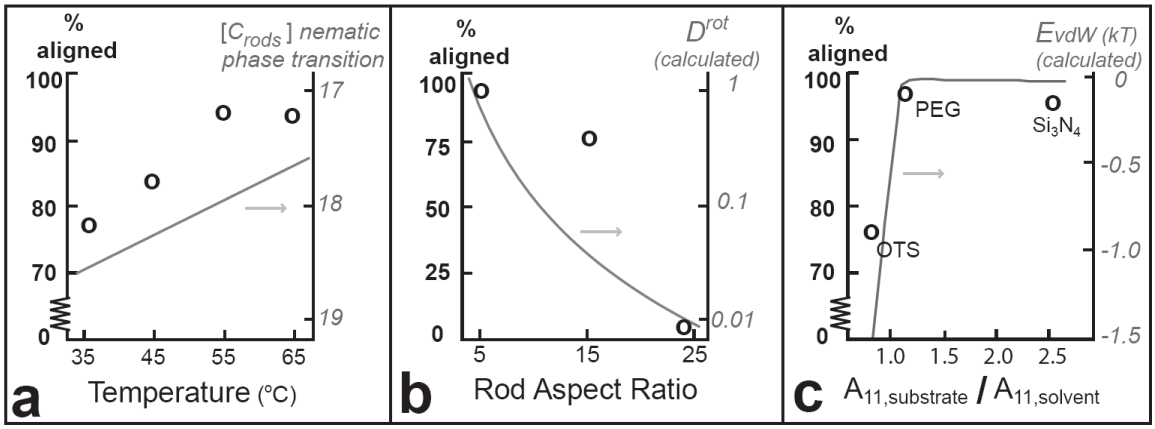

Figure 2-3. Entropy, enthalpy, and kinetics all contribute to self-assembly. a) An elevated temperature increases the percentage of vertically aligned rods (o's), and decreases the required rod concentration (volume %) for a nematic (ordered) phase transition (line)[25]. This temperature dependence demonstrates kinetic and/or entropic contributions to self-assembly. b) Rods with higher aspect ratio are more difficult to align (o's). The estimated rotational diffusion constants (normalized by $D^{rot(AR=5)}$) similarly decrease with increasing aspect ratio (line) suggesting that this is a kinetic effect. c) The percentage of vertically aligned rods (o's) is a non-monotonic function of the substrate Hamaker constant ($A_{substrate}$) and can be explained by the rod-substrate interaction strength. Substrates were silicon nitride TEM membranes, in some cases functionalized with self-assembling monolayers (SAMs): octadecyltrichlorosilane (OTS) & polyethylene glycol (PEG). A stronger attraction, calculated as the vdW interaction in solution for a rod parallel to the substrate (line), results in more horizontally oriented rods (o's). Diffraction results were corroborated qualitatively with TEM images of each sample. Error bars fall within each data point. Identical nanocrystal samples and preparation procedures were used for each temperature and substrate study for consistency. Rods with AR=6.4 had a width polydispersity of 10%, and a length polydispersity of 12% (used also for temperature and substrate studies) Rods with AR=15.7 had a width polydispersity of 12.9% and a length polydispersity of 8.5%. Rods with AR=23.75 had both length and width polydispersities of 10%.

In summary, the strong trend counter to thermodynamic expectations that is achieved by aspect ratio variation (as compared to temperature or substrate variation) suggests that kinetics plays a dominant role in rod self-assembly. While the analysis presented here provides valuable insight into this process, a complete description will need to address the kinetic interplay among evaporation, concentration, aggregation, deposition, and flow that ultimately determines film structure and particle orientation. Drying-mediated self-assembly is inherently a complex dynamical process that involves phase transitions in both nanorod and solvent density, i.e., slowly relaxing systems far from equilibrium.

Our quantitative exploration of factors affecting alignment allowed us to optimize assembly conditions and thereby vertically align nanorods on a variety of substrates (Figure 2-4); low aspect-ratio rods and an elevated temperature were used to obtain better vertical nanorod alignment. Because the rod-substrate interactions are relatively weak, we were able to align rods on a wide range of substrates. Wide peaks in the ODF were observed for rough substrates (indium tin oxide (ITO) and rough silicon nitride (Si_3N_4); RMS roughness ~ 1.2nm and 1.7nm respectively), while sharper peaks were observed for smooth substrates (Si_3N_4 RMS roughness 0.5nm), demonstrating that rough surfaces do not significantly disturb rod alignment, but merely broaden the orientation distribution; rough and smooth Si_3N_4 substrates alike had only 1-3% of rods oriented horizontally (within 20° of

the substrate plane). Interestingly, the Si_3N_4 substrates with a PEG SAM (polyethylene glycol self-assembling monolayer) provided the best vertical alignment, with up to 95% of the rods vertically aligned, consistent with the vdW interaction data in Figure 2-3c. The variety of substrates on which rods have been demonstrated to self-assemble with a high degree of alignment points further to the generality of our method; both rods and substrates of varying compositions can participate in the drying-mediated self-assembly described here.

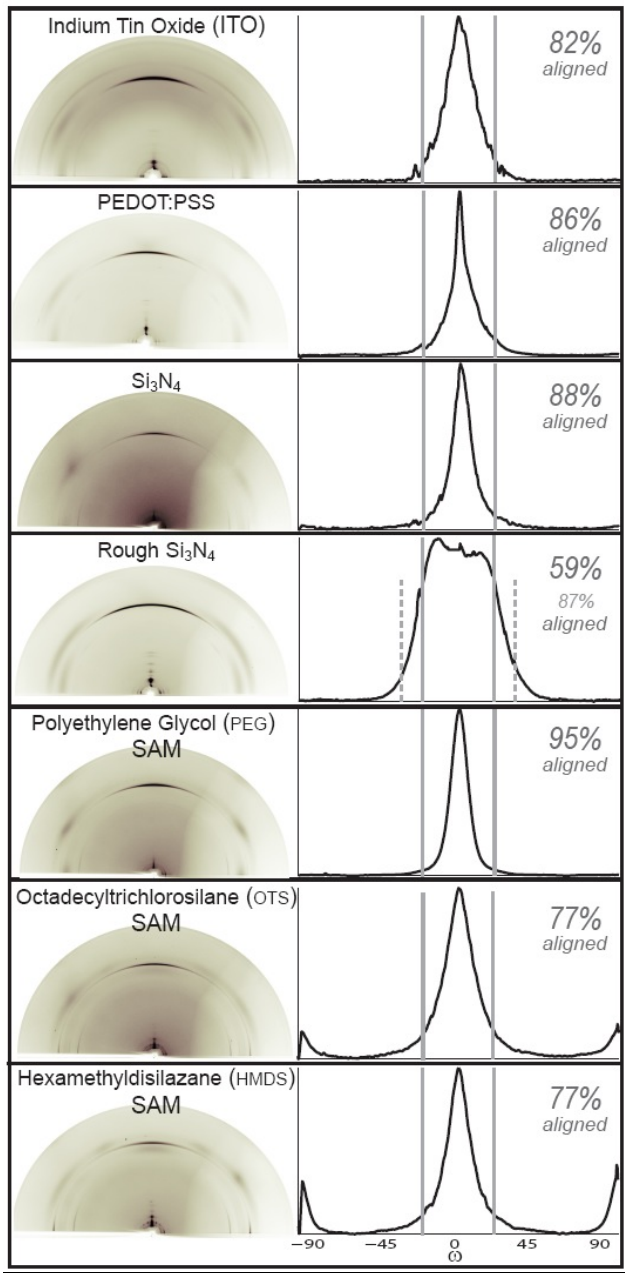

Figure 2-4. Substrate generality is shown: diffraction patterns and corresponding orientation distribution functions for each substrate. Percent vertical alignment (shown on right-hand side) is calculated by integration of the orientation distribution function between ±20°. A rough substrate results in a wider angular distribution for aligned rods. On OTS and HMDS substrates, we can see significant tails indicating horizontally oriented rods. Substrates here are ~7mm^2. Nanocrystal sample used was identical for each substrate, for fair comparison.

2.4 Device-Scale Assembly

We further show scaling of our technique to larger areas, achieving 96% alignment of the nanorods on a 1cm^2 substrate (Figure 2-5). By adapting techniques from photonic crystal assembly[32] film quality was improved in terms of its uniformity in thickness and a reduction in crack size; the substrate was carefully cleaned and the evaporation rate was reduced to <1mm/min meniscus speed (across substrate). A substrate tilt angle of 5° provided a single meniscus extended across the substrate during drying, producing a uniform film of aligned nanorods across the entire area.

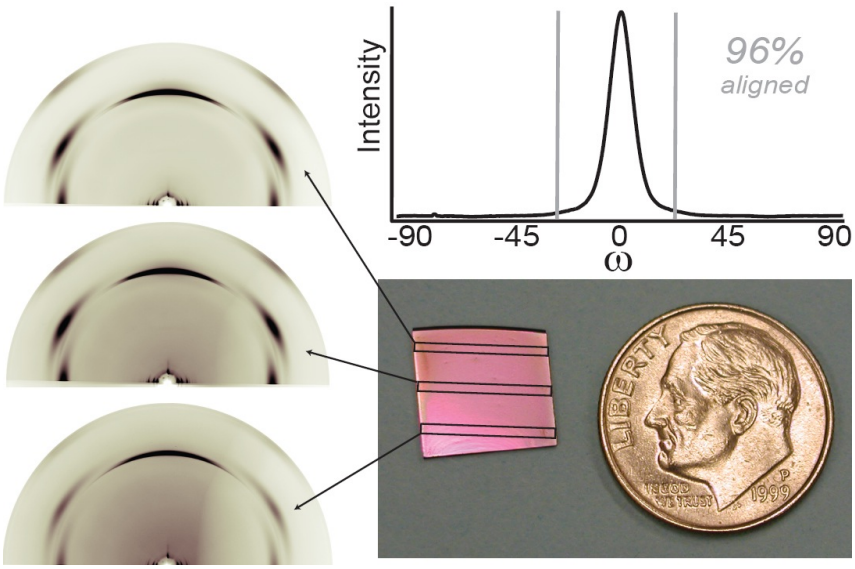

Figure 2-5. This self-assembly technique enables nanorod alignment on a device scale (1cm^2). Diffraction patterns corresponding to different areas on the substrate demonstrate uniformity across the film. Integrated intensity (ODF) from these diffraction patterns shows that we are able to achieve 96% vertical alignment on this silicon nitride substrate, pictured here next to a dime.

These large-area films comprise an assembly of many smaller domains. We found that in addition to vertical orientation, the rods in each of these domains were rotationally ordered with respect to each other about their c-axis (with ±15° leeway for rotation about this axis). Selected area wide-angle electron diffraction shows this formation of a supercrystal in two dimensions (see Appendix I Figure AI-5). Because wurtzite nanorods are known to have an approximately hexagonal cross section[33], their faceting might induce the rotational order observed. This result indicates that by probing an entire domain one could investigate nanoscale properties as a function of the crystal axis, currently impossible with colloidal nanorods randomly oriented either in solution or in dried films.

Further improvement in film quality will facilitate integration of these films in devices. Also, with further insight into the rod self-assembly mechanism, it may be possible to achieve alignment of rods with higher aspect ratio. This in turn would expand the applicability of this technique by making it possible to synthesize monolayer films of selectable thickness. We have characterized key self-assembly parameters, exploring the importance of enthalpy, entropy, and kinetics, and we

suggest that kinetics is the dominant effect that can be modified by varying experimental parameters. This exploration led us to vertically align nanorods on many device-relevant substrates, and at the centimeter scale. Ultimately, this advance may play a critical role in the development of inexpensive, solution-processed optoelectronics with performance matching that of bulk semiconductor devices.

2.5 References

1. Law, M., Greene, L. E., Johnson, J. C., Saykally, R. & Yang, P. Nanowire dye-sensitized solar cells. **4**, 455-459 (2005).
2. Greene, L. E., Law, M., Yuhas, B. D. & Yang, P. ZnOâˆ’TiO2 Coreâˆ’Shell Nanorod/P3HT Solar Cells. *The Journal of Physical Chemistry C* **111**, 18451-18456 (2007).
3. Fan, Z. et al. Three-dimensional nanopillar-array photovoltaics on low-cost and flexible substrates. **8**, 648-653 (2009).
4. Huynh, W. U., Dittmer, J. J. & Alivisatos, A. P. Hybrid nanorod-polymer solar cells. *Science* **295**, 2425-2427 (2002).
5. Gur, I., Fromer, N. A., Chen, C. P., Kanaras, A. G. & Alivisatos, A. P. Hybrid solar cells with prescribed nanoscale morphologies based on hyperbranched semiconductor nanocrystals. *Nano Letters* **7**, 409-414 (2007).
6. Trentler, T. J. et al. Solution-Liquid-Solid Growth of Crystalline Iii-V Semiconductors - an Analogy to Vapor-Liquid-Solid Growth. *Science* **270**, 1791-1794 (1995).
7. Hu, J. T., Odom, T. W. & Lieber, C. M. Chemistry and physics in one dimension: Synthesis and properties of nanowires and nanotubes. *Accounts of Chemical Research* **32**, 435-445 (1999).
8. Chen, C. C. & Yeh, C. C. Large-scale catalytic synthesis of crystalline gallium nitride nanowires. *Advanced Materials* **12**, 738-+ (2000).
9. Morales, A. M. & Lieber, C. M. A laser ablation method for the synthesis of crystalline semiconductor nanowires. *Science* **279**, 208-211 (1998).
10. Talapin, D. V. et al. CdSe and CdSe/CdS nanorod solids. *Journal of the American Chemical Society* **126**, 12984-12988 (2004).
11. Peng, X. G. et al. Shape control of CdSe nanocrystals. *Nature* **404**, 59-61 (2000).
12. Ryan, K. M., Mastroianni, A., Stancil, K. A., Liu, H. T. & Alivisatos, A. P. Electric-field-assisted assembly of perpendicularly oriented nanorod superlattices. *Nano Letters* **6**, 1479-1482 (2006).
13. Ahmed, S. & Ryan, K. M. Self-assembly of vertically aligned nanorod supercrystals using highly oriented pyrolytic graphite. *Nano Letters* **7**, 2480-2485 (2007).
14. Carbone, L. et al. Synthesis and micrometer-scale assembly of colloidal CdSe/CdS nanorods prepared by a seeded growth approach. *Nano Letters* **7**, 2942-2950 (2007).
15. Gupta, S., Zhang, Q. L., Emrick, T. & Russell, T. P. "Self-corralling" nanorods under an applied electric field. *Nano Letters* **6**, 2066-2069 (2006).
16. Ahmed, S. R., K.M. Vertical Aligned Nanorod Assembly by Electrophoretic Deposition from Organic Solvents. *Mater. Res. Soc. Symp. Proc.* (2009).
17. Breiby, D. W. et al. Biaxially Oriented CdSe Nanorods. *Langmuir* **25**, 10970-10974 (2009).
18. Peng, Z. A. & Peng, X. G. Formation of high-quality CdTe, CdSe, and CdS nanocrystals using CdO as precursor. *Journal of the American Chemical Society* **123**, 183-184 (2001).
19. Korgel, B. A., Fullam, S., Connolly, S. & Fitzmaurice, D. Assembly and self-organization of silver nanocrystal superlattices: Ordered "soft spheres". *Journal of Physical Chemistry B* **102**, 8379-8388 (1998).
20. Diffraction data was taken at the Stanford Synchrotron Radiation Lightsource on beamline 11-3 (wavelength 0.987 Angstroms) using a MAR345 image plate area detector at a distance of 400mm from the sample.
21. Baker, J. L.; Jimison, L.H.; Mannsfeld, S.; Volkman, S.; Yin, S.; Subramanian, V.; Salleo, A.; Alivisatos, A.P.; Toney, M.F. Quantification of Thin Film Crystallographic Orientation Using X-Ray Diffraction with an Area Detector. *Langmuir*, **2010**, *26* (11), pp 9146–9151
22. Toney, L. H. J. A. S. M. L. C. D. P. B. M. F. Correlating the microstructure of thin films of poly[5,5-bis(3-dodecyl-2-thienyl)-2,2-bithiophene] with charge transport: Effect of dielectric surface energy and thermal annealing. *Physical Review B* **78** (2008).
23. Tirado, M. M., Martinez, C. L. & Delatorre, J. G. Comparison of Theories for the Translational and Rotational Diffusion-Coefficients of Rod-Like Macromolecules - Application to Short DNA Fragments. *Journal of Chemical Physics* **81**, 2047-2052 (1984).

24. Onsager, L. The Effects of Shape on the Interaction of Colloidal Particles. *Ann. N.Y. Acad. Sci.* **51**, 627-659 (1949).
25. Li, L. S., Marjanska, M., Park, G. H. J., Pines, A. & Alivisatos, A. P. Isotropic-liquid crystalline phase diagram of a CdSe nanorod solution. *Journal of Chemical Physics* **120**, 1149-1152 (2004).
26. Dijkstra, M., van Roij, R. & Evans, R. Wetting and capillary nematization of a hard-rod fluid: A simulation study. *Physical Review E* **6305**, - (2001).
27. Titov, A. V. & Kral, P. Modeling the Self-Assembly of Colloidal Nanorod Superlattices. *Nano Letters* **8**, 3605-3612 (2008).
28. Rein ten Wolde, P., Sun, S. X. & Chandler, D. Model of a fluid at small and large length scales and the hydrophobic effect. *Physical Review E* **65**, 011201 (2001).
29. Rabani, E., Reichman, D. R., Geissler, P. L. & Brus, L. E. Drying-mediated self-assembly of nanoparticles. *Nature* **426**, 271-274 (2003).
30. Sadtler, B. Personal communication. (Spring 2009).
31. Khanal, B. Personal Communication. (Summer 2009).
32. Adachi, E., Dimitrov, A. S. & Nagayama, K. Stripe Patterns Formed on a Glass-Surface During Droplet Evaporation. *Langmuir* **11**, 1057-1060 (1995).
33. Manna, L., Scher, E. C. & Alivisatos, A. P. Shape control of colloidal semiconductor nanocrystals. *Journal of Cluster Science* **13**, 521-532 (2002).

The following was reproduced with permission from: Jessy Baker (Rivest), Leslie H Jimison, Stefan Mannsfeld, Steve Volkman, Shong Yin, Vivek Subramanian, Alberto Salleo, A Paul Alivisatos, and Michael F Toney, "Quantification of Thin Film Crystallographic Orientation using X-ray Diffraction with an Area Detector" Langmuir **2010**, *26* (11), pp 9146– 9151.

Copyright 2010 American Chemical Society.

* * * * *

Acknowledgements. This work was funded by the Helios Solar Energy Research Center, which is supported by the Director, Office of Science, Office of Basic Energy Sciences, Materials Sciences and Engineering Division, of the U.S. Department of Energy under Contract No. DE-AC02-05CH11231. Portions of this research were carried out at the Stanford Synchrotron Radiation Lightsource, a national user facility operated by Stanford University on behalf of the U.S. Department of Energy, Office of Basic Energy Sciences. We gratefully acknowledge financial support from the National Science Foundation in the form of a Career Award (AS) and Graduate Student Fellowship Personnel expenses (JLB, LHJ).

Chapter 3

Quantification of Thin Film Crystallographic Orientation Using X-ray Diffraction with an Area Detector

3.1 Introduction

The optical and electronic properties of polycrystalline and semicrystalline materials are highly dependent on the materials' morphology. When these properties are anisotropic in the single crystal form, the corresponding bulk properties of the poly- or semi-crystalline material are often dependent upon the orientation distribution of the crystallites.[1] As efforts are made to optimize the electrical and optical properties of functional, solution-processed polycrystalline films used for thin film transistors, solar cells, and other emerging technologies, it is necessary to fully characterize the orientation distribution, or texture, of the crystallites. There has been much effort devoted to correlating the microstructure and properties of thin films (<100 nm) of nanostructured organic semiconductors [2-7] and inorganic semiconducting nanoparticles[8, 9], but the collection of complete texture information is often challenging due to the limited film thickness. In this work, we introduce an X-ray diffraction-based method for collecting and constructing quantitative pole figures with an area detector for thin films with isotropic crystallographic orientation in the substrate plane (classically referred to as fiber texture). The technique is rapid and ideal for thin films that are sensitive to beam damage, diffract weakly or are otherwise limited by their thin film form to certain diffraction geometries.

A pole figure is a plot of the orientation distribution of a particular set of crystallographic lattice planes, providing a useful illustration of a material's texture. Traditional pole figures of bulk samples can be collected in either reflection or transmission mode. Pole figures collected in a reflection mode utilize a symmetric geometry introduced by Schultz [10-12]. In this technique, diffraction intensities are collected using a point detector as the sample is rotated along two axes. Accurate collection of intensity in the Schultz geometry is generally limited to within 85° of the surface normal, due to distortions that arise at the substrate edge. Transmission techniques [13-15] are feasible, but require

either intensity corrections or special sample shapes, and in general cannot be used for thin films for which the substrate absorbs the X-rays. Whether dealing with reflection or transmission geometries, collection with a point detector across such a large slice of the reciprocal lattice space is time-intensive, especially for thin films. The use of an area detector facilitates more rapid collection of intensity across a large section of reciprocal space, greatly decreasing total acquisition time. Area detectors are commonly used with transmission-based geometries, allowing for the simultaneous collection of Debye-Scherrer rings from multiple Bragg reflections[16, 17]. The use of flat area detectors in combination with reflection geometries for thin films results in some image distortions, making quantitative analysis difficult. Many research groups have reported useful, but mostly only qualitative, texture data of delicate thin films collected using grazing incidence synchrotron radiation with an area detector [5, 8, 18-24].

In the work presented here, we perform the diffraction experiments with a synchrotron radiation light source. The high photon flux of synchrotron radiation allows for efficient diffraction measurements of materials whose low crystal symmetry, small scattering cross section, or high beam sensitivity limits the characterization that is possible with an in house, lab-based source due to low signal to noise ratios[25]. Even for samples for which the aforementioned limitations do not apply, the use of high flux synchrotron radiation greatly reduces collection time required, and together with the use of an area detector allows for rapid pole figure collection (minutes rather than hours)[26, 27]. This is becoming a widespread method to collect texture data, and some software has been developed to calculate pole figures from Debye-Scherrer rings collected in transmission[17].

Few pole figures of thin solution-processed films have been published in the literature. These films often require the support of a rigid substrate and thus cannot be used for transmission-based diffraction geometries. The weak diffraction often associated with thin solution-cast films further contribute to the difficultly of pole figure data collection. The organic films used for published pole figures are typically limited to thick films on the order of microns[11, 28, 29] or otherwise highly diffracting materials[30], while functional organic semiconductors are applied as thin films less than ~100 nm, and often diffract weakly (especially semiconducting polymers). Thin films can have a crystal structure different from the bulk material as well as distinct texture. Published pole figures collected from solution-processed thin films of inorganic nanoparticles are also limited, due in large part to weak diffraction. Korgel and coworkers have collected small-angle scattering data of organized spherical particles[18-20], but similar small-angle work has not been performed on anisotropic nanoparticles. Breiby et al.[8] have published plots representing the orientation distribution of CdS nanorods in the plane of the substrate, taking advantage of the large beam footprint and interface sensitivity in wide-angle grazing incidence geometry. However, complete pole figures (biaxial in this case) were not reported and the orientation of nanorods out of the plane of the substrate was found using a model-dependent fit. The ideal pole figure collection technique for texture analysis must be both time efficient and capable of measuring the entire span of crystallite orientations: polar angles, c, from -90° to 90° (see Figure 3-1 for an illustration of diffraction geometry; we assume that the sample is approximately horizontal throughout this paper). The goal of this paper is to elucidate an

efficient methodology for the construction of such pole figures for fiber textured thin films. Although we chose to work with synchrotron radiation for time-efficiency, high signal-to-noise ratios, and sample lifetime considerations, this discussion could be applied to diffraction collected with an area detector and an in house, lab-based source, provided the polarization correction was modified according to the source used[31].

3.2 Obtaining a complete, accurate thin-film pole figure

We present a method of pole figure compilation for thin films with a fiber texture, where the crystallite orientation distribution is isotropic in the plane of the substrate, using synchrotron radiation and an area detector. This involves two separate measurements: one in grazing incidence geometry and one with the geometry locally satisfying the specular condition. Using a grazing incidence X-ray beam for diffraction greatly increases the signal to noise ratio by increasing the X-ray path length through the film, allowing for accurate intensity collection from weakly diffracting samples. The large beam footprint also serves to spread the beam power across the sample, resulting in less destructive data collection for radiation sensitive samples. However, raw intensity collected with a flat detector in grazing incidence geometry is distorted[32], and the detector image is not a direct map of reciprocal space. This makes it difficult to extract quantitative texture information. By appropriately combining intensity extracted from grazing incidence diffraction patterns with intensity extracted from local-specular diffraction patterns (where the proper choice of incidence angle prevents distortion near the Bragg reflection at hand), we obtain complete pole figures that represent the true intensity of a Bragg reflection across the entire span of polar angle c (-90º to 90º). This technique is simple, efficient and applicable to any thin film with a fiber texture. The only intensity corrections needed are for polarization and X-ray absorption (which is often negligible for thin films). This method can be immediately implemented to better understand the relationship between film processing and microstructure, enabling the development of solution-processed and inexpensive electronic and optoelectronic devices.

The assumptions made in this work are that (a) the sample has an isotropic crystallite orientation distribution in the plane of the substrate (i.e., has a fiber texture), or fiber texture is artificially created by rotating the substrate normal throughout the measurement, (b) the film thickness to be probed does not exceed ~100 nm (with a more exact thickness requirement depending up on the incidence angle as well as the material in question[33]) and (c) the detector sensitivity is not polarization-dependent. The geometry of the diffraction setup used in this work is detailed in Figure 3-1. Throughout our data analysis, we work with Bragg reflections corresponding to one chosen lattice spacing with Bragg angle $\mathbf{q_B}$ and reciprocal lattice vector $\mathbf{q}_B$. The Bragg reflections chosen for analysis have strong intensities, giving high signal-to-noise ratios. If possible, strong peaks that are far from the beamstop, and thus affected less by the air scattering background, are preferable. Software is used to extract the Bragg peak intensities as a function of polar angle χ, where $\chi = 0$

coincides with the $\mathbf{q}_z$ axis (see Appendix II). To achieve this, intensity is extracted along an annular region encompassing $\mathbf{q}_B$ and appropriate background subtractions are made.

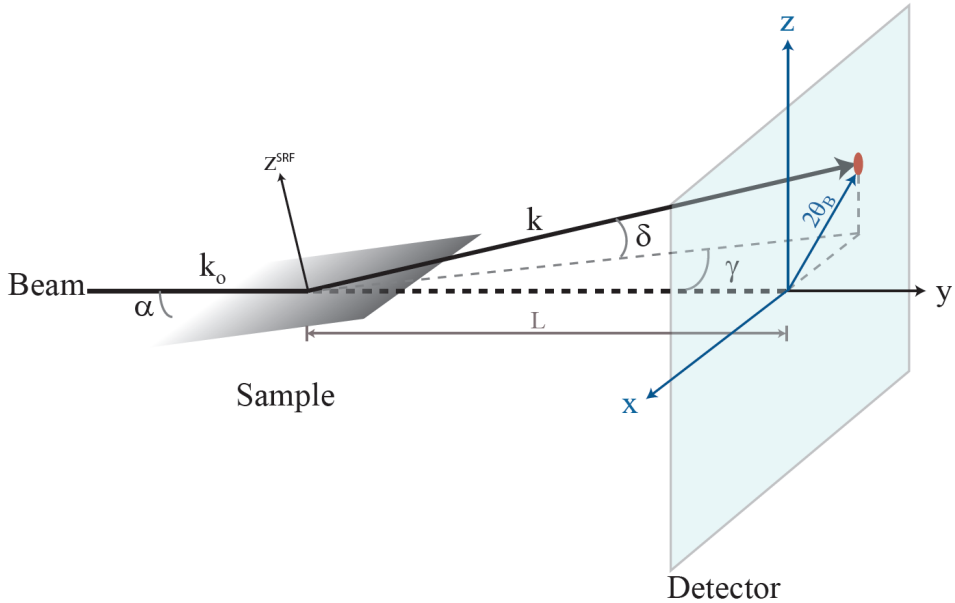

Figure 3-1. Schematic of diffraction measurement setup, including relevant geometry definitions. We assume that the sample is approximately horizontal throughout this paper. a is the angle of sample tilt (with respect to the incoming beam), z^{srf} is the sample surface normal of the sample, k_o is the incoming radiation wavevector, k is the outgoing (diffracted) radiation wavevector, L is the detector-sample distance, d is the vertical angle (with respect to the incoming beam) of the diffracted beam, g is the horizontal angle (with respect to the incoming beam) of the diffracted beam, x and z are the planar coordinates of the area detector, and $\mathbf{q_B}$ is the Bragg angle.

3.2.1 χ-Correction

Images collected with a grazing incidence geometry and a flat area detector are useful for qualitative analysis, but are not reciprocal space maps. To understand the distortions caused by the flat detector and grazing incidence geometry, it is helpful to imagine a sphere of crystallite orientations in reciprocal space. The radius of this orientation sphere is defined by the $\mathbf{q_B}$ of interest. The center of this sphere corresponds to $\mathbf{q}$=0 and is placed on the surface of the Ewald sphere at the head of the incoming **k** vector (See Fig 3-2). From this construction, we can see the intersection of these two spheres, corresponding to all observable diffraction in this geometry. This figure illustrates the importance of working with a sample that is either isotropic in-plane or rotated about z^{SRF} (sample surface normal) throughout the measurement (effectively creating in-plane isotropy). Crystallites with $\mathbf{q_B}$ near in-plane (Fig 3-2, vector ***a***) will intersect the Ewald sphere, while those with $\mathbf{q_B}$ close to perpendicular (Fig 3-2, vector ***b***) will not intersect the Ewald sphere and thus do not result in observed diffraction. The most vertical orientation that will result in observed diffraction (corresponding to the minimum detectable χ) has a polar angle of $\mathbf{q_B}$ (Fig 3-2, vector c). In other

words, rather than ranging [-90° to 0° to 90°], χ is constrained to a range of [-90° to -$\mathbf{q_B}$° and $\mathbf{q_B}$° to 90°] in the grazing incidence geometry. Thus, the intensity displayed along a vertical slice of the detector through the beamstop arises from crystallites with χ near $\mathbf{q_B}$. Interpretation of this vertical slice as the specular diffraction is thus incorrect, as has been pointed out previously[32, 34]. With this in mind, we collect intensity using an area detector in the grazing incidence geometry, assuring that the incidence angle used is above the critical angle for total external reflection to probe the entire film thickness. From the two dimensional pattern, we extract intensity as a function of χ along an arc with radius q_B. The arc used to extract intensity has a width Δq that is chosen to encompass the entire peak. Appropriate background subtractions are made to assure that collected intensity arises from diffraction from the crystallites and not extraneous scattering. This data set serves as the starting point for pole figure compilation, with the understanding that the signal near $\boldsymbol{\chi=0}$ is distorted and is not the true intensity.

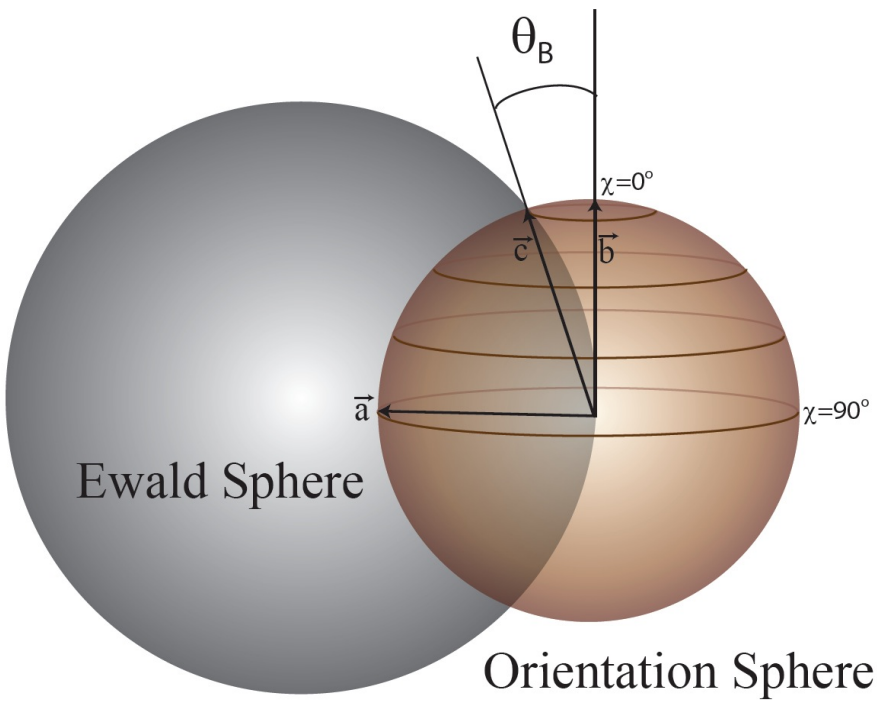

Figure 3-2. Intersection of Ewald sphere with crystallite orientation sphere, indicating possible diffraction events in grazing incidence geometry. **a** is the vector denoting an in-plane reciprocal lattice vector that results in pure horizontal scattering (χ =90°), **b** is the vector denoting an out-of-plane reciprocal lattice vector (χ =0°), which in the grazing-incidence geometry does not result in any observable scattering, and **c** is the vector denoting off-vertical reciprocal lattice vector which results in pure vertical scattering in the grazing incidence diffraction geometry. The local-specular condition is met when the substrate (and therefore orientation sphere) is tilted at $\mathbf{q_B}$.

To amend this distortion and move toward a complete pole figure, an additional data set is extracted from a second two-dimensional diffraction pattern, taken with the substrate tilted at an incident angle $\boldsymbol{\alpha} = \mathbf{q_B}$, such that the pole of the orientation sphere of the Bragg peak intersects the Ewald sphere. We refer to these curves as "local-specular," because of the exact satisfaction of the specular condition near the Bragg peak of interest. This type of scan has been referred to previously as a

'wide-angle rocking curve', since the substrate is rocked into the specular condition[21, 24]). We compile the full pole figure by appropriately merging the [intensity, χ] data sets extracted from the local-specular diffraction pattern and the grazing incidence diffraction pattern. To determine an appropriate merging angle for these two data sets, we plot intensity vs. χ for both diffraction patterns and adjust the arbitrary amplitude of one curve until both curves overlay (i.e. their local derivatives are identical) within the appropriate angular bounds. The relevant angular range for local-specular data is $\mathbf{0^o > \chi > 60^o}$, while the relevant angular range for grazing data is $\mathbf{q_B < \chi < 90^o}$. The $\mathbf{q_B}$ bound arises from the intersection of the Ewald and orientation sphere in grazing incidence geometry (see above), and the $\mathbf{60^o}$ bound arises from the physical blocking of the horizon diffraction by the substrate edge after tilting into Bragg condition in the local-specular geometry (See Appendix II for geometrical expression). The value between $\mathbf{q_B}$ and $\mathbf{60^o}$ at which the two sets of data are merged is operationally determined by the signal to noise ratio in the data.

A Lorentz correction [36-38] is required in X-ray geometries that involves either a rotating single crystal or a stationary powder sample. However, in the present case of morphology quantification (as opposed to structural characterization) the data are obtained from a single Bragg ring, which obviates the need for a Lorentz correction.

3.2.2 Polarization Correction

Synchrotron radiation is horizontally polarized, causing diffraction intensities that vary with angle[31]. To correct for this, we divide collected intensity by the polarization correction factor given in Eq. 1[36, 39]:

$$C_p = p_h\left(1-\cos^2\delta\cdot\sin^2\gamma\right)+\left(1-p_h\right)\cdot\left(1-\sin^2\delta\right) \qquad \text{Eqn. 1}$$

Here p_h is the fraction of radiation that is polarized in the horizontal direction (typically about 98% for a synchrotron source) and the angles **d** and **g** correspond to geometry shown in Figure 3-1.

3.2.3 Absorbance Correction

The path an X-ray follows through a film is longer at low exit angles than at high angles. If the absorbance of the film is high, this can affect the diffraction intensity data. Assuming a uniform sample absorbance, the expression for the correction is[40, 41]:

$$C_a = \frac{1 - e^{-\mu \cdot t\left(\frac{1}{\sin(\alpha)} + \frac{1}{\sin(\delta)}\right)}}{\mu \cdot \left(\frac{1}{\sin(\alpha)} + \frac{1}{\sin(\delta)}\right)} \quad , \qquad \text{Eqn. 2}$$

where m is the extinction coefficient (or inverse of the penetration depth at low angles) and *t* is the film thickness. Note that in many films, this correction is negligibly small. We can express the total intensity correction factor as the product of equations (1) and (2): $C_f = Cp * Ca$.

In summary, we collect two diffraction patterns for each sample: one at grazing incidence and one at an incidence angle satisfying the specular condition. Detector coordinates [x, z] are converted to angles **g** and **d**, $\mathbf{q_B}$ and χ. This image is used to obtain the intensity versus χ through an annular region at a selected Bragg ring, and any background intensity present is subtracted. The I(χ) data are corrected for polarization and absorption. The two I(χ) figures are scaled and merged at an angle greater than $\mathbf{q_B}$ but less than an upper bound angle, **60º**, defined by diffraction geometry; the intensity nearest the pole consists of data collected from the local specular diffraction pattern, while the intensity at larger angles of χ corresponds to the diffraction pattern taken at grazing incidence. On the completion of a satisfactory merge, we obtain our final, complete pole figure. The data analysis for this technique can be carried out quickly using WxDiff software [32].

3.3 Technique Application

Examples of materials for which this pole figure technique can be readily applied include thin films of nanostructured organic and inorganic semiconductors and nanostructured metallic thin films. For the semiconductors in particular, films are often fabricated via solution processing techniques such as printing, painting, or spray coating. It is useful to be able to quantify crystallite orientation distributions across these multi-parameter film deposition techniques. Diffraction data and intensity-corrected pole figures for three sample systems are plotted in Figure 3-3. These data were obtained on SSRL beam line 11-3 with a MAR345 image plate detector and an X-ray energy of 12.7 keV. For the grazing angle data, the vertical incident beam size was 0.05 mm, and the incidence angles were above the critical angles for the film examined (0.12º for polymer, 0.15º for both CdS and Au films). For the local specular data, the vertical incident beam size was 0.15 mm (full beam height). The q

and Δq values we chose for integration q≅.725 Å^{-1} and Δq=0.15 Å^{-1} (polymer); q≅1.865 Å^{-1} and Δq=0.07 Å^{-1} (CdS); q≅2.7 Å^{-1} and Δq=0.14 Å^{-1} (Au).

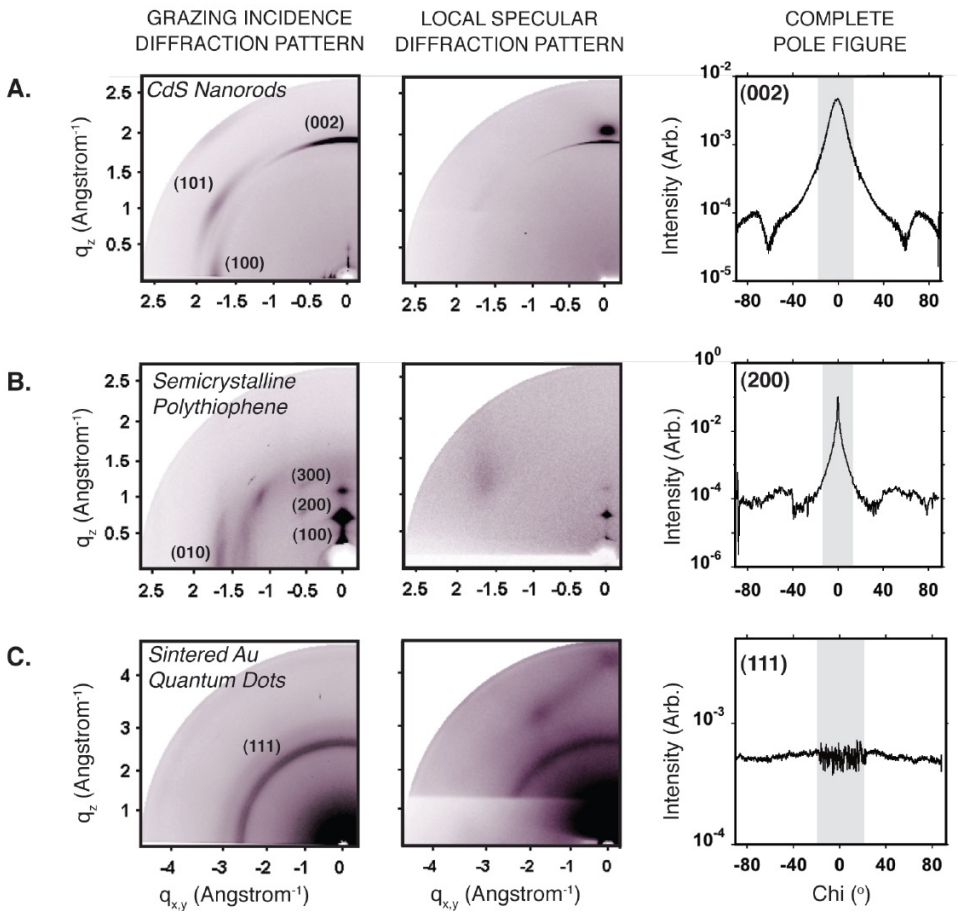

Figure 3-3. Example data for three different materials: A) CdS nanorods deposited by slow evaporation of nanorod solution, B) semicrystalline polymer poly[5,5'-bis(3-dodecyl-2-thienyl)-2,2'-bithiophene] (PQT-12) deposited by spin-casting, and C) sintered Au quantum dots deposited by spin-casting. The column on the left shows diffraction patterns collected in grazing incidence geometry. The middle column shows diffraction patterns taken with specular condition satisfied for the desired Bragg reflection, referred to as local-specular. The column on the right shows the complete pole figure, compiled by appropriately combining data from the grazing incidence diffraction patterns (unshaded regions) and the specular diffraction patterns (shaded region.) The specular diffraction patterns are necessary to complete the pole figures: the intensity highlighted in grey is not probed in the grazing incidence geometry and is instead collected in the local specular curves. Note that the intensity shown along q_{xy}= 0 in the grazing incidence images is distorted as described above (e.g., are not truly at q_{xy} = 0) but images are shown in this fashion for simplicity.

In a film composed of rod-shaped cadmium sulfide nanoparticles (Fig 3-3A), electron mobility normal to the film (and therefore device performance) can be improved by vertically orienting the nanorods, making the through-film direction appear as single-crystalline. Such a film of vertically aligned nanorods could offer high performance solar cells or LEDs at a low (solution-processed) cost. Our texture analysis method can be used to quantify the degree of vertical orientation in each film, thus allowing optimization of the nanorod deposition process[9]. Strong texture can be observed

from both the grazing incidence and local specular diffraction patterns of the film in Figure 3-3a. The (002) reflection appears with the strongest signal, and corresponds to the long axis of the wurtzite nanorod. The (101) and (100) reflections can also be observed, with angles appropriate for these respective crystal directions in reciprocal space. In principal, any of these reflections could be used to construct a pole figure, but with a lower signal to noise ratio for the (101) and (100). We construct a pole figure by correcting and merging these two diffraction patterns, using the (002) reflection because of its strong intensity. We see a strong preference for vertical (**c**=0) orientation of the (002) wurtzite crystal direction (long axis of nanorod), which indicates we have found appropriate processing conditions for our desired film of vertically aligned nanorods.

The electronic performance, namely the field-effect mobility, of thin films of polymer semiconductors has a similar dependence on film microstructure. Semicrystalline semiconducting polymers generally form films with crystallites on the order of 10-15 nm in diameter that are isotropically oriented in the plane of the substrate, with various degrees of ordering in the out of plane direction[3, 21, 23, 24]. The film texture depends strongly on the processing conditions. In the grazing incidence X-ray scattering pattern shown, we see three strong (h00) peaks, which arise from the backbone stacking of the polymers in the direction perpendicular to the substrate. The (010), arising from cofacial molecular stacking in the plane of the substrate, is visible along the horizon of the grazing incidence pattern. For this sample, we chose to compile a pole figure based on the (200) Bragg reflection (because of its strong intensity and distance from the direct beam). From the two diffraction patterns, we constructed a complete pole figure for the (200) Bragg reflection that confirms a strong tendency for out-of-plane texture. By quantifying the orientation distribution using (h00) pole figures, we can indirectly obtain information concerning the misorientation between neighboring crystallites. By comparing pole figures of multiple samples, we can more effectively study how microstructure (and in turn charge transport) changes with processing conditions. The complete pole figures shown in Figure 3-3b play an important role in film optimization.

In the case of the gold nanoparticle film, the goal was to understand the transformation of discrete particles into continuous metal films. Mechanically stable films can be formed from these particles at temperatures as low as 120 °C, with 70% the conductivity of bulk gold[43]. The texture of these metal films varies with sintering condition, though in the case of gold films, highly textured films are generally not seen. This is not the case for other metal systems such as silver where both (111) textured and untextured films can be produced depending on processing conditions. Because different crystal planes have different work functions, film texture will change the effective film work function. Also in the formation of microelectronic mechanical systems (MEMS), such as cantilevers, the mechanical properties of the films are drastically affected by the orientation of the metal films[44]. Both the diffraction pattern and the pole figure indicate almost no preference in orientation of the gold nanocrystals for this sintering condition, making this a useful control for probing film texture. Note that the data from the local specular condition is much noisier than the grazing data, due to the lower signal that results from a smaller sampling area.

The examples included in this discussion (the semiconducting nanoparticle film, the nanostructured semicrystalline semiconducting polymer and the sintered gold nanoparticle film) were chosen to illustrate the broad range of our method's utility. This method can be applied to any diffracting thin films with fiber texture. In the cases mentioned, complete pole figures have been a critical tool for the characterization of film structure, giving insight into the effect of various processing conditions.

3.4 Conclusion

We have demonstrated a fast and efficient data collection technique using synchrotron radiation and a flat area detector for the characterization of crystallographic orientation for functional thin films, and outlined a method for quantifying film texture by merging two, corrected data sets. In this work, we bring attention to inherent distortions in intensity collected using a flat image plate and discuss the correct factors and data merging techniques needed to use the data in a quantitative manner. The method presented here can serve as a valuable tool in the optimization of microstructure-dependent performance.

3.5 References

1. Robert L. Snyder, J. F., Hans L. Bunge *Defect and Microstructure Analysis by Diffraction*. Oxford University Press: Oxford, **1999**.
2. Jimison, L. H.; Toney, M. F.; Mcculloch, I.; Heeney, M.; Salleo, A., Charge-Transport Anisotropy Due to Grain Boundaries in Directionally Crystallized Thin Films of Regioregular Poly(3-hexylthiophene). *Adv. Mater.* **2009**.
3. Kline, R.; McGehee, M.; Kadnikova, E.; Liu, J.; Frechet, J.; Toney, M., Dependence of regioregular poly(3-hexylthiophene) film morphology and field-effect mobility on molecular weight. *Macromolecules* **2005,** 38, (8), 3312-3319.
4. Joseph Kline, R.; Mcgehee, M. D.; Toney, M. F., Highly oriented crystals at the buried interface in polythiophene thin-film transistors. *Nat Mater* **2006,** 5, (3), 222-228.
5. Breiby, D. W.; Sa, u., E. J., Quantification of preferential orientation in conjugated polymers using X-ray diffraction. *J. Polym. Sci. B Polym. Phys.* **2003,** 41, (20).
6. Resel, R.; Ottmar, M.; Hanack, M.; Keckes, J.; Leising, G., Preferred orientation of copper phthalocyanine thin films evaporated on amorphous substrates. *J Mater Res* **2000,** 15, (4), 934-939.
7. Kline, J. R.; Mcgehee, M. D.; Toney, M. F., Highly oriented crystals at the buried interface in polythiophene thin-film transistors. *Nat Mater* **2006,** 5, (3), 222-228.
8. Breiby, D.; Chin, P.; Andreasen, J., Biaxially Oriented CdSe Nanorods. *Langmuir* **2009,** 25, (18), 10970-10974.
9. Baker, J. L.; Widmer-Cooper, A.; Toney, M. F.; Geissler, P. L.; Alivisatos, A. P., Device-Scale Perpendicular Alignment of Colloidal Nanorods. *Nano Letters* **2010**.
10. Schulz, L., A direct method of determining preferred orientation of a flat reflection sample using a Geiger counter X-ray spectrometer. *J. Appl. Phys.* **1949,** 20, 1030.
11. Gilbert, M.; Ross, D.; Bowen, A., X-ray pole figures for oriented PVC. *Polymer(Guildford)* **1999,** 40, (5), 1233-1239.
12. You, L.; Yang, G.; Knorr, D.; McDonald, J.; Lu, T., Texture of vapor deposited parylene thin films. *Appl. Phys. Lett.* **1994,** 64, 2812.
13. Decker, B.; Asp, E.; Harker, D., Preferred Orientation Determination Using a Geiger Counter X-ray Diffraction Goniometer. *J. Appl. Phys.* **1948,** 19, (4), 388-392.
14. Norton, J., A Technique for Quantitative Determination of Texture of Sheet Metals. *J. Appl. Phys.* **1948,** 19, (12), 1176-1178.
15. Schwartz, M., … for Obtaining Complete Quantitative Pole Figures for Flat Sheets Using One Sample and …. *J. Appl. Phys.* **1955**.
16. Rodriguez-Navarro, A. B., Registering pole figures using an X-ray single-crystal diffractometer equipped with an area detector. *J Appl Crystallogr* **2007,** 40, (3), 631-634.
17. Garbe, U., New pole figure calculation software: 2DiffCalc. *J Appl Crystallogr* **2009,** 42, (4), 730-733.
18. Korgel, B. A.; Fullam, S.; Connolly, S.; Fitzmaurice, D., Assembly and Self-Organization of Silver Nanocrystal Superlattices: Ordered "Soft Spheres". *The Journal of Physical Chemistry B* **1998,** 102, (43), 8379-8388.
19. Connolly, S.; Fullam, S.; Korgel, B.; Fitzmaurice, D., Time-Resolved Small-Angle X-ray Scattering Studies of Nanocrystal Superlattice Self-Assembly. *Journal of the American Chemical Society* **1998,** 120, (12), 2969-2970.
20. Korgel, B. A.; Fitzmaurice, D., Small-angle x-ray-scattering study of silver-nanocrystal disorder-order phase transitions. *Physical Review B* **1999,** 59, (22), 14191.
21. Jimison, L. H.; Salleo, A.; Chabinyc, M. L.; Bernstein, D. P.; Toney, M. F., Correlating the microstructure of thin films of poly[5,5-bis(3-dodecyl-2-thienyl)-2,2-bithiophene] with charge transport: Effect of dielectric surface energy and thermal annealing. *Physical Review B* **2008,** 78, (12), -.
22. Belman, N.; Acharya, S.; Konovalov, O.; Vorobiev, A.; Israelachvili, J.; Efrima, S.; Golan, Y., Hierarchical Assembly of Ultranarrow Alkylamine-Coated ZnS Nanorods: A Synchrotron Surface X-Ray Diffraction Study. *Nano Lett* **2008,** 8, (11), 3858-3864.

23. Sirringhaus, H.; Brown, P. J.; Friend, R. H.; Nielsen, M. M.; Bechgaard, K.; Langeveld-Voss, B. M. W.; Spiering, A. J. H.; Janssen, R. A. J.; Meijer, E. W.; Herwig, P.; de Leeuw, D. M., Two-dimensional charge transport in self-organized, high-mobility conjugated polymers. *Nature* **1999,** 401, (6754), 685-688.
24. Chabinyc, M. L.; Toney, M. F.; Kline, R. J.; Mcculloch, I.; Heeney, M., X-ray scattering study of thin films of poly(2,5-bis(3-alkylthiophen-2-yl)thieno[3,2-b]thiophene). *J Am Chem Soc* **2007,** 129, (11), 3226-3237.
25. Wcislak, L.; Klein, H.; Bunge, H.; Garbe, U.; Tschentscher, T.; Schneider, J., Texture analysis with high-energy synchrotron radiation. *J Appl Crystallogr* **2002,** 35, 82-95.
26. Wenk, H.; Grigull, S., Synchrotron texture analysis with area detectors. *J Appl Crystallogr* **2003,** 36, 1040-1049.
27. Heidelbach, F.; Riekel, C.; Wenk, H., Quantitative texture analysis of small domains with synchrotron radiation X-rays. *J Appl Crystallogr* **1999,** 32, (5), 841-849.
28. Brasen, D.; Wang, T., Pole Figure Measurements of Drawn and Rolled PVF2 Films. *J. Appl. Phys.* **1981,** 52, (9), 5543-5546.
29. Pazur, R.; Prud'Homme, R., X-ray Pole Figure and Small Angle Scattering Measurements on Tubular Blown Low-Density …. *Macromolecules* **1996**.
30. Salzmann, I.; Resel, R., STEREOPOLE: software for the analysis of X-ray diffraction pole figures with IDL. *Journal of Applied Crystallography* **2004,** 37, (6), 1029-1033.
31. Als-Nielsen, J.; McMorrow, D., *Elements of modern X-ray physics*. Wiley: New York, 2001.
32. Mannsfeld, S. C. B.; Virkar, A.; Reese, C.; Toney, M. F.; Bao, Z., Precise Structure of Pentacene Monolayers on Amorphous Silicon Oxide and Relation to Charge Transport. *Adv. Mater.* **2009,** 21, (22), 2294-+.
33. *This is not a rigorous requirement, but merely a guide. If the film is significantly thicker than the X-ray penetration depth, then only the surface region is probed.*
34. Breiby, D. W.; Bunk, O.; Andreasen, J. W.; Lemke, H. T.; Nielsen, M. M., Simulating X-ray diffraction of textured films. *Journal of Applied Crystallography* **2008,** 41, (2), 262-271.
35. Snyder, R. L.; Fiala, J.; Bunge, H. L., *Defect and Microstructure Analysis by Diffraction*. Oxford University Press: Oxford, **1999**.
36. Smilgies, D., Geometry-independent intensity correction factors for grazing-incidence diffraction. *Rev Sci Instrum* **2002,** 73, (4), 1706-1710.
37. Specht, E.; Walker, F., A Method for the Accurate Determination of Crystal Truncation Rod Intensities by X-ray Diffraction. *J Appl Crystallogr* **1993,** 26, 166-171.
38. Evans-Luetterodt, K.; Tang, M., Angle Calculations for a 2+2 Surface X-ray Diffractometer. *J Appl Crystallogr* **1995,** 28, 318-326.
39. Schleputz, C. M.; Herger, R.; Willmott, P. R.; Patterson, B. D.; Bunk, O.; Bronnimann, C.; Henrich, B.; Hulsen, G.; Eikenberry, E. F., Improved data acquisition in grazing-incidence X-ray scattering experiments using a pixel detector. *Acta Crystallographica Section A* **2005,** 61, (4), 418-425.
40. Warren, B. E., *X-Ray Diffraction*. Dover Publications, Inc.: New York, **1990**.
41. Barmak, K.; Kim, J.; Lewis, L. H.; Coffey, K. R.; Toney, M. F.; Kellock, A. J.; Thiele, J. U., On the relationship of magnetocrystalline anisotropy and stoichiometry in epitaxial L1[sub 0] CoPt (001) and FePt (001) thin films. *Journal of Applied Physics* **2005,** 98, (3), 033904-10.
42. Baker, J. L.; Widmer-Cooper, A.; Toney, M. F.; Geissler, P. L.; Alivisatos, A. P., Device scale vertical alignment of colloidal nanorods. *Nano Letters* **2010**, 10 (1) 195-201.
43. Huang, D.; Liao, F.; Molesa, S.; Redinger, D.; Subramanian, V. J., Plastic-compatible low resistance printable gold nanoparticle conductors for flexible electronics. *J Electrochem Soc* **2003,** 150, (7), G412-G417.
44. Faurie, D.; Renault, P. O.; Le Bourhis, E.; Goudeau, P., Study of texture effect on elastic properties of Au thin films by X-ray diffraction and in situ tensile testing. *Acta Materialia* **2006,** 54, (17), 4503-4513.

The following was reproduced with permission from: Jessy Baker (Rivest), Sarah L Swisher, Lam-Kiu Fong, Haimei Zheng, and A. Paul Alivisatos, "Assembled Monolayer Nanorod Heterojunctions" ACS Nano **2011**, *5* (5), pp 3811– 3816.

Copyright 2011 American Chemical Society.

* * * * *

Acknowledgements. We gratefully acknowledge PK Jain, B Sadtler, J Urban, D Milliron, and E Rabani for helpful discussions and critical review of the manuscript. We thank KM Yu for RBS data and MVP Altoe & S Aloni for EFTEM data. SEM, EDS and EFTEM were performed at the Molecular Foundry, Lawrence Berkeley National Laboratory (LBNL), and were supported by the Office of Science, Office of Basic Energy Sciences, Scientific User Facilities Division, of the U.S. Department of Energy under Contract No. DE-AC02—05CH11231. HRTEM was performed at the National Center for Electron Microscopy at LBNL. Work summarized in Figure 4-2 was funded by the Helios Solar Energy Research Center, which is supported by the Director, Office of Science, Office of Basic Energy Sciences of the U.S. Department of Energy under Contract No. DE-AC02-05CH11231. Work summarized in Figures 4-3 and 4-4 was supported by Director, Office of Science, Office of Basic Energy Sciences, of the United States Department of Energy under contract DE-AC02-05CH11231 on the Inorganic/Organic Nanocomposites NSET Program, KC3104. JBR and SLS performed electrical measurements and were supported by National Science Foundation Graduate Student Fellowships. An Intel Fellowship supported the research on heterojunction formation (JBR).

Chapter 4

Assembled Monolayer Nanorod Heterojunctions

4.1 Introduction

A dense array of perpendicularly aligned but asymmetric semiconductor nanorods with a compositional change along the rod length is desirable for a variety of systems where charge separation across an interface is a first step: catalytic systems, sensors, light-emitting diodes, photovoltaics and optoelectronics. Building upon work by others,[1-4] we have recently shown that colloidal semiconductor nanorods of a single composition can be organized by controlled evaporation over a reasonable length scale for device characterization.[5] However, the next step in producing such films with broken symmetry poses a challenge. While colloidal nanorods can be made asymmetric in solution by exploiting the different reactivity of the facets of a low symmetry crystal during cation exchange,[6] it is still difficult to subsequently organize the asymmetric nanorods such that they will all point in the same direction. Evaporative assembly will not be selective; introduction of a chemically selective agent on the substrate may produce asymmetric alignment, but will also likely block the subsequent charge flow pathways. Here we demonstrate that it is possible to create the desired asymmetric film by first assembling the single composition nanorods in an array and then performing cation exchange on that film (Figure 4-1). The ion exchange can be controlled to a high degree, affording a powerful means of patterning the nanorod films for subsequent use.

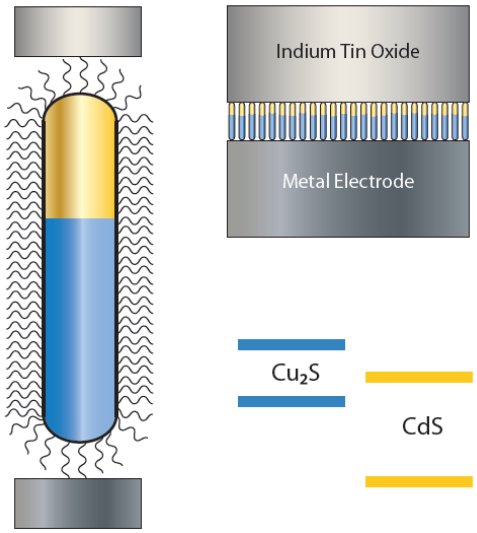

Figure 4-1. Schematic of parallel nanodiode or nano-photodiode arrays, and the bulk energy band alignment of our material system. Self-assembled colloidal CdS nanorods are partially converted (top ends only) to Cu_2S using our in-film cation exchange procedure.

4.2 Cation Exchange

Cation exchange can be used to chemically convert the top-layer of a crystalline film by replacing one cation for another while the anionic sub-lattice remains intact. However, the conversion is uneven in polycrystalline films, as the rate of exchange along different crystal axes can vary widely.[7,8] Columnar polycrystalline films yield improved uniformity, but contain grain boundaries down which cations can travel and plate out, causing shunting, shorting and cation-deficiency.[9,10] In single crystals, cation exchange results in high interfacial strain, causing dislocations that act as performance-degrading recombination sites. Cation exchange in vertically-oriented arrays of single-crystalline nanorods can relieve many of these challenges. The characteristic length over which dislocations are formed to relieve lattice mismatch are 5nm or greater in many materials systems.[9,11] If the nanorod diameter is less than 5nm, dislocations are avoided altogether and we reap only the benefits of ion exchange in a single crystal.

Recently, cation exchange has been applied to nanocrystals, in which this process has been shown to be uniquely shape-preserving and reversible, with reactions happening more rapidly than in the bulk

and yielding high quality material.[6,11-13] Here, we develop a new strategy to address the problem of *asymmetric*, single-nanocrystal cation exchange. We first fabricate a controlled structure using self-assembly and then use ion exchange to produce an array of oriented nanorod heterojunctions: In a vertically aligned, close-packed superlattice of nanorods on a substrate, ion access is limited to only the top end of individual nanorods, ensuring that exchange happens from only one end of the nanorod and that all nanodiodes are oriented in the same direction.

Here, cation exchange was performed *in film* by soaking the aligned nanorod film in a methanolic salt solution of the relevant cation in a dry, inert atmosphere. The molar amount of Cu^+ in the exchange solution was adjusted based on the number of required Cd^{2+} ion replacements to achieve exchange to a desired spatial depth into the aligned monolayer (Figure 4-2). This assumed that the reaction went to completion (all Cu^+ ions went into nanorods).

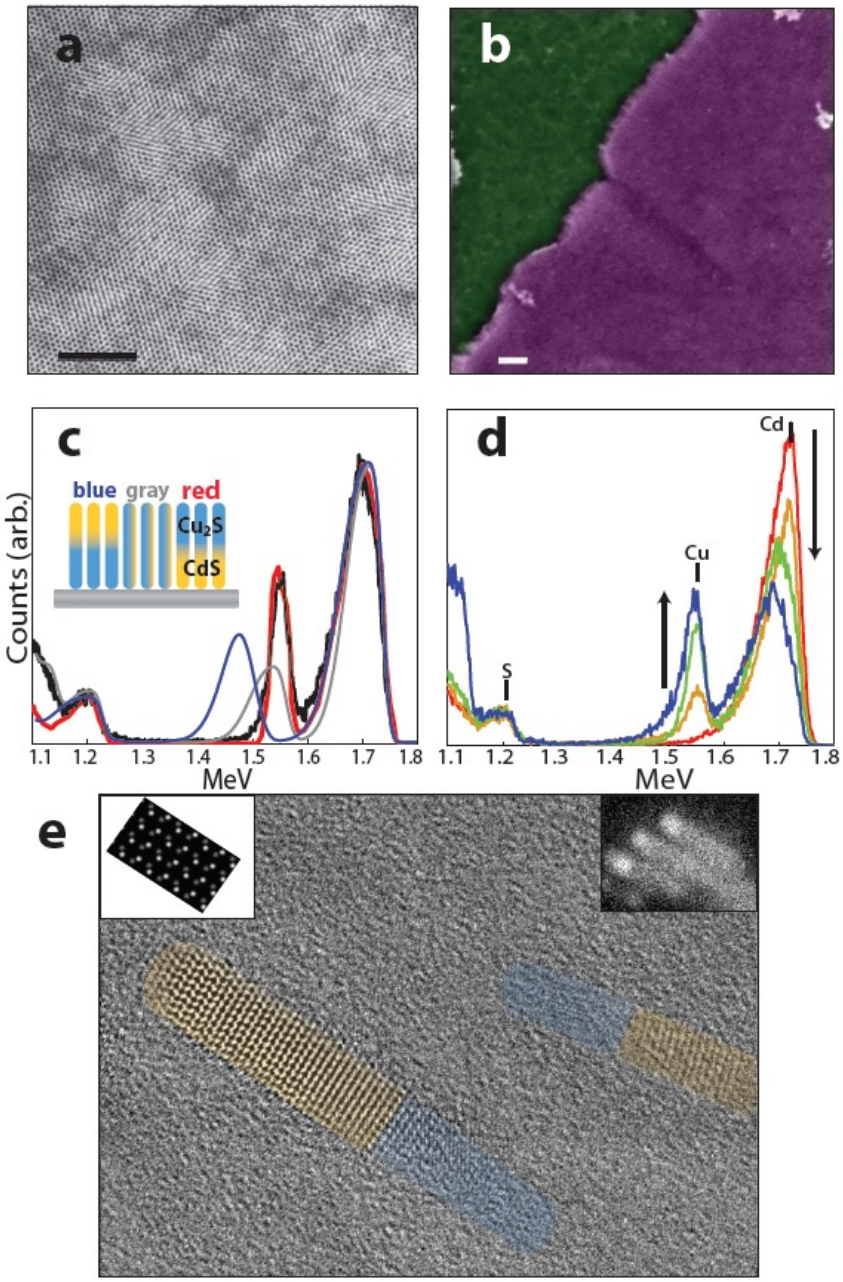

Figure 4-2. Self-assembled and cation-exchanged nanorod arrays. a) Transmission electron microscopy (TEM) image of aligned nanorod array. b) SEM false-color image of a film edge in a nanorod array, showing a monolayer of aligned rods (pink) on ITO (green). Scalebars are 100nm. c) Rutherford backscattering spectroscopy (RBS) demonstrates the selective copper ion exchange from the exposed ends of rods, resulting in asymmetry. Data (black) are fit with a simulated curve (grey) based on compositional depths (cartoon, inset). Simulations plotted show Cu_2S on top of CdS (red), Cu_2S and CdS evenly mixed within the film (gray), and Cu_2S underneath the CdS layer (blue). d) RBS shows that the extent of cation exchange can be controlled. The shift to lower energies of the Cd peak as the film is further Cu^+-exchanged indicates that the Cd is in the bottom layer of the film. Correspondingly, the lack of a shift in the Cu peak indicates that Cu is restricted to the top layer of the film. No exchange (red), 20% exchange to Cu (orange), 40% (green), and 60% (blue). e) High resolution TEM (HRTEM) image showing an example heterojunction after redispersion. Left inset shows the simulated CdS structure, providing evidence that the higher-contrast portion of the rod is CdS, while the lower-contrast portion of the rod is the lower-symmetry Cu_2S. Right inset shows energy filtered TEM image of redispersed nanorods, with the energy filter positioned at the Cu-M_1 edge.

4.3 Depth-profiling of heterojunction composition

The depth of the Cu exchange into the nanorod monolayer was characterized by Rutherford Backscattering Spectroscopy (RBS). Briefly, substrates were bombarded with He^{2+} ions. The kinetic energy of ions scattered elastically from the nanorod film were measured. Heights of Cd and Cu peaks in the RBS spectra allowed determination of the average film composition. Shifts in the peaks from their standard positions allowed approximate depth profiling of Cu- and Cd-rich sections. (Figure 4-2c,d) Spectra confirm that Cu^+ exchange occurs selectively from the top end of aligned nanorods.

Further evidence for one-sided exchange is provided by transmission electron microscopy (TEM). By redispersing a film of aligned & cation exchanged nanorods in chloroform and depositing the rods on an ultrathin carbon TEM grid, we were able to collect high-resolution TEM (HRTEM) and energy-filtered TEM (EFTEM) images to confirm asymmetric cation exchange. Studies of redispersed nanorods must be interpreted with care, because they inevitably will include rods that had been standing (one end exposed) as well as some rods that stood along scrack in the film (both ends exposed), as well as some rods from the bottom of a multilayer (neither end exposed). However, the presence of significant numbers of nanorods with contrast profiles like those shown in Figure 4-2e, is strongly suggestive of exchange that initiates on the exposed end of the rod film and propagates inward, with little or no exchange from the sides or buried ends of the rods. Extensive studies on HRTEM imaging of CdS-Cu_2S nanorods have shown that CdS is less sensitive to electron beam damage and appears to be higher in contrast compared with the counterpart of Cu_2S within a nanorod (Figure 4-2e). HRTEM images depict the Cd-S dumbbell characteristic of wurtzite Cadmium Sulfide (higher contrast, shaded yellow). Cu minor edge EFTEM images (Figure 4-2e right inset) were collected with a filter set at 120eV using a slitwidth of 5eV. The bright portions of the nanorods suggest a non-uniform composition and can be interpreted, following reference 6, as the Cu_2S phase.

This method for producing asymmetric nanoparticles allows us to control the spatial depth of the exchange to Cu_2S systematically. Nanorods in the film can also be exchanged to Ag_2S[12] (Appendix III) or by use of a sequential cation exchange method, they can be double-exchanged to rock salt PbS[14]. The method may be generalized to the exchange of chalcogenides with various cations (HgS, Ag_2S, SnS_2, CdS, CdSe, ZnS, ZnSe Cu_2S, Bi_2S_3, and Sb_2S_3).[11,13,15,16]

4.4 Electrical measurements of massively parallel nanorod junctions

A careful approach was required in order to make electrical contacts for studies of transport through these monolayer films. Evaporated metals have been employed successfully on relatively thick films or long nanowires,[17,18] but it has been shown that evaporation onto small nanorods can result in metal diffusion into the nanocrystal, altering electrical properties.[19] Further, evaporated metals may penetrate these thin films and produce shorts that can fluctuate in time, as in electrical measurements through monolayer molecular films.[20] In order to avoid shorting and damage to the nanocrystals, we made electrical contact using a room-temperature liquid metal (EGaIn) on a micromanipulator probe.[21] Approximate contact areas were measured with a side-view camera, and ranged from a few to hundreds of microns in diameter (contacting 10^6-10^9 nanorods). All measurements were taken inside an Argon glovebox at room temperature.

In order to demonstrate the high degree of compositional control provided by in-film cation exchange, we took electrical measurements of a monolayer film during a series of sequential cation exchanges on the same film (Figure 4-3). The chemical composition after each cation exchange step was confirmed using energy dispersive X-ray spectroscopy in a scanning electron microscope (Appendix III). The film region probed and the measurement conditions were kept approximately constant throughout. Measurements were repeatable in high-quality (well aligned monolayer) regions of the film over multiple cycles and multiple days, provided biases applied were no larger than +/-0.5 V.

The initial CdS nanorod array (contacted by EGaIn and indium tin oxide (ITO)) showed a linear current-voltage shape characteristic of Ohmic contact, as expected based on previous work.[22,23] After partial (to a depth of 25% into the monolayer) exchange to Cu_2S, rectification was measured, as expected from a type II heterojunction.[24] At only 25% exchange, it is likely that a fraction of the nanorods in the array are left unexchanged and provide a shunt path, limiting the rectification. Additionally, the high resistivity of CdS may increase series resistance in the diode, further reducing sharp rectification. From previous work,[6] it is expected that asymmetry in cation exchange from one nanorod end to another (001 to 001bar) does not exceed ~25%. Therefore, we expect that nanorods are exchanged with an average depth uniformity of +/- 4nm, in qualitative agreement with the RBS and TEM data.

Upon further soaking of the same film in a fresh and more concentrated cation solution to achieve ~70% cation exchange, the film showed greater rectification. This may be due to the formation of a Cu_2S top-layer extending over the entire film, preventing shunts. Greater rectification may also be related to the reduction in the percentage of high-resistivity (CdS) semiconductor.

Further exchange of this film with an excess molar amount of Cu^+ resulted in a film fully exchanged to Cu_2S, which showed an Ohmic electrical response. Because Cu_2S is highly doped in the bulk by copper vacancies,[25] it screens electric fields efficiently, leading to short depletion regions which

enable easy charge carrier tunneling through potential barriers.[26] Cu_2S is therefore expected to form Ohmic contact to most metals. In films of *unaligned* nanorods, no level of Cu^+ cation exchange produced rectification, most likely because the exchange results in a mixed-phase film with no common electric field to drive electrons toward the same electrode.

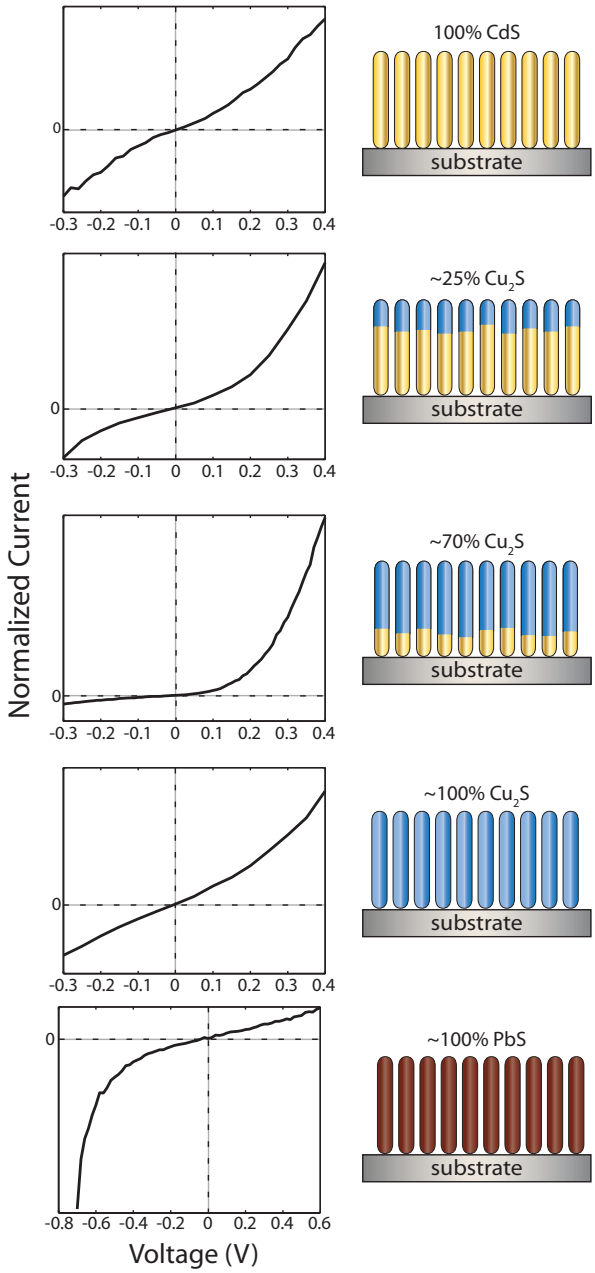

Figure 4-3. Sequential cation exchange. One film was used for a series of sequential cation exchanges: starting with CdS vertically aligned rods, Cu^+ was exchanged for Cd^{2+} to a 25% depth, then a 70% depth, then a 100% depth. Next, the resulting Cu_2S nanorods were exchanged fully to PbS. Between each cation exchange reaction, electrical measurements were taken and energy dispersive X-ray spectra were collected to verify the chemical composition. In the last stage (bottom frame), the liquid metal top-contact formed a Schottky junction with the PbS film, reversing the direction of rectification. All electrical measurements were performed in the dark.

Following full sequential exchange from Cd^{2+} to Cu^{+} and then to Pb^{2+} by soaking the Cu_2S film in a Pb^{2+} cation solution with a 10x molar excess of cations, the rectification direction reversed, as the resulting PbS rods formed Schottky junctions with the EGaIn probe. It is known that similarly-quantum confined PbS forms a Schottky junction with aluminum,[27] and the near-equality of aluminum and EGaIn work functions (~-4.3eV) suggest that the nature of the electrical contact may be the same. This series of experiments demonstrates precise control of composition and rectification of a nanorod film, using simple solution processing *in situ*.

The exchanged diodic films – both Cu_2S-CdS and PbS – showed a photoresponse when illuminated with AM1.5G solar flux (Figure 4-4). The photoresponse of the devices was stable (after exposure to air and subsequent storage in an Argon glovebox) for more than three months and was repeatable over this timeframe. The 30nm-long rods (and therefore 30nm-thick films) absorb approximately 8% of the solar spectrum above the Cu_2S and PbS confined bandgaps. The types of nanocrystals studied here are currently being examined in a variety of quantum confined semiconductor photovoltaics, where interparticle hopping plays a key role in the transport.[17,27,28] In the monolayer devices studied here, there is no interparticle hopping, allowing the influence of contacts and intraparticle recombination to be separately investigated from hopping phenomena. The photovoltages produced by these devices are rather low (0.13V for Cu_2S-CdS, 0.15V for PbS) compared with their theoretical values (~0.8V for Cu_2S-CdS,[29,30] and ~0.4V for PbS[14]) or their practical values (~0.45V for Cu_2S-CdS,[31] and ~0.3V for PbS[27]). The low photovoltage could be the result of a number of effects. In traditional photovoltaic devices, a low photovoltage is commonly associated with high recombination.[32] Given the high surface area of this system, it is reasonable to expect that there may be high rates of recombination that lower the photovoltage, and that these recombination sites could be passivated through ligand exchange or capping strategies. Alternatively, the low voltage could be a result of band alignments in the nanodiodes that differ from those observed in the bulk; quantum confinement and doping levels could cause large changes, as could pinning of the Fermi level. Other performance limitations may be set by the series resistance from the 1.8nm insulating ligands or by fundamental problems with ultra-thin heterojunctions, such as field quenching.[9,33] In future studies where the nanorod lengths and diameters and the ligand type and length are varied, it should be possible to learn a great deal about the intrinsic optical and electrical characteristics of the nanocrystals.

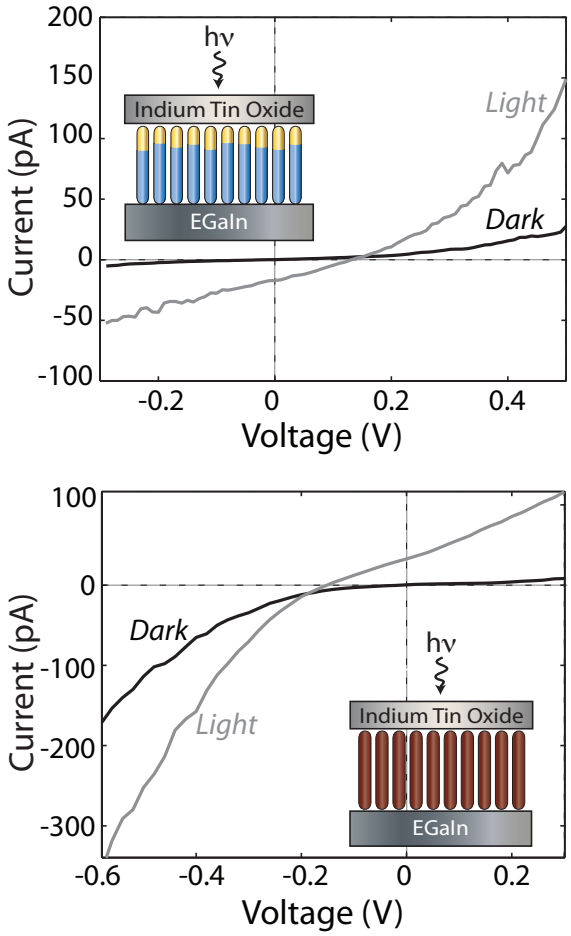

Figure 4-4. Current-voltage plot: Photovoltaic effect demonstrated in (top) a CdS-Cu_2S heterojunction and (bottom) a PbS Schottky nanodiode array.

We have presented a method for achieving a finely-tunable compositional and electrical architecture using colloidal nanorods. Perpendicular self-assembly and in-film cation exchange enable the precise formation of a single-crystal epitaxial heterojunction in each oriented nanorod, and can be used with a variety of chemical compositions. This advance may allow the production of inexpensive solution-processed photocatalysts, sensors, and optoelectronics. On the fundamental side, this architecture may enable better understanding of charge transport longitudinally through nanorods (without any inter-particle hops), and illuminate unique characteristics of devices at the few-nanometer scale.

4.5 References

1. Talapin, D. V.; Shevchenko, E. V.; Murray, C. B.; Kornowski, A.; Forster, S.; Weller, H. CdSe and CdSe/CdS Nanorod Solids *J Am Chem Soc* **2004**, 126, 12984-12988.
2. Ryan, K. M.; Mastroianni, A.; Stancil, K. A.; Liu, H. T.; Alivisatos, A. P. Electric-Field-Assisted Assembly of Perpendicularly Oriented Nanorod Superlattices *Nano Lett* **2006**, 6, 1479-1482.
3. Carbone, L.; Nobile, C.; De Giorgi, M.; Sala, F. D.; Morello, G.; Pompa, P.; Hytch, M.; Snoeck, E.; Fiore, A.; Franchini, I. R. *et al.* Synthesis and Micrometer-Scale Assembly of Colloidal CdSe/CdS Nanorods Prepared by a Seeded Growth Approach *Nano Lett* **2007**, 7, 2942-2950.
4. Gupta, S.; Zhang, Q. L.; Emrick, T.; Russell, T. P. "Self-Corralling" Nanorods Under an Applied Electric Field *Nano Lett* **2006**, 6, 2066-2069.
5. Baker, J. L.; Widmer-Cooper, A.; Toney, M. F.; Geissler, P. L.; Alivisatos, A. P. Device-Scale Perpendicular Alignment of Colloidal Nanorods *Nano Lett* **2010**, 10, 195-201.
6. Sadtler, B.; Demchenko, D. O.; Zheng, H.; Hughes, S. M.; Merkle, M. G.; Dahmen, U.; Wang, L. W.; Alivisatos, A. P. Selective Facet Reactivity During Cation Exchange in Cadmium Sulfide Nanorods *J Am Chem Soc* **2009**, 131, 5285-5293.
7. Sullivan, G. A. Diffusion and Solubility of Cu in Cds Single Crystals *Phys Rev* **1969**, 184, 796-&.
8. Macdonald, F.; Lide, D. R. CRC Handbook of Chemistry and Physics *Abstr Pap Am Chem S* **2003**, 225, U552-U552.
9. Boer, K. W. The Cds/Cu_2s Solar Cell *J Cryst Growth* **1982**, 59, 111-120.
10. Pfisterer, F. The Wet-Topotaxial Process of Junction Formation and Surface Treatments of Cu_2S-CdS Thin-Film Solar Cells *Thin Solid Films* **2003**, 431, 470-476.
11. Robinson, R. D.; Sadtler, B.; Demchenko, D. O.; Erdonmez, C. K.; Wang, L. W.; Alivisatos, A. P. Spontaneous Superlattice Formation in Nanorods Through Partial Cation Exchange *Science* **2007**, 317, 355-358.
12. Son, D. H.; Hughes, S. M.; Yin, Y. D.; Alivisatos, A. P. Cation Exchange Reactions in Ionic Nanocrystals *Science* **2004**, 306, 1009-1012.
13. Dloczik, L.; Koenenkamp, R. Nanostructured Metal Sulfide Surfaces by Ion Exchange Processes *J Solid State Electr* **2004**, 8, 142-146.
14. Luther, J. M.; Zheng, H. M.; Sadtler, B.; Alivisatos, A. P. Synthesis of PbS Nanorods and Other Ionic Nanocrystals of Complex Morphology by Sequential Cation Exchange Reactions *J Am Chem Soc* **2009**, 131, 16851-16857.
15. Dorn, A.; Allen, P. M.; Harris, D. K.; Bawendi, M. G. *In Situ* Electrical Monitoring of Cation Exchange in Nanowires *Nano Lett* **2010**, 10, 3948-3951.
16. Song, J. H.; Messer, B.; Wu, Y. Y.; Kind, H.; Yang, P. D. MMo_3Se_3 (M = Li^+, Na^+, Rb^+, Cs^+, NMe^{4+}) Nanowire Formation *via* Cation Exchange in Organic Solution *J Am Chem Soc* **2001**, 123, 9714-9715.
17. Luther, J. M.; Law, M.; Beard, M. C.; Song, Q.; Reese, M. O.; Ellingson, R. J.; Nozik, A. J. Schottky Solar Cells Based on Colloidal Nanocrystal Films *Nano Lett* **2008**, 8, 3488-3492.
18. Cui, Y.; Duan, X. F.; Hu, J. T.; Lieber, C. M. Doping and Electrical Transport in Silicon Nanowires *J Phys Chem B* **2000**, 104, 5213-5216.
19. Trudeau, P. E.; Sheldon, M.; Altoe, V.; Alivisatos, A. P. Electrical Contacts to Individual Colloidal Semiconductor Nanorods *Nano Lett* **2008**, 8, 1936-1939.
20. Bernede, J. C. Polarized Memory Switching in MIS Thin-Films *Thin Solid Films* **1981**, 81, 155-160.
21. Chiechi, R. C.; Weiss, E. A.; Dickey, M. D.; Whitesides, G. M. Eutectic Gallium-Indium (EGaIn): A Moldable Liquid Metal for Electrical Characterization of Self-Assembled Monolayers *Angew Chem Int Edit* **2008**, 47, 142-144.
22. Meng, X. L., Yongjuan; Yang, Baoping; Yi,Gewen; Jia, Junhong. Fabrication and Photoelectrochemical Characteristics of the Patterned CdS Microarrays on Indium Tin Oxide Substrates *Applied Materials and Interfaces* **2010**, DOI: 10.1021/am100548w.

23. Finlayson, M. F.; Wheeler, B. L.; Kakuta, N.; Park, K. H.; Bard, A. J.; Campion, A.; Fox, M. A.; Webber, S. E.; White, J. M. Determination of Flat-Band Position of Cds Crystals, Films, and Powders by Photocurrent and Impedance Techniques - Photoredox Reaction Mediated by Intragap States *J Phys Chem-Us* **1985**, 89, 5676-5681.
24. Reynolds, D. C.; Leies, G.; Antes, L. L.; Marburger, R. E. Photovoltaic Effect in Cadmium Sulfide *Phys Rev* **1954**, 96, 533-534.
25. Leon, M.; Terao, N.; Rueda, F. Phase-Transitions in Cuprous Sulfide Evaporated Thin-Films *J Mater Sci* **1984**, 19, 113-120.
26. Yu, A. Y. C. Electron Tunneling and Contact Resistance of Metal-Silicon Contact Barriers *Solid State Electron* **1970**, 13, 239.
27. Johnston, K. W.; Pattantyus-Abraham, A. G.; Clifford, J. P.; Myrskog, S. H.; Hoogland, S.; Shukla, H.; Klem, J. D.; Levina, L.; Sargent, E. H. Efficient Schottky Quantum Dot Photovoltaics: The Roles of Depletion, Drift, and Diffusion *Appl Phys Lett* **2008**, 92.
28. Huynh, W. U.; Dittmer, J. J.; Alivisatos, A. P. Hybrid Nanorod-Polymer Solar Cells *Science* **2002**, 295, 2425-2427.
29. Brandhorst, H. W. J. in *E-4722* 1-17 National Aeronautics and Space Administration, **1969**.
30. Rothwarf, A. The Cds-Cu_2s Solar Cell - Basic Operation and Anomalous Effects *Sol Cells* **1980**, 2, 115-140.
31. Stanley, A. G. Cadmium Sulfide Solar Cells *Applied Solid State Science: Advances in Materials and Device Research* **1975**, 5, 251.
32. Nelson, J. *The Physics of Solar Cells* (Imperial College Press, 2003).
33. Fahrenbruch, A.; Bube, R. H. Heat-Treatment Effects in Cu_2s-Cds Heterojunction Photovoltaic Cells *J Appl Phys* **1974**, 45, 1264-1275.

The following was reproduced with permission from the Journal of Physical Chemistry Letters, submitted for publication

Copyright 2011 American Chemical Society.

* * * * *

Acknowledgements. We gratefully acknowledge Haimei Zheng for helpful discussions and Bryce Sadtler for providing some samples and for review of the manuscript. This work was supported by the Physical Chemistry of Semiconductor Nanocrystals Program, KC3105, Director, Office of Science, Office of Basic Energy Sciences, of the United States Department of Energy under contract DE-AC02-05CH11231. Portions of this research were carried out at the Stanford Synchrotron Radiation Lightsource, a national user facility operated by Stanford University on behalf of the U.S. Department of Energy, Office of Basic Energy Sciences. JBR received funding from an Intel Fellowship. PJ acknowledges the fellowship of the Miller Institute at UCB.

Chapter 5

Size Dependence of a Temperature-Induced Solid-Solid Phase Transition in Copper(I) Sulfide

5.1 Introduction

Size dependent structural transformations and phase transitions in nanoscale materials play a key role in determining the phases that can be accessed and employed at the nanoscale, and yet there are still only a limited number of such transformations whose size and shape dependence has been mapped out. As a result, our understanding of the underlying factors that control metastabilty and stability in nanocrystals is still incomplete. With the advent of the capability to control the shapes of nanocrystals, as well as the ability to separately tune composition through means such as ion exchange, it is now possible to investigate size dependent structural transformations in a much wider range of systems. Here we investigate one such structural transformation in nanorods of copper sulfide.

Over the past few decades, copper sulfide has captured the attention of a broad scientific community with a rich $Cu_{2-x}S$ phase diagram and compositionally tunable properties. This semiconductor has found applications in photovoltaics,[1] switching[4,5] and sensing[6,7] (sometimes enabled or enhanced by chemical transformations[2,3] or doping[8,9]), in addition to copper ore processing.[10] The recent synthesis of copper(I) sulfide nanocrystals[2,11-14] may enable inexpensive solution processing for many of these applications, however, it is critical for implementation that the size-dependence of the material properties and crystallographic phase diagram be well understood.

Buffat and Borel described the size dependence of melting transitions in 1976[15] and their work has been followed by a variety of experiments probing size dependence in temperature- or pressure-induced solid-solid and solid-liquid phase transitions.[16-19] This body of work has described situations

where thermodynamic factors dominate over kinetics, and in the simplest case, the size dependence arises from a competition between surface energy and internal energy of each crystallographic phase. As the surface area to volume ratio increases, phases with lower surface energy become more favorable:

$$T_b - T_m = \frac{2T_m}{\Delta H^o \rho_1 R}\left[\gamma_1 - \gamma_2 \left(\frac{\rho_1}{\rho_2}\right)^{2/3}\right], \text{[17]} \qquad \text{Eqn 5-1}$$

$$P_b - P_m = \frac{2}{R}(\gamma_1 - \gamma_2), \text{[20]} \qquad \text{Eqn 5-2}$$

where T_b (P_b) is the bulk transition temperature (pressure), T_m (P_m) is the size-modified phase transition temperature (pressure), ΔH^o is the enthalpy change for the phase transition, R is the particle radius, r is density, and g is the surface tension of each phase (1 or 2).

Depending on the nature of the phase transition, a reduction in nanoparticle size may either increase or decrease the temperature or pressure at which the transition occurs. In the case of a solid-liquid transition, the surface energy almost uniformly decreases, so a melting point depression is typically observed with reduced particle size (exceptions arise in cases of melting of inclusions of one solid phase encapsulated inside another solid). Solid-solid phase transitions have different trends: they can show either higher or lower transition temperature or pressure with decreasing particle size. While there have been many reports of pressure-induced solid-solid phase transitions, temperature-induced first-order solid-solid transitions have been difficult to reliably observe due to inadvertent particle reorganization, sublimation, or sintering, which can change the size dispersion.

5.2 The low- to high- chalcocite transition in copper(I) sulfide

Stoichiometric or nearly stoichiometric Cu_2S exhibits the monoclinic low-chalcocite phase at room temperature, and shows a bulk transition to a higher symmetry hexagonal high-chalcocite at 376.65 K,[21] a temperature low enough to avoid sintering. Low chalcocite is a p-type semiconductor self-doped by copper vacancies, and has relatively high carrier mobility.[22,23] In the low chalcocite form, the sulfur sublattice is nearly close-packed hexagonal, while the copper ions are organized in a complex fashion, forming a 144-atom unit cell, $Cu_{96}S_{48}$.[24] This arrangement of cations leads to an indirect bandgap[25] of ~1.2eV. As low chalcocite (LC) converts topotactically to high chalcocite (HC), the sulfur atoms approximately maintain their positions while the copper ions adopt a partly statistical distribution on lattice sites, and the distinction between interstitial and lattice ions is lost.[26] This 'melting' of the copper sublattice gives rise to an increased almost liquid-like ionic mobility, but a decreased hole conductivity. It is interesting to note that disorder in the crystal structure in the HC phase leads to reduced mobility for holes and electrons in what amounts to the higher symmetry phase.[26] The transition has a subtle effect on the indirect bandgap (increased to 1.42eV), but leaves the direct transitions unaffected.[25] Despite the dependence of device-relevant optoelectronic

properties on the copper(I) sulfide phase, there is lack of robust experimental data on phase properties of copper(I) sulfide, as it is nontrivial both to identify its low-symmetry phases and to measure the exact stoichiometry, which varies between x=0 and x=0.2.

Phase transitions in copper(I) sulfide have been studied in extended solids[27-29] and, more recently, in nanoparticles.[30,31] A recent study[32] illuminated the dynamics of the LC-HC phase transition in nanorods, enabling the visualization of fluctuations between these two phases during the nucleation and growth of HC from the LC phase. This study was performed without intentional heating, yet was able to access the HC phase likely due to beam heating. There have been additional reports of HC nanoparticles existing at low temperatures,[11,13] which suggests a size dependence to copper(I) sulfide phase stability. However, until now, the nature of the relationship between particle size and transition temperature has not been systematically studied for the important phase transition from low to high chalcocite. Here, we show such a study using copper(I) sulfide nanorods to map out a size-dependent phase diagram for use in nanostructured devices employing nearly stoichiometric Cu_2S phases.

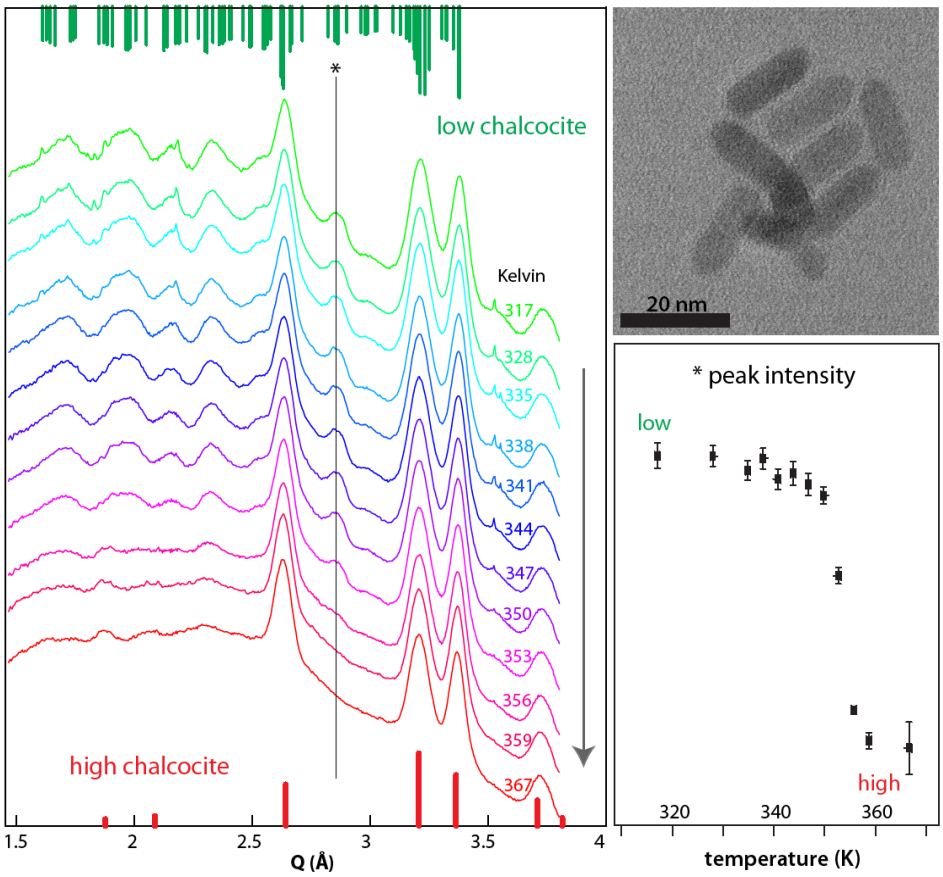

Figure 5-1. (left) Phase transition of Cu_2S from low chalcocite [Joint Committee on Powder Diffraction Standards (JCPDS) no. 00-033-0490] to high chalcocite [JCPDS no. 00-046-1195] with increasing temperature. The * peak near 2.84 Å is unique to low chalcocite, while other strong peaks are shared by the high chalcocite phase or are obscured by small crystallite size-induced broadening or background. The curves are offset for clarity. (top right) Transmission electron microscopy image of the nanorod sample from this data set allows size distribution measurements. (bottom right) A plot of the * peak intensity versus temperature shows a sharp transition from low to high chalcocite.

The stoichiometric low chalcocite phase of Cu_2S can be reliably obtained through a cation exchange of cadmium sulfide with Cu(I).[9,21,33] Monodisperse samples of CdS nanorods of controlled diameter and length were synthesized using Schlenck line techniques[34], and then converted to Cu_2S by addition of a methanolic solution of copper(I) salt to a solution of CdS nanorods in toluene.[6] The resulting copper(I) sulfide nanoparticles were drop-cast into a ~500nm thick film on a Si_3N_4 substrate. All steps were performed air-free to prevent oxidation of the nanoparticles, which is known to result in a variation in the stoichiometry and phase of Cu_2S.[9] X-ray diffraction of the copper(I) sulfide films was measured at the Stanford Synchrotron Radiation Lightsource (SSRL) at beamline 11-3 with an energy of 12.735 keV and a grazing incidence geometry. Samples were placed on a heating stage in a helium chamber and heated at 1 Kelvin per minute (to avoid temperature overshoot and facilitate near-equilibrium measurements). Collection time was 5 min and raw data were processed using WxDiff[35] to obtain intensity (I) *versus* Q plots.

From a plot of I(Q), the strongest LC peak was identified and monitored as a function of temperature. Due to the crystallographic relationship between low and high chalcocite, almost all diffraction peaks from HC are shared with LC, but the greater and more complex ordering in the LC phase is manifested as several additional peaks. One such peak near 2.84Å is unique to LC and is denoted by * in Figure 5-1, which shows the temperature dependent diffraction. High chalcocite data closely matched the JCPDS standard 00-046-1195, while low chalcocite closely matched 00-033-0490 both before heating and after cooling, indicating the Cu_2S stoichiometry was maintained during transition.

Error bars on the data presented result from sample size distribution, as measured by transmission electron microscopy (TEM) (x-axis) and limits in the accuracy of a) temperature measurement, b) Gaussian fitting and diffraction peak integration and c) the Boltzmann fitting (y-axis). Errors in absolute TEM size measurements are assumed to be negligible in comparison with other errors mentioned above. As the particle size decreases, the diffraction peaks are broadened, introducing more uncertainty. This accounts for the general trend of larger error bars on smaller particles.

The integrated peak intensity for the low chalcocite peak (2.84Å) was plotted as a function of temperature, resulting in a sigmoidal curve representing the transition from low chalcocite ($A_{LC}>0$) to high chalcocite ($A_{HC}\sim0$). Fitting these data with a Boltzmann function (Eqn 3) yielded a phase transition temperature, T_o.

$$y = \frac{A_{LC}-A_{HC}}{1+e^{(T-T_O)/\Delta T}} \quad , \qquad \text{Eqn 5-3}$$

where ΔT is the temperature range of the transition.

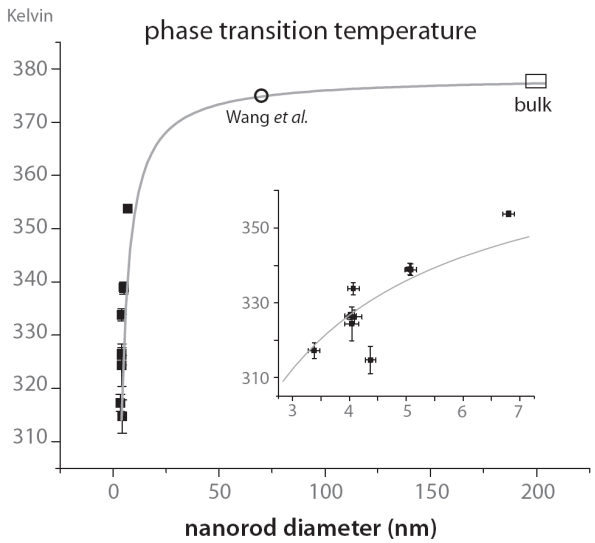

Figure 5-2. Phase transition temperature (Kelvin) as a function of nanorod diameter (nm). Data points collected in this study are black squares; data from bulk[21] and from Wang et al.[31] are noted. Inset shows a magnified plot of the data from the present study. The fitting curve (same in both plots) follows Equation 5-1 (Pearsons' s χ^2=1.18).

5.3 Size-Dependent Phase Relation

The average transition temperature (T_o) was plotted versus nanorod size (diameter) to obtain the size dependence (see Figure 2). A strong size dependence was observed, with nanorods transforming to high chalcocite at temperatures as low as 315 K, a depression of more than 60 K below the bulk transition temperature of 376.65 K. This trend indicates that HC may be thermodynamically favored at room temperature in nanocrystals smaller than 2.5nm diameter. The data were fitted to Equation 1 by assuming the same density (5.6 g/cc[24]) for the two phases, and an enthalpy change of 3849.3 J/mol.[36] This yields a change in average surface energy of 20 mN/m or roughly a change of 50% from the low chalcocite value of ~40 mN/m.[37,38] A typical range found for Dg/g is 15% to 50%.[19,39-41] Cu_2S may be on the high end of this range due to the unique nature of its LC-HC transition in which the Cu sublattice effectively melts, lending some solid-liquid character to this solid-solid transition. Further demonstrating the LC-HC order-disorder character is the high formation entropy of 10.238 J/K-mol (with 1.3 Cu(I) atoms distributed over 2 equivalent positions and 2.7 Cu(II) atoms distributed over 12 positions[42]).

The surface tensions obtained can be used in the Dupré equation to estimate the interfacial energy between the two phases (assuming no work of adhesion). Comparing interfacial energy with internal formation energy, we can calculate the critical nucleation radius (R^*) to be 0.885 nm, which is comparable to the smallest nuclei that were observed in the recent in situ TEM study of the this transition[32]:

$$R^* = {2\gamma_{LC-HC}}/{\Delta H_0} \ .^{43} \qquad \text{Eqn 5-4}$$

We also note that the hysteresis observed in this experiment is similar to that observed in extended solids.[27]

T_o was plotted as a function of nanorod length (keeping diameter constant at 4nm) and also as a function of nanorod diameter (keeping length constant at 40nm). We see that the nanorod transition temperature depends sensitively on the nanorod diameter *d*, whereas the nanorod length *l* has no significant effect on T_o (Figure 5-3). This is consistent with the fact that the independent variable in the size-dependent depression is the surface-area-to-volume ratio of the nanorods given by (4/d + 1/ℓ). In the range of dimensions in the present study, the length term (ℓ) is negligible.

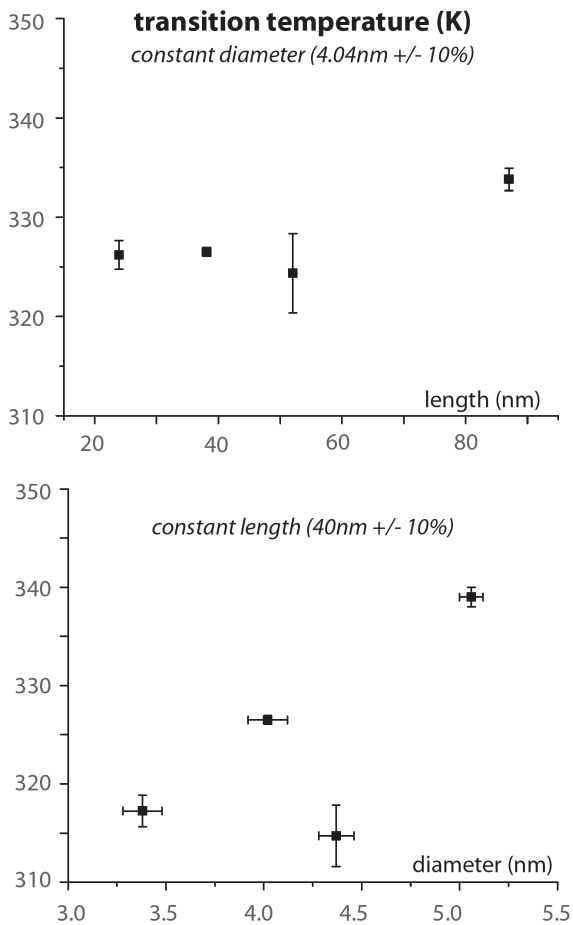

Figure 5-3. Phase transition temperatures (top) as a function of nanorod length with constant diameter of 4nm) and (bottom) as a function of nanorod diameter (with constant length of 40nm).

5.4 Implications for Cu_2S Applications

This work has some implications for the field of photovoltaics; copper sulfide comprised the original thin film solar cell in 1954.[33,44] In the photovoltaics community there has recently been significant interest in nanocrystalline Cu_2S as well as the related phases copper (indium gallium) (sulfide selenide) (CIGS) and copper zinc tin sulfide (CZTS)[45,46], which employ an ordered cation substitution for improved stability and optical tuning. The phase diagrams of these ternary and quaternary semiconductors are also complex, leaving open the possibility of relatively low-temperature phase transitions that may show a strong size-dependence near photovoltaic operating temperatures (typically 300 K to 330 K) or during crystal growth (500-800 K). In the case of Cu_2S for photovoltaic operation, our work indicates that it is crucial to maintain a particle size >6nm in diameter to avoid the stabilization of a deleterious phase (high chalcocite) at typical operating temperatures.

The stabilization of a high-temperature crystallographic phase at room temperature by use of nanocrystalline semiconductors may have favorable or unfavorable consequences, depending on the functional properties of interest. For example, the low to high ionic conductivity change during the LC-HC transition could find use in switching applications, which may be enabled by the narrow range of metastability observed due to the ~10 K hysteresis of this transition. Our results also provide context for several reported observations of high chalcocite phases in nanoparticles existing at low temperatures.[11,13] The uniquely low-temperature solid-solid transition observed for copper(I) sulfide suggests real-world applicability of this phase-change material, while making a broader call for characterization of additional materials whose phase diagrams enable transitions between functional crystal phases at room temperature.

5.5 References

1. Hadley, H. Materials aspects of Cu2S for CdS/Cu2S solar cells. *Journal of Crystal Growth* **1977**, *39*, 61–72.
2. Sakamoto, T.; Sunamura, H.; Kawaura, H.; Hasegawa, T.; Nakayama, T.; Aono, M. Nanometer-scale switches using copper sulfide. *Appl. Phys. Lett.* **2003**, *82*, 3032.
3. You, L. Copper Sulfide Solid-State Electrolytic Memory Devices, Case Western Reserve University, 2007.
4. Sagade, A. Copper sulphide (Cu_xS) as an ammonia gas sensor working at room temperature. *Sensors and Actuators B: Chemical* **2008**, *133*, 135–143.
5. Alaskar, M.; Ames, M.; Liu, C.; Connor, S.; Horne, R. SMART NANOSENSORS FOR IN-SITU TEMPERATURE MEASUREMENT IN FRACTURED GEOTHERMAL RESERVOIRS. *pangea.stanford.edu*.
6. Sadtler, B.; Demchenko, D. O.; Zheng, H.; Hughes, S. M.; Merkle, M. G.; Dahmen, U.; Wang, L.-W.; Alivisatos, A. P. Selective facet reactivity during cation exchange in cadmium sulfide nanorods. *J. Am. Chem. Soc.* **2009**, *131*, 5285–5293.
7. Luther, J. M.; Zheng, H.; Sadtler, B.; Alivisatos, A. P. Synthesis of PbS nanorods and other ionic nanocrystals of complex morphology by sequential cation exchange reactions. *J. Am. Chem. Soc.* **2009**, *131*, 16851–16857.
8. Zhao, Y.; Pan, H.; Lou, Y.; Qiu, X.; Zhu, J.; Burda, C. Plasmonic Cu(2-x)S nanocrystals: optical and structural properties of copper-deficient copper(I) sulfides. *J. Am. Chem. Soc.* **2009**, *131*, 4253–4261.
9. Luther, J. M.; Jain, P. K.; Ewers, T.; Alivisatos, A. P. Localized surface plasmon resonances arising from free carriers in doped quantum dots. *Nat Mater* **2011**, *10*, 361–366.
10. Dannenberg, R. O.; Gardner, P.C.; Crane, S. R.; Seidel, D. C. *Recovery of cobalt and copper from complex sulfide concentrates*; US Department of the Interior,Pittsburgh, PA, 1987.
11. Sigman, M. B.; Ghezelbash, A.; Hanrath, T.; Saunders, A. E.; Lee, F.; Korgel, B. A. Solventless Synthesis of Monodisperse Cu 2S Nanorods, Nanodisks, and Nanoplatelets. *J. Am. Chem. Soc.* **2003**, *125*, 16050–16057.
12. Wu, Y.; Wadia, C.; Ma, W.; Sadtler, B.; Alivisatos, A. P. Synthesis and photovoltaic application of copper(I) sulfide nanocrystals. *Nano Lett.* **2008**, *8*, 2551–2555.
13. Liu, Z.; Xu, D.; Liang, J.; Shen, J.; Zhang, S.; Qian, Y. Growth of Cu2S ultrathin nanowires in a binary surfactant solvent. *J Phys Chem B* **2005**, *109*, 10699–10704.
14. Rivest, J. B.; Swisher, S. L.; Fong, L.-K.; Zheng, H.; Alivisatos, A. P. Assembled monolayer nanorod heterojunctions. *ACS Nano* **2011**, *5*, 3811–3816.
15. Buffat, P.; Borel, J.-P. Size effect on the melting temperature of gold particles. *Phys. Rev. A* **1976**, *13*, 2287–2298.
16. Tolbert, S. H.; Alivisatos, A. P. Size Dependence of a First Order Solid-Solid Phase Transition: The Wurtzite to Rock Salt Transformation in CdSe Nanocrystals. *Science* **1994**, *265*, 373–376.
17. Goldstein, A. N.; Echer, C. M.; Alivisatos, A. P. Melting in semiconductor nanocrystals. *Science* **1992**, *256*, 1425–1427.
18. McHale, J. M. Surface Energies and Thermodynamic Phase Stability in Nanocrystalline Aluminas. *Science* **1997**, *277*, 788–791.
19. Banfield, J. Particle size effects on transformation kinetics and phase stability in nanocrystalline TiO2. *American Mineralogist* **1997**.
20. Tolbert, S. H.; Alivisatos, A. P. High-Pressure Structural Transformations in Semiconductor Nanocrystals. *Annu. Rev. Phys. Chem.* **1995**, *46*, 595–626.
21. Sands, T. D.; Washburn, J.; Gronsky, R. High Resolution Observations of Copper Vacancy Ordering in Chalcocite (Cu2S) and the Transformation to Djurleite (Cu1.97 to 1.94S). *Phys. Stat. Sol. (a)* **1982**, *72*, 551–559.
22. Hirahara, E. The Electrical Conductivity and Isothermal Hall Effect in Cuprous Sulfide, Semi-Conductor. *Journal of the Physical Society of Japan* **1951**.
23. Bougnot, J.; Guastavino, F.; Luquet, H.; Sodini, D. On the electrical properties of CuxS. *Phys. Stat. Sol. (a)* **1971**, *8*, K93–K96.
24. Buerger, M. J.; Buerger, N. W. LOW-CHALCOCITE AND HIGH-CHALCOCITE. *The American Minerologist*

1944, *29*, 55.
25. RASTOGI, A.; SALKALACHEN, S. Optical absorption behaviour of evaporated CuxS thin films. *Thin Solid Films* **1982**, *97*, 191–199.
26. Okamoto, K.; Kawai, S. Electrical Conduction and Phase Transition of Copper Sulfides. *Jpn. J. Appl. Phys.* **1973**, *12*, 1130–1138.
27. Leon, M.; Terao, N. On the phase transition of chalcocite Cu2S thin films. *Phys. Stat. Sol. (a)* **1981**.
28. Putnis, A. Electron diffraction study of phase transformations in copper sulfides. *American Mineralogist* **1977**.
29. Kazinets, M. M.; Ivanova, I. V.; Shafizade, R. B. Investigation of phase transformations in Cu1.8S-Cu2S thin films by kinematic electron diffraction. *GPHT* **1979**, *1*, 199–206.
30. Lotfipour, M.; Machani, T.; Rossi, D. P.; Plass, K. E. α-Chalcocite Nanoparticle Synthesis and Stability. *Chem. Mater.* **2011**.
31. Wang, S. Phase transitions in the Cu2S nanowires. *Materials Chemistry and Physics* **2002**, *75*, 32–38.
32. Zheng, H.; Rivest, J. B.; Miller, T. A.; Sadtler, B.; Lindenberg, A.; Toney, M. F.; Wang, L.-W.; Kisielowski, C.; Alivisatos, A. P. *Observation of Transient Structural Transformation Dynamics in a Cu2S Nanorod*; Science, 2011, 333 (6039) 206-209.
33. Carlson, A. *Research in semiconductor films*; 97494th ed. WADC Technical Report, 1956; Vol. Clevite Corporation.
34. Peng, Z. A.; Peng, X. Formation of High-Quality CdTe, CdSe, and CdS Nanocrystals Using CdO as Precursor. *J. Am. Chem. Soc.* **2001**, *123*, 183–184.
35. Mannsfeld, S.; Virkar, A.; Reese, C. Precise Structure of Pentacene Monolayers on Amorphous Silicon Oxide and Relation to Charge Transport - Mannsfeld - 2009 - Advanced Materials - Wiley Online Library. *Advanced* … **2009**.
36. Scientific Group Thermodata Europe SGTE, E. T. H. R. A. Thermodynamic Properties of Compounds, CuS to ErF3, pp. 175-200. **2001**, 1–26.
37. Ozcan, O. Classification of minerals according to their critical surface tension of wetting values. *International Journal of Mineral Processing* **1992**, *34*, 191–204.
38. Janczuk, B.; Wójcik, W.; ZDZIENNICKA, A. Determination of surface-free energy components of synthetic chalcocite from contact angle measurements. *Powder Technology* **1993**, *76*, 233–239.
39. Tolbert, S. H.; Alivisatos, A. P. Size Dependence of a First Order Solid-Solid Phase Transition: The Wurtzite to Rock Salt Transformation in CdSe Nanocrystals. *Science* **1994**, *265*, 373–376.
40. Buffat, P.; Borel, J.-P. Size effect on the melting temperature of gold particles. *Phys. Rev. A* **1976**, *13*, 2287–2298.
41. Hardy, S. C.; Coriell, S. R. Surface tension and interface kinetics of ice crystals freezing and melting in sodium chloride solutions. *Journal of Crystal Growth* **1973**, *20*, 292–300.
42. Gronvold, F.; Westrum, E. Thermodynamics of copper sulfides I. Heat capacity and thermodynamic properties of copper (I) sulfide, Cu2S, from 5 to 950 K* 1. *The Journal of Chemical Thermodynamics* **1987**.
43. Schmelzer, J.; Röpke, G. *Nucleation theory and applications*; 2005.
44. Reynolds, D.; Leies, G.; Antes, L.; Marburger, R. Photovoltaic Effect in Cadmium Sulfide. *Phys. Rev.* **1954**, *96*, 533–534.
45. Bhattacharya, R. N.; Contreras, M. A.; Teeter, G. 18.5% Copper Indium Gallium Diselenide (CIGS) Device Using Single-Layer, Chemical-Bath-Deposited ZnS(O,OH). *Jpn. J. Appl. Phys.* **2004**, *43*, L1475–L1476.
46. Katagiri, H.; Jimbo, K.; Maw, W. S.; Oishi, K.; Yamazaki, M.; Araki, H.; Takeuchi, A. Development of CZTS-based thin film solar cells. *Thin Solid Films* **2009**, *517*, 2455–2460.

Chapter 6

Conclusion

The work herein describes methods of achieving an unprecedented degree of morphological and compositional control of semiconductor thin films by piecing together the building blocks of self-assembly and chemical transformation (cation exchange or phase change). While the implications of this control are general to optical and electronic applications, this research was performed from the perspective of third-generation photovoltaics: **Vertical self-assembly** of nanorods was used to create a thin semiconducting film whose properties in the through-film direction equal those of a single crystal. With the development of a novel method for thin film **morphology quantification**, the assembly process was optimized and scaled. Square-centimeter areas of **96% vertical nanorod** alignment were achieved. A **cation exchange** technique was used to chemically convert aligned nanorods on-chip between Ohmic junctions, Schottky junctions, and **heterojunctions**. A **photovoltaic effect** was observed in illuminated rectifying cation exchanged junctions. The **crystallographic phase stability of Cu_2S** was strongly influenced by nanocrystal size; nanocrystals at least 5 nm in diameter should be used in photovoltaics to maintain favorable optoelectronic properties; the low- to high chalcocite phase transition is depressed from the bulk transition temperature by 60 degrees Celcius in nanocrystals less than 4 nm in diameter.

A wealth of future work exists on the morphological and compositional control of semiconducting thin films. Further development of the aligned nanorod architecture should focus on improving or displacing the native organic ligands on the nanocrystal surface, which may be acting as recombination sites and as large series resistors. Additionally, the elimination of cracks and multilayers in nanorod assemblies would enable the use of more robust electrical contacts and more scalable devices. This may involve using similar assembly methods at a liquid-liquid interface, or may require the development a completely distinct method that achieves perfect monolayered assembly. The morphology quantification method described in this dissertation may be applied to other material systems to quantify the relationship between processing conditions and thin film microstructure. Most immediately, the aligned, cation-exchanged nanorod architecture may be generalizable to a variety of chemical compositions, having already been demonstrated in Cu_2S-CdS heterojunctions and PbS Schottky devices. New chemistries may enable higher photovoltaic performance (through higher absorption or conductivity) or allow for the fabrication of different devices.

The application of this architecture is not limited to photovoltaics. The hierarchical structural control of these nanocrystalline films – from the monodisperse rod-shaped wurtzite crystallite

lattices to the perpendicular superlattice of rods to the compositionally organized film – demonstrates the control we have learned to wield in the production of nanocrystals. Whether in sensors, light-emitting diodes, transistors, memory, photocatalysis or photovoltaics, this architecture may one day be used to produce high-quality semiconducting devices at low cost.

APPENDIX I. Nanorod Assembly

SYNTHESIS OF NANOPARTICLES. Cadmium sulfide nanorods were synthesized according to the following procedure[1]: in a three-neck flask under an argon atmosphere, cadmium oxide (207mg, 1.6 mmol), *n*-octadecylphosphonic acid (1.08g, 3.2 mmol), and tri-*n*-octylphosphine oxide (2.75g, 7 mmol) were degassed, then heated to 300 °C to get a colorless solution. The flask was placed under vacuum at 120 °C for 1 hour, and then reheated to 335 °C. Trioctylphosphine (2g) was injected, followed by a rapid injection of sulfur dissolved in triocylphosphine (1.3g, molar ratio 1:1). The temperature was reduced to 310 °C and maintained for 45 minutes, at which point the heating mantle was removed and the sample was allowed to cool naturally. At 80 °C, anhydrous toluene was injected, and the entire solution was transferred (air-free) to a glass vial. The solution was centrifuged at 4,000 rpm for 30 minutes, and the precipitate was redispersed in toluene and octylamine, then immediately precipitated with isopropyl alcohol and centrifuged at 4000rpm for 30 minutes. This cleaning procedure was repeated until no white organic matter precipitated with the rods. The nanorods were further purified by dispersing in hexane, precipitating with acetone, and centrifuging at 4000 rpm. Size selective precipitation was employed to achieve good length monodispersity, and to remove any tetrapods. Note that careful cleaning is needed for both good monodispersity and nanorod length selection. The nanorods were typically 4nm in diameter and 35-100nm in length, with 10-12% polydispersity in both dimensions. They were stored air-free in hexane, and the final product was translucent. After cleaning, rods would not precipitate on their own – they remained soluble for at least one year.

ASSEMBLY. Before alignment, concentrations were measured with UV-vis absorption calibrated with inductively coupled plasma mass spectrometry. Rods were aligned in a closed cell with a controlled flow of dry nitrogen and a controlled temperature (Figure AI-2). Substrates were cleaned before film deposition either by dipping in toluene (Si_3N_4 membranes) or by sonication in toluene and isopropanol, followed by an oxygen plasma etch.

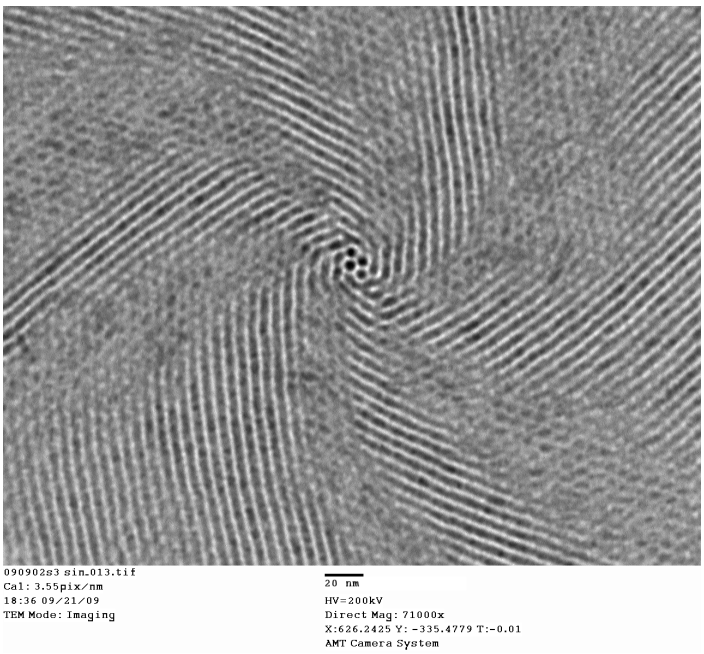

Figure AI-1. TEM of vertically aligned nanorods, showing how a small degree of nanorod tilt makes individual nanorods, and therefore their ordering, difficult to interpret.

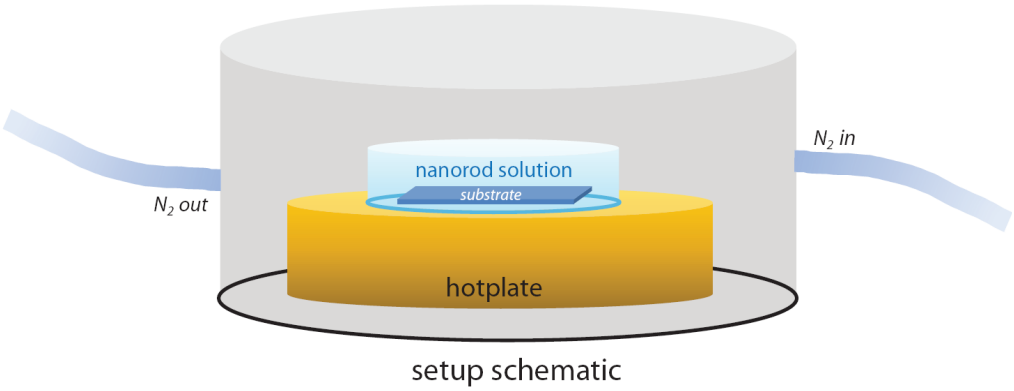

Figure AI-2. Schematic of controlled drying setup. The substrate was placed in the bottom of a short-walled container, which was filled with nanocrystal solution. This container was set on a hotplate, and placed inside a small Teflon evaporation chamber. A controlled flowrate of dry nitrogen through the small atmosphere of the chamber enabled control of solvent evaporation rate.

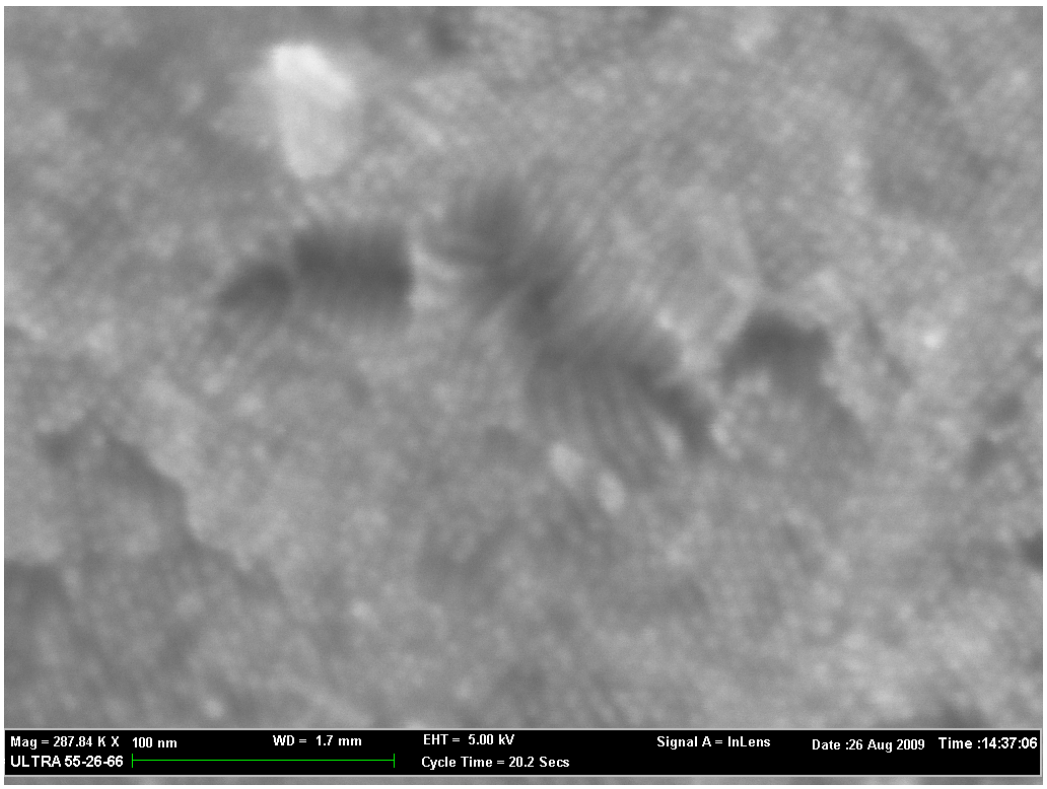

Figure AI-3. SEM image showing tilt of rods.

MORE DETAILS ON SURFACTANT CONCENTRATIONS, INITIAL ROD CONCENTRATIONS, AND EVAPORATION RATE

Other factors qualitatively found to influence alignment were evaporation rate, initial rod concentration, and concentration of excess surfactant. Alignment was aided by the presence of excess surfactant (native octadecylphosphonic acid) up to several hundred times in excess of the number of expected nanorod binding sites[2]. One reason for this could be that excess surfactant ensures thorough ligand coverage, even in the case of highly-labile surfactants. Dense ligand coverage is thought to prevent nanoparticle aggregation. Another possible explanation for this behavior is that the excess surfactant induces depletion-attraction interactions between the rods, which is predicted to reduce the concentration at which orientationally aligned phases start to form[3]. Beyond several hundred times excess surfactant, alignment was hampered.

The initial rod concentration had only a mild influence on the degree of alignment. Provided the initial rod concentration was at least high enough to produce a monolayer of vertically aligned rods on the bottom of the substrate container (see Fig AI-2), alignment proceeded. Higher concentrations aligned equally well.

The evaporation rate also had an effect on alignment. Rapid evaporation rates of several seconds resulted in no observable vertical alignment. Slowing evaporation rates down to 1mm/min meniscus speeds across the substrate resulted in well-aligned rods. Further slowing of evaporation

rate did not improve degree of alignment, but did improve film quality by reducing the stick-slip action of the meniscus[4] and thereby improving thickness uniformity.

ANALYSIS. TEM images were taken with a Tecnai G2 S-Twin electron microscope operating at 200kV . Statistics for the length polydispersity of the CdS nanorods were taken from at least 100 measurements of TEM images of each sample. Diffraction data were taken at the Stanford Synchrotron Radiation Lightsource on beamline 11-3 (wavelength 0.987 Angstroms) using a MAR345 image plate area detector at a distance of 400mm from the sample. Diffraction data were intensity-corrected for warping, polarization, x-ray absorption, and sample orientation. A grazing incidence (incident x-rays at 0.15degrees) data set (relevant at $|\omega|>=$ Bragg angle) was merged with a specular curve (incident x-rays at Bragg angle) (relevant only at low ω values).[5,6]

DETAILS OF VAN DER WAALS ENERGY CALCULATIONS. Rod-rod and rod-substrate dispersion energies, including the effect of ligands and solvent, were calculated using Hamaker-Lifshitz theory[7]. Dipole-dipole interactions between rods were calculated by integrating the dipole density over the appropriate volumes. Interaction energies obtained for 4 x 20nm CdS rods on a-Si_3N_4 in C_2Cl_4 and in vacuum are shown in Figure AI-4.

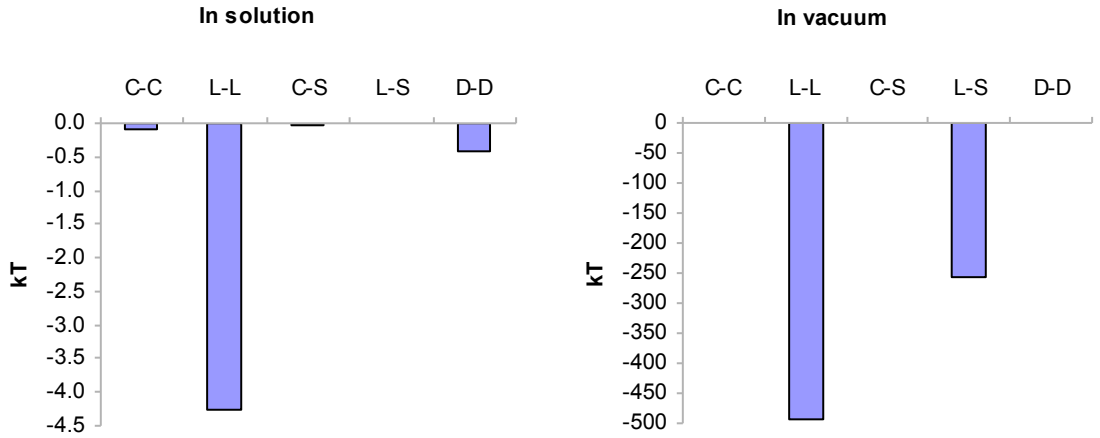

Figure AI-4. Typical rod-rod and rod-substrate interaction energies calculated in C_2Cl_4 (left) and in vacuum (right) at 300K. Nanocrystal-nanocrystal (C-C), ligand-ligand (L-L) and dipole-dipole (D-D) interactions are shown for rods oriented side-by-side with the dipoles anti-parallel to one another, while nanocrystal-substrate (C-S) and ligand-substrate (L-S) interactions are shown for rods oriented perpendicular to the substrate. Note the extremely small C-C and C-S energies and dominance of ligand terms when the rods are dry.

DISPERSION INTERACTIONS. Rod-rod interactions were calculated numerically by treating the crystalline core as a hexagonal prism of the appropriate diameter and length surrounded by a solid 1.5nm hydrocarbon shell using the expression

$$V^{vdW}(ij) = -\frac{A}{\pi^2}\int_{V_i}\int_{V_j}\frac{1}{r^6}d\bar{r}_i d\bar{r}_j$$

where A is the appropriate Hamaker constant for the interaction being considered. Previous work[8] suggests that the ligands on our CdS nanorods are almost entirely octadecylphosphonic acid, so the hydrocarbon shell was treated as n-octadecane. A contact distance of 0.3nm (the diameter of a methyl group) was used as this gave similar energies for the ligand-ligand interaction in air compared to when this was calculated using the surface tension of *n*-octadecane (28 mJ/m^2, Israelachvili[7] p. 315) and a ligand-ligand contact area equal to the area of one of the side crystal facets. The Hamaker constants used were: CdS (0.71 eV)[9]; *n*-octadecane (0.34 eV), estimated from the values for *n*-octane (0.28 eV) and *n*-hexadecane (0.33 eV)[7]; C_2Cl_4 (0.41 eV), estimated from the surface tension (31.7 dyn/cm)[10] using the approximate relationship[7] $\gamma = A/24\pi d_0^2$, where d_0 = 0.165nm. Hamaker constants for the ligand-solvent-ligand interaction and the nanocrystal-ligand-nanocrystal interaction were calculated from these using the combining rules in Israelachvili[7] (p. 200), which are expected to give reasonable estimates in nonpolar media.

Rod-substrate interactions were calculated analytically using the expressions for a cylinder (length L, radius R) interacting parallel or perpendicular to an infinite half-space (with the appropriate Hamaker constant A_s at a distance d from the surface)[11].

$$V_{\parallel}^{vdW}(d) = -\frac{A_s L R^2}{6(d(2R+d))^{3/2}},$$

$$V_{\perp}^{vdW}(d) = -\frac{A_s R^2}{12}\left(\frac{1}{d^2} - \frac{1}{(d+L)^2}\right)$$

The additional assumption was made that the dispersion interaction between the nanorod and the substrate can be split additively into two components: the ligand-solvent-substrate interaction, and the nanocrystal-ligand/solvent-substrate interaction. This assumption, while not entirely accurate, should still give the correct trend for energies on different substrates for a given solvent. The energies in Figure 2-3 were calculated for rods lying parallel to the substrate at a substrate-ligand distance of: (a) 0.3nm (the diameter of a methyl group) when the interaction was attractive at short range, or (b) the position of the minimum in the interaction potential when the interaction was repulsive at short range and attractive at longer range. Hamaker constants for a-Si_3N_4 (1.04 eV) and PEG (0.47 eV) were taken from Bergstrom[9] and Cao[12]. OTS (octadecyltrichlorosilane-functionalised Si_3N_4) was treated as *n*-octadecane. Hamaker constants for the ligand-solvent-substrate interaction and the nanocrystal-ligand/solvent-substrate interaction were calculated from these using the combining rules in Israelachvili[7] (p. 200), which are expected to give reasonable estimates in

nonpolar media. The ligand-substrate interaction in air (at contact) was estimated from the ligand-ligand interaction in air (also at contact) based on the differences in Hamaker constants for these two interactions, so their relative values should be approximately correct.

DIPOLE-DIPOLE INTERACTIONS. For the permanent dipole moment of CdS nanorods we use ρ_d = 1.1 D/nm^3, based on an estimate[13] that it is double that measured experimentally for CdSe nanorods[14]. Both CdS and CdSe have a wurzite lattice with intrinsic polarity along the rod axis due to a lack of inversion symmetry. We consider a uniform distribution of point dipoles inside the hexagonal prism of volume V, giving a total dipole moment $\rho_d V$. Dipole-dipole interactions for rods oriented antiparallel and end-to-end were calculated by integrating the dipole distributions over the volumes V_1 and V_2 of both nanorods using

$$V^D(ij) = -\rho_d^2 \int_{V_1}\int_{V_2} \frac{-3(\hat{\mu}_1 \cdot \hat{r})(\hat{\mu}_2 \cdot \hat{r}) + \hat{\mu}_1 \cdot \hat{\mu}_2}{4\pi\varepsilon_0 \varepsilon_1 r^3} d\vec{r}_i d\vec{r}_j$$

where $\hat{\mu}_1$ and $\hat{\mu}_2$ are unit vectors along the nanorod axes, $\vec{r}_i$ and $\vec{r}_j$ are the positions of the point dipoles within the nanorods, $\vec{r} = \vec{r}_i - \vec{r}_j$, and $\hat{r} = \vec{r}/r$, where $r = |\vec{r}|$. The effective dielectric constant ε_1 was taken to be 2.4 (in comparison, ε_1 for C_2Cl_4 is 2.5 and for dodecane is 2.0 [15]). Dipole coupling to the substrate was not considered. In previous work[11] this was found to be quite weak even for conducting substrates. As the substrates compared in Figure 2-3c are all non-conducting we expect the dipole coupling to the substrate to be even weaker in our systems.

INFLUENCE OF ENTROPIC LIGAND REPULSION AND NON-UNIFORM LIGAND DENSITY. While not explicitly considered in this work, it is well known that ligands attached to nanoparticles repel one another for both entropic and steric reasons when compressed[16]. This will act in opposition to attractive ligand-ligand and ligand-substrate dispersion interactions when the ligands are in contact with one another or a substrate. In these cases, the total ligand-ligand and ligand-substrate interaction energies will differ from the values presented here. The density of the ligand shell is also non-uniform, varying with distance from the surface of the nanorod. This may also modify the actual dispersion energies from the values calculated here.

We have begun more detailed analysis of the interaction between our CdS nanorods using molecular dynamics simulations with explicit ligands and solvent, carried out with methods and models similar to those of Vlugt et al.[16], in order to investigate these effects. Preliminary results from this analysis indicate that many of the assumptions behind the vdW energy calculations presented here are quite reasonable: our choice for the thickness of the ligand shell and the crystal-crystal separation at contact, as well as treating the ligands as a compact hydrocarbon shell with the same density as octadecane. We also note that these simulations show only a small degree of ligand interdigitation: mostly, the ligands at the point of rod-rod contact bend away from

one another. The results of this more detailed analysis lie beyond the scope of the present paper and will be presented elsewhere.

Based on this work to date, we expect the main conclusions from the continuum analysis presented here to remain valid, i.e. for the nanorods considered in the present study, the rod-substrate interaction can be made weak through an appropriate solvent-substrate combination (the trend in Figure 2-3c should remain the same), the crystal-crystal interaction will be insignificant in solution, and the ligand-ligand and ligand-substrate interactions will dominate in air.

EFFECT OF CHANGING ASPECT RATIO. Energetically, changing the aspect ratio (AR) of the rods is expected to have little effect on the relative stability of close-packed monolayers oriented perpendicular or parallel to the substrate, since the ratio of total energies per particle in the two structures remains close to constant within the range AR = 5-25. The two monolayers we considered are as described in Ref. 11, and similarly we sum over all the nearest-neighbor interaction terms to obtain the total interaction energy per particle in each of the two structures (in our case also considering the ligand interactions as described above). The energies obtained for rods with AR = 5 and 20 are listed in Table S1. As can be seen, the relative stability of the perpendicular and parallel structures changes little with aspect ratio. A rough estimate of the effect of entropic ligand repulsion can be made by reducing the magnitude of all ligand-ligand interactions by 50-100%. Such analysis yields results consistent with the above conclusion.

	In solution			**In vacuum**		
	Energy/particle (kT)			Energy/particle (kT)		
AR	Perpendicular	Parallel	Perp/Parr	Perpendicular	Parallel	Perp/Parr
5	-13.5	-6.7	2.0	-1736	-1505	1.2
20	-53.0	-20.5	2.6	-6168	-5577	1.1

Table AI-1. The total vdW interaction energy per nanorod for close-packed monolayers of CdS rods aligned perpendicular or parallel to an a-Si_3N_4 substrate in solution (C_2Cl_4) and in vacuum. The ratio of stabilization energies (Perp/Parr) is given for comparison between rods with different aspect ratios.

DIFFUSION CONSTANTS AND LONG-TIME DIFFUSION BEHAVIOUR OF ROD-SHAPED PARTICLES. Tirado et al.[17] have calculated analytical expressions for the short-time diffusion constants of cylindrical particles by considering local hydrodynamic effects:

$$D^{\perp} = \frac{D_0}{4\pi}(\ln p + 0.839 + 0.185/p + 0.233/p^2),$$

$$D^{\parallel} = \frac{D_0}{2\pi}(\ln p - 0.207 + 0.980/p - 0.133/p^2),$$

$$D^{r} = \frac{3D_0}{\pi L^2}(\ln p - 0.662 + 0.917/p - 0.050/p^2)$$

where $D_0 = k_B T/\eta_s L$, L is the total length, p is the aspect ratio, and η_s is the shear viscosity. These equations were found to be compatible with experimental results for DNA fragments with aspect ratios between 2 and 30[17]. We have used these expressions to discuss how the kinetics of nanorod

self-assembly is likely to vary with temperature and aspect ratio. In concentrated solutions, the rods will collide with one another resulting in slower long-time diffusion behaviour. The magnitude of this slow-down can be described by the ratio D_L^i / D^i of the long-time diffusion constants D_L^i to the short-time diffusion constants D^i, where $i = r$ (rotational) or t (translational). The long-time diffusion behaviour of hard spherocylinders undergoing Brownian dynamics according to the above short-time diffusion constants has been studied by Löwen[18]. At the density at which the rods form a nematic phase, $D_L^r / D^r \sim$ 0.1-0.2 and $D_L^t / D^t \sim$ 0.2-0.3 for aspect ratios of 6-20. Experimentally, 820 x 230nm Se rods were found to have $D_L^r / D^r \sim$ 0.3 and $D_L^t / D^t \sim$ 0.5 at a volume fraction of 18%[19]. Vicinal hydrodynamic effects, which were not considered by Löwen and may be important for the CdS nanorods studied in this papercould further reduce the long-time diffusion constants in our experimental system from the values obtained using the equations listed here.

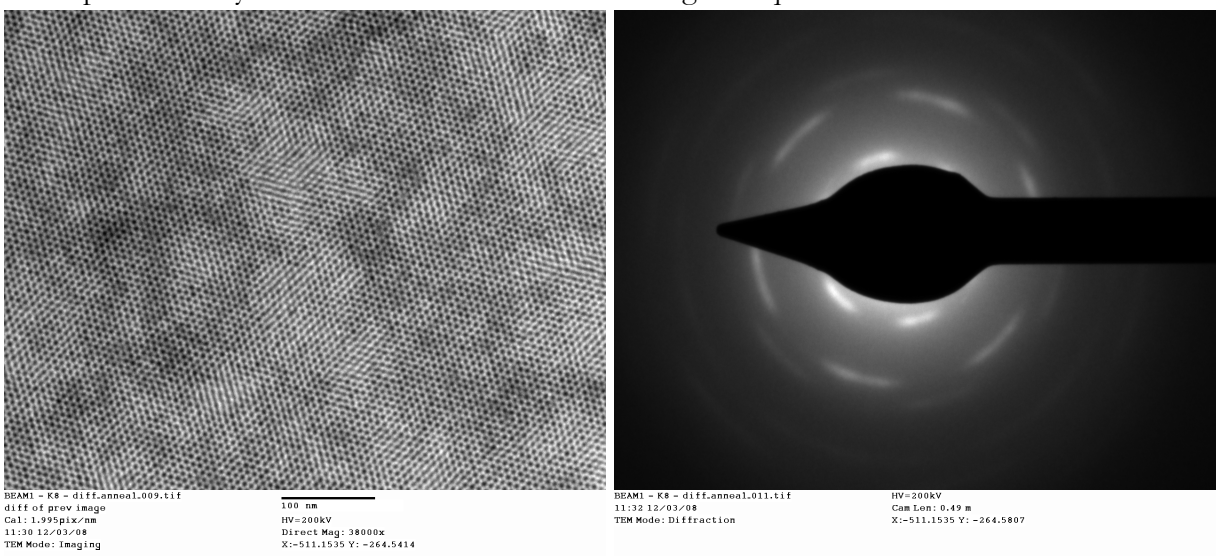

Figure AI-5. Vertically aligned array of nanorods and their corresponding selected-area wide-angle electron diffraction pattern. This pattern (which corresponds to the [100] spacing) shows that there is rotational order as well as orientational order (both the c- and the a-axes are aligned, forming a true supercrystal).

References

1. Peng, Z. A. & Peng, X. G. Formation of high-quality CdTe, CdSe, and CdS nanocrystals using CdO as precursor. *Journal of the American Chemical Society* **123**, 183-184 (2001).
2. Manna, L., Wang, Cingolani, R. & Alivisatos, A. P. First-Principles Modeling of Unpassivated and Surfactant-Passivated Bulk Facets of Wurtzite CdSe: A Model System for Studying the Anisotropic Growth of CdSe Nanocrystals. *The Journal of Physical Chemistry B* **109**, 6183-6192 (2005).
3. Bolhuis, P. G., Stroobants, A., Frenkel, D. & Lekkerkerker, H. N. W. Numerical study of the phase behavior of rodlike colloids with attractive interactions. *Journal of Chemical Physics* **107**, 1551-1564 (1997).
4. Adachi, E., Dimitrov, A. S. & Nagayama, K. Stripe Patterns Formed on a Glass-Surface During Droplet Evaporation. *Langmuir* **11**, 1057-1060 (1995).
5. Jimison, L. H., Salleo, A., Chabinyc, M. L., Bernstein, D. P. & Toney, M. F. Correlating the microstructure of thin films of poly[5,5-bis(3-dodecyl-2-thienyl)-2,2-bithiophene] with charge transport: Effect of dielectric surface energy and thermal annealing. *Physical Review B* **78**, - (2008).
6. Baker, J. L.; Jimison, L.H.; Mannsfeld, S.; Volkman, S.; Yin, S.; Subramanian, V.; Salleo, A.; Alivisatos, A.P.; Toney, M.F. Quantification of Thin Film Crystallographic Orientation Using X-Ray Diffraction with an Area Detector. *Langmuir*, **2010**, *26* (11), pp 9146–9151
7. Israelachvili, J. N. *Intermolecular and Surface Forces* (Academic Press, 1985).
8. Owen, J. S., Park, J., Trudeau, P.-E. & Alivisatos, A. P. Reaction Chemistry and Ligand Exchange at Cadmiumâ"Selenide Nanocrystal Surfaces. *Journal of the American Chemical Society* **130**, 12279-12281 (2008).
9. Bergström, L. Hamaker constants of inorganic materials. *Advances in Colloid and Interface Science* **70**, 125-169 (1997).
10. (http://ntp.niehs.nih.gov/index.cfm?objectid=E87D1CE3-BDB5-82F8-FF89E156508651F8).
11. Titov, A. V. & Kral, P. Modeling the Self-Assembly of Colloidal Nanorod Superlattices. *Nano Letters* **8**, 3605-3612 (2008).
12. Cao, G. *Nanostructures and nanomaterials* (Imperial College Press, London, 2004).
13. Nann, T. S., Jurgen. Origin of permanent electric dipole moments in wurtzite nanocrystals. *Chemical Physics Letters* **384**, 150-152 (2003).
14. Li, L.-s. & Alivisatos, A. P. Origin and Scaling of the Permanent Dipole Moment in CdSe Nanorods. *Physical Review Letters* **90**, 097402 (2003).
15. (http://www.clippercontrols.com/info/dielectric_constants.html).
16. Schapotschnikow, P., Pool, R. & Vlugt, T. J. H. Molecular Simulations of Interacting Nanocrystals. *Nano Letters* **8**, 2930-2934 (2008).
17. Tirado, M. M., Martinez, C. L. & Delatorre, J. G. Comparison of Theories for the Translational and Rotational Diffusion-Coefficients of Rod-Like Macromolecules - Application to Short DNA Fragments. *Journal of Chemical Physics* **81**, 2047-2052 (1984).
18. Lowen, H. Brownian dynamics of hard spherocylinders. *Phys. Rev. E* **50** (1994).
19. Maeda, H. & Maeda, Y. Direct Observation of Brownian Dynamics of Hard Colloidal Nanorods. *Nano Letters* **7**, 3329-3335 (2007).

APPENDIX II. Quantification of Thin Film Crystallographic Orientation

Here, we discuss how the pole figure for a given reciprocal lattice vector can be derived from the diffraction data recorded on a flat area X-ray detector. We consider a sample in which the crystallite orientation distribution is isotropic in the substrate surface plane. In order to extract the pole figure for the given reciprocal lattice vector $\mathbf{q}_B$ for such a sample, the X-ray scattering intensity I needs to be evaluated as a function of the angle χ between the scattering vector $\mathbf{q}$ and the pole vector $\mathbf{q}_{Pole}$. Refer to Figure 3-1 in main text of manuscript for geometrical definitions.

In an in-plane isotropic powder sample, the pole vector is parallel to the z-axis in the sample reference frame (z^{SRF}). The angle χ is then determined by: $\chi = \cos^{-1}(\mathbf{q}_z^{SRF} / ||\mathbf{q}||)$ where $\mathbf{q}_z^{SRF}$ refers to the z-component of $\mathbf{q}$ in the sample reference frame. In order to obtain the scattering intensity, I, as a function of χ, the components of the scattering vector in the sample reference frame must be determined.

However, the q-vector can directly be measured on the detector (detector reference frame). In general, $\mathbf{q}$ is given by:

$$\mathbf{q} = ||\mathbf{k}|| * (\mathbf{e}_k - \mathbf{e}_{k0}),$$

where $\mathbf{e}_{k0}$ and $\mathbf{e}_k$ are the unit vectors in the directions of the incident beam and the scattered beam, respectively. In the detector frame as depicted in Fig. 3-1, $\mathbf{e}_k$ is conveniently defined in spherical coordinates by the azimuthal angle g and the elevation angle d:

$$\mathbf{e}_{k0} = \begin{pmatrix} 0 \\ 1 \\ 0 \end{pmatrix}, \qquad \mathbf{e}_k = \begin{pmatrix} -\cos(\delta)\sin(\gamma) \\ \cos(\delta)\cos(\gamma) \\ \sin(\delta) \end{pmatrix}$$

With L, the sample-detector distance (see Fig. 3-1), d and g are easily calculated from the pixel position (x, z) on the detector:

$$\gamma = \tan^{-1}\left(\frac{-x}{L}\right), \quad \delta = \tan^{-1}\left(\frac{z}{\sqrt{L^2 + x^2}}\right)$$

The $\mathbf{q}$ vector in the detector frame, $\mathbf{q}^{DRF}$, is then given by:

$$\mathbf{q}^{DRF} = \mathbf{k}\begin{pmatrix} -\cos(\delta)\sin(\gamma) \\ \cos(\delta)\cos(\gamma)-1 \\ \sin(\delta) \end{pmatrix}$$

However, for the calculation of $I(\chi)$, we need the representation of **q** in the surface reference frame, $\mathbf{q}^{SRF}$. Relative to the detector frame, the sample frame is tilted backwards by the angle **a** as expressed by the rotation matrix $\mathbf{R}_a$:

$$\mathbf{R}_\alpha = \begin{pmatrix} 1 & 0 & 0 \\ 0 & \cos(\alpha) & -\sin(\alpha) \\ 0 & \sin(\alpha) & \cos(\alpha) \end{pmatrix}, \quad \mathbf{e}_i^{SRF} = \mathbf{R}_\alpha \mathbf{e}_i^{DRF}$$

Therefore, $\mathbf{q}^{SRF}$ can be calculated using the inverse of the matrix $\mathbf{R}_a$ by:

$$\mathbf{q}^{SRF} = \mathbf{R}_\alpha^{-1}\mathbf{q}^{DRF} = \mathbf{k}\begin{pmatrix} -\cos(\delta)\sin(\gamma) \\ \cos(\alpha)\big(\cos(\delta)\cos(\gamma)-1\big)+\sin(\alpha)\sin(\delta) \\ \cos(\alpha)\sin(\delta)+\sin(\alpha)\big(1-\cos(\delta)\cos(\gamma)\big) \end{pmatrix},$$

and thus, the z-component $\mathbf{q}_z^{SRF}$ in particular is given by:

$$\mathbf{q}_z^{SRF} = \mathbf{k}\big[\cos(\alpha)\sin(\delta)+\sin(\alpha)\big(1-\cos(\delta)\cos(\gamma)\big)\big].$$

The absolute value of the scattering vector, $|\mathbf{q}|$, is easily determined from the total scattering angle **2q**. In the non-grazing geometry, **2q** is easily determined from the position of a spot on the detector (x,z), as follows: With $\tan^2(2q) = (x^2+z^2)/L^2$ and Bragg's law, one finds:

$$|q| = \frac{4\pi}{\lambda}\sin\left(\frac{\tan^{-1}\left(\sqrt{x^2+z^2}\big/L\right)}{2}\right).$$

In grazing geometry, i.e., for incidence angles below the material's critical angle, a small correction has to be made for the $\mathbf{e}_{k0}$ unit vector because the scattering results from an evanescent wave field travelling in the sample surface:

$$e_{k0} = \begin{bmatrix} 0 \\ \cos(\alpha) \\ \sin(\alpha) \end{bmatrix}$$

The derivation of the $\mathbf{q}_z^{SRF}$ expressions derived here for the non-grazing case is completely analogous. However, the correction is very small (a is typically 0.1°) and can be safely neglected for most purposes and the equations above can be used unchanged.

With the expressions for $\mathbf{q}_z^{SRF}$ and $|\mathbf{q}|$, the pole figure can then be constructed from the pixels on the screen I(x, z) by calculating I(χ), with $\chi = \cos^{-1}(\mathbf{q}_z^{SRF} / ||\mathbf{q}||)$. In Figure AII-1, we plot a correction curve for the CdS experimental example discussed in the main text. Here $\mathbf{q}$=1.88 Å^{-1}, Θ_B=8.4°, the degree of radiation horizontal polarization is 98%, the film is 50% dense CdS and is 60nm thick. This plot indicates where uncorrected pole figure data is most distorted and most affected by the intensity corrections (e.g., different from unity).

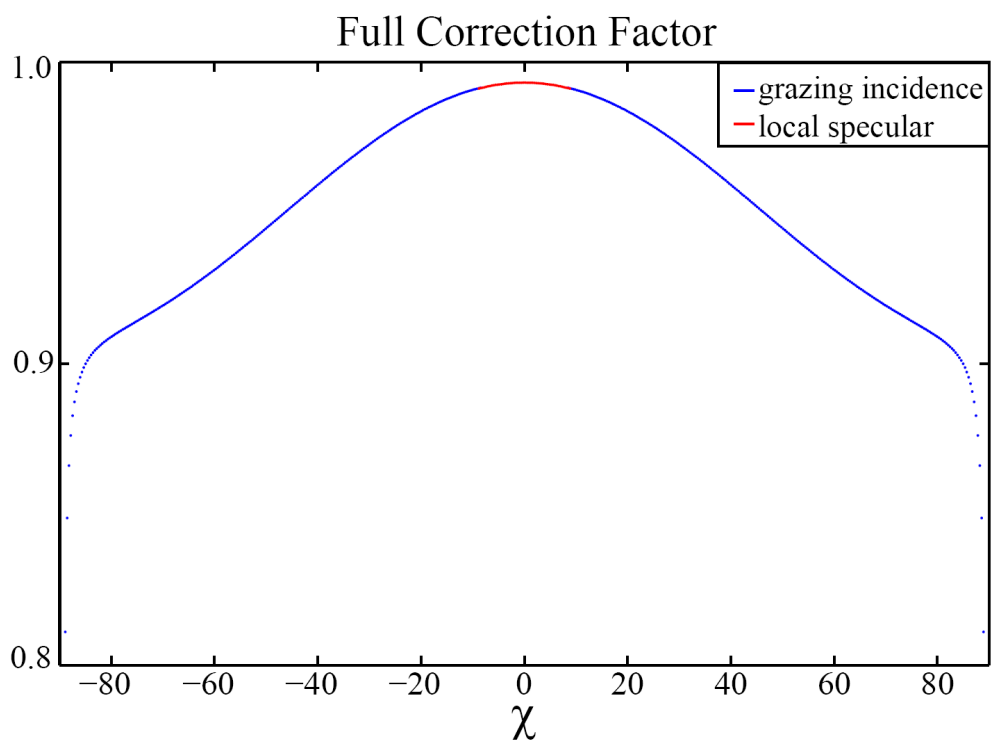

Figure AII-1. Plot of the final correction factor as a function of the angle χ. Raw intensity data should be divided by correction factor to yield true intensity.

To calculate the minimum angle for the local-specular curve:
Refer to Figure 3-1 in the main text. When the substrate is tilted by **a**, reflections that are below **a** in the detector frame of reference are physically blocked by the substrate. This sets a z constraint on the data from the area detector, as detailed below. The geometry of the system can be exploited to reveal the maximum allowed value of χ for the local-specular condition (where sample is tilted at $\mathbf{a}=\mathbf{q_B}$).

At the maximum (nearest to horizontal) angle of χ, the beam is grazing over the sample, meaning that the z-component of our outgoing (diffracted) k-vector in the surface reference frame is zero, $k_{z,o}^{SRF}=0$. Because the sample is tilted at the angle $\mathbf{a}=\mathbf{q_B}$, our incoming k-vector in the surface reference frame is $k_{z,i}^{SRF}=-k\sin(\mathbf{a})=-k\sin(\mathbf{q_B})$. Therefore, it follows that

$$
\begin{aligned}
q_z &= k_z^{SRF} - k_z = k \cdot \sin(\theta_B) = \frac{2\pi}{\lambda}\sin(\theta_B) \\
|q| &= \frac{4\pi}{\lambda}\sin(\theta_B) \\
\cos(\chi_{\max}) &= q_z / q = 1/2 \\
\chi_{\max} &= 60\,\mathrm{deg}
\end{aligned}
.
$$

Independent of sample geometry or composition, the maximum value (nearest to horizontal diffraction) one can obtain in the local-specular condition is χ=60 degrees.

APPENDIX III. Assembled Monolayer Nanorod Heterojunctions

METHODS

Sample preparation. Colloidal CdS nanorods were synthesized and self-assembled as reported elsewhere.[5] Briefly, nanorods were synthesized air-free with a CdO precursor in trioctylphosphine oxide and octadecylphosphonic acid. Nanorods were stored air-free, and colloidal concentrations were measured by UV-vis absorption calibrated with inductively coupled plasma mass spectrometry. With a controlled evaporation rate (<1 mm/min meniscus speed across a slightly tilted substrate), an elevated temperature (55 °C), an appropriate substrate (for example, silicon nitride), and a size-monodisperse sample, the nanorods oriented vertically.[5] The volume of nanorod solution needed for monolayer self-assembly was calculated by substrate area, assuming a 50% areal fill factor due to the long organic ligands on the nanorods. Substrates on which nanorods were to be aligned (Si_3N_4 for RBS measurements; 150nm 20Ω/square ITO on glass for electrical measurements) were cleaned by sequential sonication in water, toluene, isopropanol and acetone, followed by an oxygen plasma etch. This cleaning procedure was performed to reduce the friction between the solvent meniscus and substrate, in an effort to avoid any stick-slip behavior that would be detrimental to film smoothness. Dried nanorod assemblies were cation exchanged air-free by soaking substrates in an anhydrous methanolic solution of (to go from CdS to Cu_2S) ~0.1 mM tetrakis(acetonitrile)copper(I) hexafluorophosphate ($[MeCN]_4CuIPF_6$) or (to go from Cu_2S to PbS) ~0.1mM lead acetate and ~0.1mM trioctylphosphine. Cation exchange reactions were assumed to go to completion, so the exact amount of cation salt to be added could be calculated for the desired degree of exchange. After ~12 hours (to ensure reaction completion), substrates were removed from the cation solution and dipped in a vial of neat methanol. Cation exchange from CdS to Cu_2S was manifested by a change in film color from yellow to light brown. After cation exchange was complete, films were generally kept air-free and moisture-free, although these conditions may not be critical.

Electron Microscopy. SEM images were taken with a Zeiss Gemini Ultra-55 Analytical Scanning Electron Microscope at an accelerating voltage of 3keV. EFTEM images were taken on a JEOL 2100F operated at 120keV equipped with Gatan Tridiem imaging spectrometer. HRTEM images were taken on an FEI monochromated F20 UT Tecnai microscope operated at 200keV. CdS wurztite simulation was performed using MacTempas.

Compositional Analysis. Rutherford backscattering data was taken with a 2.5 MeV Van de Graaff accelerator. The spectra were taken using a 2 MeV He+ ion beam with a Si surface barrier detector at 165o with respect to the incident beam. The samples were tilted by 50 degrees in order to improve depth resolution. The spectra were analyzed using the RUMP software package.

Energy dispersive X-ray spectroscopy (EDS) was taken on a Zeiss Gemini Ultra-55 Analytical Scanning Electron Microscope (accelerating voltage 7keV) with an EDAX EDS detector with Genesis software. A range of spot sizes and locations on film were measured before concluding compositional analysis and to confirm uniformity. Acquisition times were a few minutes. During EDS analysis, the quality of film and nanorod assembly were verified.

Electrical Characterization. All electrical measurements were taken in an Argon glovebox. Current-voltage measurements were taken using a Keithly 236 Source Measurement Unit and a probe station. A droplet of EGaIn (<1mm diameter) was placed on top of the film and contacted with the 'high' probe tip. Contact was made to the ITO by scraping off a small area of aligned rods and smearing Indium onto this area for easy contact by the 'low' probe. EGaIn contact areas were monitored with a 100x sideview camera. Multiple locations on each device were measured and representative data was selected. AM1.5G illumination was provided by an Oriel 91160 300W Xe solar simulator and was directed upward through a quartz window on the floor of the glovebox, on top of which the sample rested, nanorod film facing up.

Nanorod Synthesis & Assembly

Details of the synthetic and assembly procedures for the nanorods can be found in the supporting information of our previous work[1]. One important point to note about repeatability of this assembly is that relatively fresh nanorods (synthesized within ~1 month of assembly attempt) had higher rates of successful assembly. Also, while monodispersity was important (which requires cleaning), over-cleaning was found to result in rods that laid parallel to the substrate. Finding an appropriate balance of monodispersity and cleanliness was difficult and sometimes took a few synthetic attempts before successful alignment. The required cleaning procedure for each batch of rods was slightly different, despite the fact that the syntheses themselves were identical. Assembly substrates (Si_3N_4 for RBS measurements; 150nm 20Ω/square ITO on glass for electrical measurements) were cleaned by sequential sonication in water, toluene, isopropanol and acetone, followed by an oxygen plasma etch.

Rutherford Backscattering Spectroscopy (RBS)

Rutherford backscattering data was taken with a 2.5 MeV Van de Graaff accelerator. The spectra were taken using a 2 MeV He+ ion beam with a Si surface barrier detector at 165o with respect to the incident beam. The samples were tilted by 50 deg in order to improve depth resolution. The spectra were analyzed using the RUMP software package.

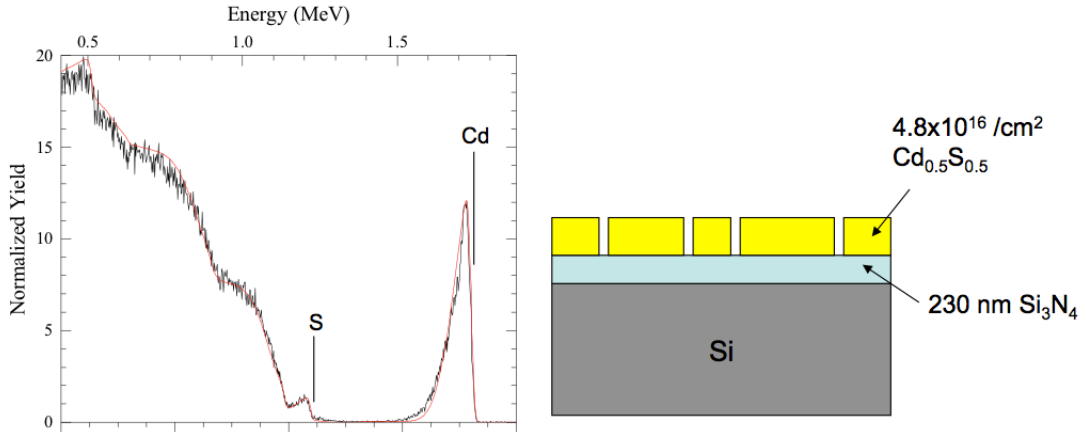

Figure AIII-1. Rutherford backscattering analysis of pure cadmium sulfide nanorod film. Gaps represent the organic matrix comprising nanocrystal ligands (octadecylphosphonic acid). Samples were measured on Si_3N_4 to avoid charging and signal interference with relevant elements.

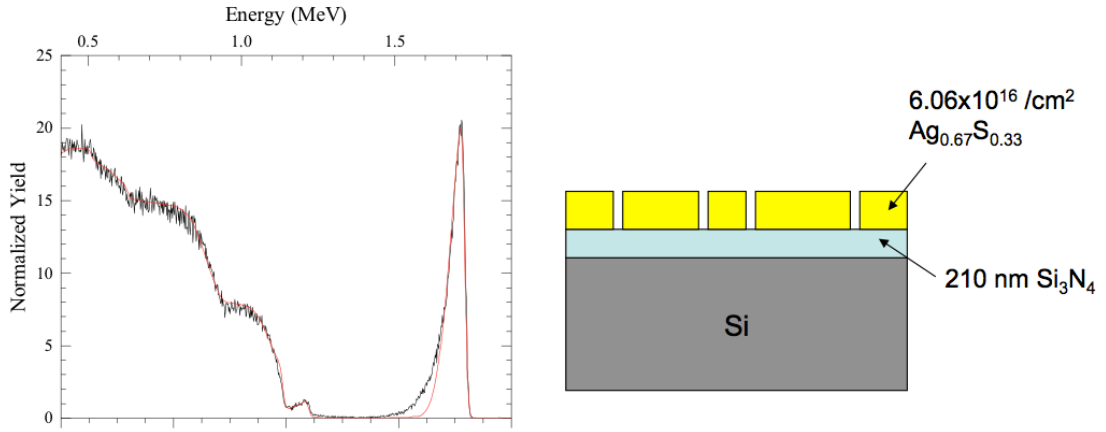

Figure AIII-2. Rutherford backscattering analysis of silver sulfide fully cation exchanged nanorod film.

Secondary Ion Mass Spectrometry (SIMS)

SIMS depth profiles were acquired by Evans Analytical (Sunnyvale, CA) using a PHI6650 Quadrupole SIMS instrument. Samples were sputtered using 2keV Cs^+ primary ions incident on the sample at 60° off-normal to the sample surface. Positive CsM^+ molecular secondary ions were detected using an electron multiplier (where M is the analyzed element). Concentration calibration factors were obtained using analyses of samples of know composition. Depth scales were calibrated using Tencor P10 stylus profilometer measurements of total sputtered crater depths.

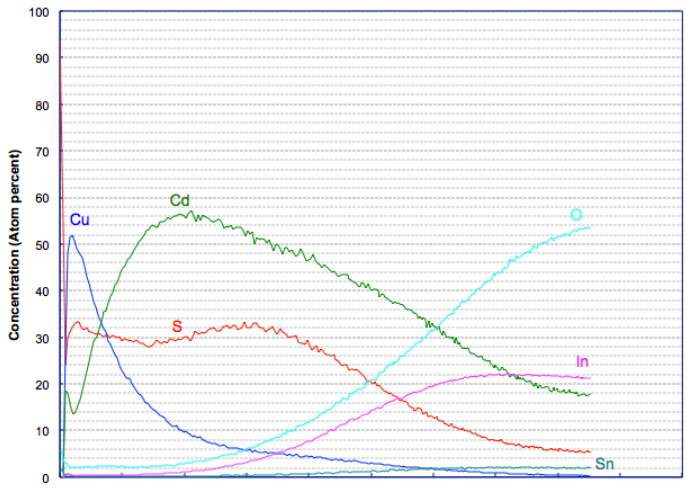

Figure AIII-3. SIMS data taken on a partially-Cu-exchanged CdS nanorod film.

EDS Energy dispersive X-ray spectra were taken at an accelerating voltage of 10keV with a Zeiss Gemini Ultra-55 Analytical Scanning Electron Microscope with an EDAX detector. A range of spot sizes and locations on film were measured before concluding compositional analysis and to confirm uniformity. Acquisition times were a few minutes. Data was analyzed with Genesis software to obtain atomic percents of each element. Because data was taken from a nanorod film on ITO/glass, Indium and Tin both overlapped with the Cd signal. For approximation of composition, we observed the ratios of Cu:S, assuming that all Cu present was in Cu_2S and that all sulfur present was in either Cu_2S or CdS. Pb and S peaks overlapped, so % PbS composition was inferred from absence of Cu (after a pure Cu_2S film was converted to PbS). Spotsizes were typically 10um in diameter. During EDS analysis, the quality of film and nanorod assembly were verified.

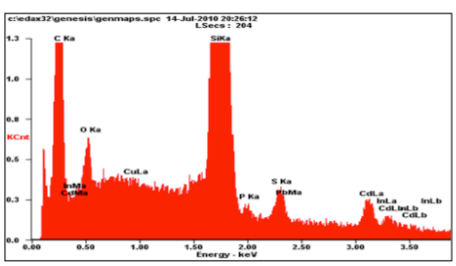

Element	Wt%	At%
CK	16.98	33.80
OK	00.84	01.25
CuL	00.10	00.04
SiK	73.19	62.30
PK	00.20	00.16
SK	01.21	00.90
PbM	00.44	00.05
CdL	07.05	01.50
InL	00.00	00.00
Matrix	Correction	ZAF

Figure S4: EDS data indicating approximate film composition of ~100% CdS.

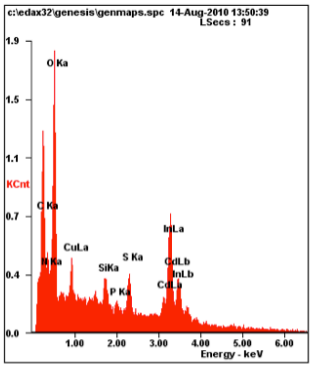

Element	Wt%	At%
CK	10.59	31.72
NK	02.89	07.41
OK	14.52	32.64
CuL	03.21	01.82
SiK	01.71	02.19
PK	00.64	00.74
SK	03.17	03.55
CdL	13.49	04.32
InL	49.79	15.60
Matrix	Correction	ZAF

Figure S5: EDS data indicating approximate film composition of ~25% Cu_2S, 75% CdS.

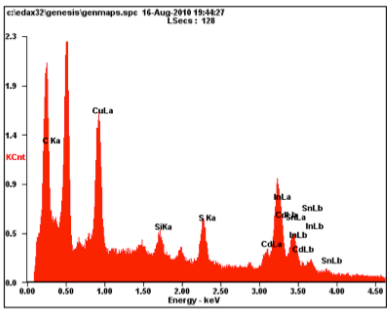

Element	Wt%	At%
CK	24.22	49.37
CuL	14.58	05.62
SiK	44.02	38.37
SK	05.39	04.11
CdL	06.99	01.52
InL	02.87	00.61
SnL	01.95	00.40
Matrix	Correction	ZAF

Figure S6: EDS data indicating approximate film composition of ~68% Cu_2S, 32% CdS.

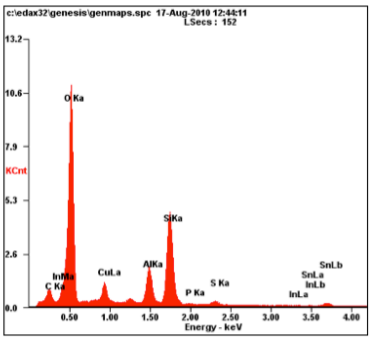

Element	Wt%	At%
CK	08.69	14.69
OK	42.92	54.45
CuL	07.10	02.27
AlK	08.74	06.57
SiK	27.97	20.21
PK	00.32	00.21
SK	01.86	01.18
InL	01.59	00.28
SnL	00.81	00.14
Matrix	Correction	ZAF

Figure S7: EDS data indicating approximate film composition of ~100% Cu_2S.

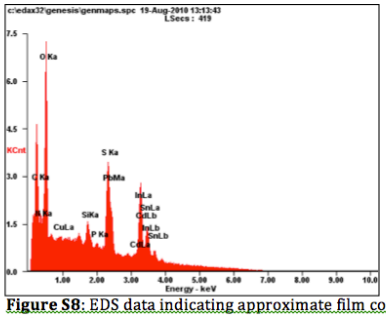

Element	Wt%	At%
CK	07.88	27.29
NK	00.85	02.54
OK	13.06	33.93
CuL	00.23	00.15
SiK	01.48	02.19
PK	00.25	00.34
SK	08.18	10.60
PbM	09.81	01.97
CdL	04.02	01.49
InL	43.01	15.57
SnL	11.22	03.93
Matrix	Correction	ZAF

Figure S8: EDS data indicating approximate film composition of ~100% PbS by absence of Cu signal out of the noise.

Formation of EGaIn electrode

To make electrical contact to the aligned nanorods we used a gallium-indium eutectic (EGaIn) as a liquid metal probe. When used in ambient atmosphere, a surface layer of gallium oxide forms over a droplet of EGaIn suspended from a syringe needle[2]. The rigid oxide skin increases the surface

tension of the EGaIn, allowing the formation of a cone-shaped tip (filament) of EGaIn at the end of the needle.

Because our electrical measurements were all carried out in an Argon glovebox, the EGaIn could not form the oxide skin necessary for a filament. Instead, to form an EGaIn probe we dipped the end of a squared-off 21-gauge needle into the bottle of EGaIn (used as-purchased from Sigma-Aldrich). (A small amount of solid material was in the bottle with the liquid EGaIn. It is presumed that the solid was gallium- or indium- oxide because the EGaIn was packed under air.) Carefully withdrawing the probe needle from the EGaIn bottle resulted in a very small filament of EGaIn attached to the tip of the needle. We suspect that we were able to get these filament shapes by inadvertently fishing out an oxide flake with the probe needle. The EGaIn-coated needle was brought into contact with the nanorod film using a micromanipulator. A sideview camera allowed us to monitor the distance between the EGaIn filament and the substrate surface (Figure AIII-9), and a live current measurement verified that we were in good electrical contact.

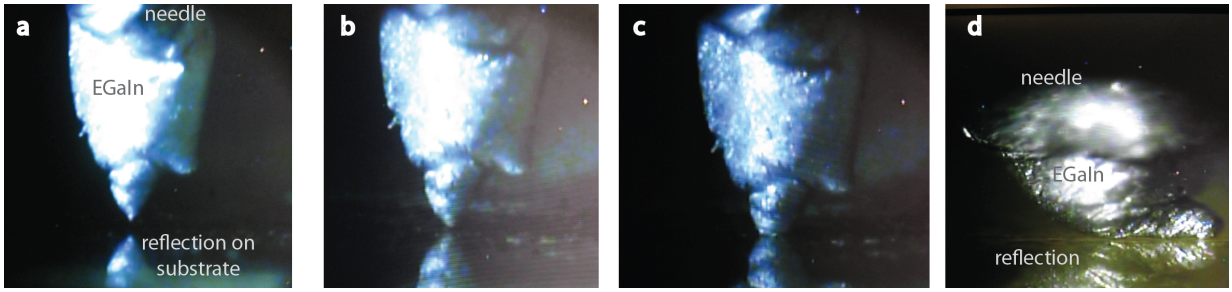

Figure AIII-9: EGaIn probe approaching substrate (a,b), and making contact (c,d).

We sometimes observed zero current when the EGaIn probe was in clear physical contact with the substrate. Continued lowering of the EGaIn probe toward the substrate resulted in deformation of the EGaIn filament (Figure AIII-9d) and eventually caused current to flow through the probe. We hypothesize that in these cases, the filament had a large oxide content which prevented current flow through the probe until the filament deformed enough for the metal in the EGaIn/oxide agglomeration to make contact with the semiconductor film. To avoid this issue, we placed a small ball of liquid (unoxidized) EGaIn directly from the bottle onto the substrate and contacted it with a bare probe tip (Figure AIII-10). This method produced larger contact areas and limited precision in selecting a test area, but eliminated the "false contact" issues we had with the filament.

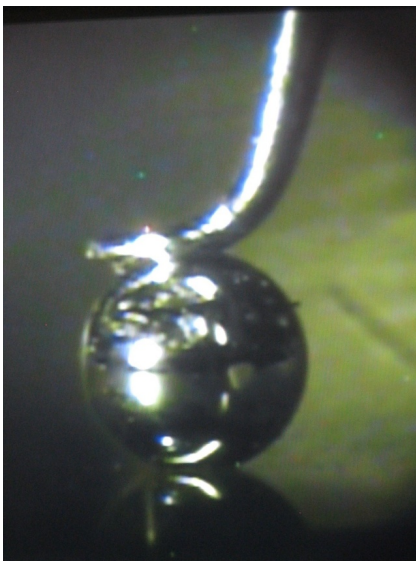

Figure AIII-10. Bent probe contacts EGaIn droplet on CdS/Cu_2S substrate.

References

1. Baker, J. L., Widmer-Cooper, A., Toney, M. F., Geissler, P. L. & Alivisatos, A. P. Device-Scale Perpendicular Alignment of Colloidal Nanorods. *Nano Letters* **10**, 195-201 (2010).
2. Chiechi, R. C., Weiss, E. A., Dickey, M. D. & Whitesides, G. M. Eutectic gallium-indium (EGaIn): A moldable liquid metal for electrical characterization of self-assembled monolayers. *Angewandte Chemie-International Edition* **47**, 142-144 (2008).